STAFFORDSHIRE UNIVERSITY

School of Creative Arts & Engineering

A Novel Swirl Generator for Improving the Performance of Marine Current Turbine

PhD submitted to Staffordshire University,

for the Degree of Doctor of Philosophy

Sharif Zafer Al Dajani

October 2021

Acknowledgement

I feel indebted to many people, so many people I would like to thank, all those who shared either morally or practically in making this possible and an enjoyable experience for me.

I would like to express my deepest sense of gratitude and deep respect to my supervisors Dr. Abdel Hamid Soliman (Staffordshire University), Dr. Khalid Saqr for their valuable support, patient guidance, immense knowledge and great advice. Above all and the most needed, they provided me support in various ways and helped whenever I was in need throughout all the stages of this thesis. Their support also included teaching me the professional way of thinking, providing me with necessary references, as well as giving me extraordinary experiences throughout the work. In addition to their advice and their willingness to share their bright thoughts with me, those were very fruitful for shaping up my ideas and research. Words cannot describe how grateful I am. I think their presence was the best thing that could happen. I am grateful in every possible way and hope to keep up this collaboration in the future.

I also wish to express my appreciation and thanks to Dr. Abdel Hamid Soliman for making my visits to Stafford really enjoyable, for keeping me going when times were tough, for being totally supportive in all times and above all making me feel home. He is my brother in the UK.

I would like to send gratitude to my previous supervisors Dr. Dave Cheshire, Dr. Neil Hart (Staffordshire University), for their great help and encouragement during the early stages in the PhD.

I would like to express my respect to the team of graduate school, the head of department and Mott Theresa (Staffordshire University) for their great effort helping me during the years of PhD.

I would like to pay my gratefulness and respect to my supervisor Dr. Mohamed Fahmy for his continuous support and help in various ways, patience and valuable suggestions throughout the years and during all stages of my PhD.

I would like to express my great thankfulness and gratefulness for my supervisor Dr. Khalid Saqr for his guidance, motivation and knowledge which helped me during all time of the research. His advice, concern and patience are really appreciated. I would like to thank him for encouraging my research, he has been a tremendous mentor for me. His astounding perspective and thorough criticisms were of great value. Furthermore, his honest and precise review were very helpful to trace points of weakness in the thesis and strengthen them. Without his help, this work would not be possible.

I would like to express my gratitude to all my colleagues in the Arab Academy for their support and encouragement for me. I would like to express my gratitude to Eng. Hussein Kamal, my friend in Arab Academy for his great help and support during PhD.

Words fail me to express my appreciation and denote my sincere thanks to my family members who gave me spiritual continuous support and encouragement to complete this thesis successfully, their prayers for me were what sustained me thus far and their love and support have taken the load off my shoulder. Finally, I would like to thank everybody who was important to the realization of this thesis.

List of Publications

1. S. Dajani, M. Shehadeh, N. Hart, D. Cheshire, Aspects of Tidal Power Resources in Egypt, RAEPS Conference, Helnan Palestine Hotel, Alexandria, 3-5. April 2012.

2. S. Dajani, M. Shehadeh, K.M. Saqr, A.H. Elbatran, N. Hart, A. Soliman, D. Cheshire, Numerical Study for a Marine Current Turbine Blade Performance under Varying Angle of Attack, TMREES17, 21-24 April 2017, Beirut Lebanon, ELSEVIER.

Data sets:

Dajani, Sharif; Shehadeh, Mohamed Fahmy; Soliman, Abdel-Hamid; Elbatran, Ali; Ahmed, Yasser; Saqr, Khalid (2019), "CFD Validation Database for NACA HFSX Hydrodynamics", Mendeley Data, v1 http://dx.doi.org/10.17632/p3y3xjmpjt.1

To be submitted

1. S. Dajania, b, M. Shehadeh, A. Soliman, A. Batran, Y. Ahmed, K. M. Saqr, CFD Simulation for a 2D Marine Current Turbine Blade Performance and power calculations. To be submitted to Energy Journal.

2. Sharif Al-Dajani, Abdel Hamid Soliman, M. Shehadeh, Aly El-Batran, Khalid M. Saqr, A Novel Swirl Generation Concept for Improving the Hydrodynamic Characteristics of Marine Current Turbines. To be submitted to Energy Journal.

Abstract

Marine energy is one of the areas of high potential to improve Egypt's renewable energy mix under the national 2030 development plan. The New Delta national project aims to develop the north-western Mediterranean coast of Egypt. In this coastal part of the Mediterranean, marine current speeds are low, however, they have consistent and homogenous directions along the year. Horizontal Axis marine current turbines (HAMCT) are good candidate to harness marine energy in this location. However, at such low current speeds, these turbines have low hydrodynamic performance.

This thesis conceptualizes and validates a novel static device that is designed to improve the hydrodynamic performance of HAMCT under transitional flow conditions. This device is called the *Vane Swirl Generator (VSG)*. It is a static structure of twisted flat vanes to be installed upstream HAMCT. The function of VSG is to convert part of the axial momentum of the incoming flow into rotating momentum to improve lift force and reduce drag resistance.

The literature review of this thesis revealed a severe scarcity of available information on HAMCTs' hydrodynamic performance under transitional flow conditions. This is because most of the existing platforms and R&D projects are focusing on regions with high current speeds.

In order to demonstrate and validate the proposed VSG concept, a methodology based on Computational Fluid Dynamics (CFD) has been carried out. The CFD methodology was undertaken in two validation stages and one parametric analysis stage. The total number of simulations reported in this thesis is 110 simulations. The only available comprehensive study on HAMCTs under transitional flow conditions was conducted in Fiji Island and was adopted as the benchmark case-study to validate the CFD models in this thesis.

The CFD modeling approach was parametrized based on the angle of attack (AoA) starting from theoretical 2D simulations, then 3D single-blade simulations, then 3D full-scale turbine simulation. A turbulence modeling comparison revealed that the SST $k-\omega$ model is the best fit for the CFD simulations. In transitional flow, fully-developed turbulence models were found to miscalculate the hydrodynamic performance parameters and sometimes diverge the solution.

The Final 3D CFD model used to study the effects of the novel VSG on HAMCT's hydrodynamic performance parameters had a modeling error ranging from -18.6% to 28% depending on 0º-16º AoA range. In HAMCT, such range of error translates to -4.3% to 5.3% in power coefficient calculations.

Swirl flow generated by VSG was studied at different intensities ranging from 0.1 to 0.5 as defined by the swirl number(S_n). It was found that low swirl deteriorates lift and increases drag. It was found that the novel VSG concept provides significant performance improvement of lift

coefficient for $0.3 \leq S_n \leq 0.5$ and $0 \leq AoA \leq 8$ as restricted by the increase in drag coefficient. The results show significant improvements in the coefficient of power (C_p) from 18% without swirl to 27% at 0º AoA and from 17.5% without swirl to 33.5% at 12º AoA.

Table of Contents

Page

List of Figures

List of tables

Table number **Page**

Abbreviations

AOA	Angle of Attack
BEM	Blade Element Momentum
CFD	Computational Fluid Dynamics
CAD	Computer Aided Design
CAE	Computer Aided Engineering
DES	Detached Eddy Simulation
DNS	Direct numerical simulation
FEA	Finite Element Analysis
FSI	Fluid Structure Interactions
HAMCT	Horizontal Axis Marine Current Turbine
LES	Large Eddy Simulation
MCT	Marine Current Turbine
RANS	Reynolds Averaged Navier Stokes
SST	Shear Stress Transport
TSR	Tip Speed Ratio
VSG	Vane Swirl Generator
VAMCT	Vertical Axis Marine Current Turbine

Symbols

A	Cross Sectional Area
α	Angle of attack
AOA	Angle of Attack
W	Angular Velocity
AR	Aspect Ratio
Γ	Circulation
ρ	Density
C_d	Drag Coefficient
F_D	Drag Force
Gw	Giga Watt
g	Gravity Acceleration
Kw	Kilo Watt
D	Turbine Diameter
x	Distance from Turbine Hub
C_l	Lift Coefficient
F_L	Lift Force
C_m	Moment Coefficient
Mp	Pitching Moment
Cp	Power Coefficient
P	Pressure
r	Radius
V_{rel}	Relative Velocity
Re	Reynolds Number
Sn	Swirl Number
Ω	Vorticity
2D	Two Dimensional
3D	Three Dimensional

Chapter 1

Introduction

1.1 Background

Tidal energy is considered as one of the most promising renewable energy resources for its green environmental footprint and high-energy density. Marine current turbine (MCT) generates power from tidal energy. This turbine runs on the same principles of operation as those of wind turbines. However, their performance is different due to the inherent physical differences between wind and tidal currents [1, 2]. In comparison with wind turbines, studies on MCT design, operation and technologies can be fairly considered limited [3, 4]. There are many areas of rapid development in MCT research such as improving the turbine materials and optimizing its hydrodynamic performance for low-speed currents [5]. Most of the reported MCT power generation stations operate at current speed of more than 2.5 m/s [6, 7] such as the SeaGen turbine [8]. At this speed tidal energy has high economic potential compared to wind energy. This is because under the same conditions, water is at least 800+ times dense than air, thus, carry much higher kinetic energy [6]. MCTs working under relatively low current speed (<2.5 m/s) are new [9] and still in technology development stages and the present thesis contributes to this class of MCTs.

Studies on the potential of tidal energy along the 1000 km length Mediterranean coast of Egypt are scarce [10, 11]. A recent Mediterranean energy mapping study found that the energy flux along the coast of Egypt ranges from 1.2 to 3.2 kW/m [12]. This corresponds to an average current speed of 2 m/s along the year. Water depth off the urban coastal line is consistently below 120 m [13]. This coastal line has numerous touristic and commercial activities and is rapidly developed within the Egypt's Vision 2030 that also include a substantial increase in renewable energy adoption and reliance [14, 15]. Marine current speed and depth conditions in Egypt's north coast generally favor seabed-mounted MCTs with small diameter-to-depth ratio to minimize its drawbacks on marine environment and human activities [16, 17]. Designs such as Nova M100[1] of 100 kW rated power qualify for such location. However, in terms of available published studies, there is very scarce data on MCT hydrodynamics in this range of operating conditions [4, 5].

[1] www.novainnovation.com

The research presented in this thesis addresses the hydrodynamic performance of horizontal axis MCT. Until today, the efforts done to improve hydrodynamic performance mainly address the turbine's hydrofoil and blade geometry [3, 18, 19]. As it will be detailed later in Chapter 2, Computational Fluid Dynamics (CFD) models are efficiently used to evaluate the MCT hydrodynamic performance [3]. The methodology of this thesis is established based on CFD modeling approach. CFD models are used in this thesis to establish a parametric framework in order to achieve the research objectives, detailed later in this Chapter. The parametric CFD framework was established after detailed verification and validation procedures were successfully undertaken as reported in Chapters 3 and 4.

This thesis proposes a novel method to improve MCT hydrodynamic performance. This novel method relies on adding a Vane Swirl Generator (VSG) upstream the MCT to increase the tangential momentum admitted to the turbine, hence, improve its hydrodynamic performance. Although the VSG theory of operation, as explained in Chapter 5, is simple and straightforward, it has never been reported in any similar system of marine energy extraction. VSG can be categorized as a passive flow-control method, similar to the same concept used to improve combustion aerodynamics in gas-turbines. The innovative introduction of VSG and its effects on the hydrodynamic performance of MCT are the main contributions of this thesis, as detailed in Chapter 6.

It is important to navigate the background of tidal energy conversion in order to explain the potential impact of the proposed VSG on different aspects related to MCT design and operation. Since the early 1970s, researchers have been working to discover renewable energy resources that can be less harmful and less environment-damaging than fossil fuel. As shown in figure (1.1), the ocean covers about 70% of our planet surface and it contains a huge potential energy source in different forms. One of the ocean energy hidden forms is the ocean current, where the sun radiation is absorbed by the ocean, heats it up and circulates between different areas. These consist of tides with their waves and temperature difference. The scope of the researchers is limited to the ocean current turbine to extract energy from ocean current. [20]

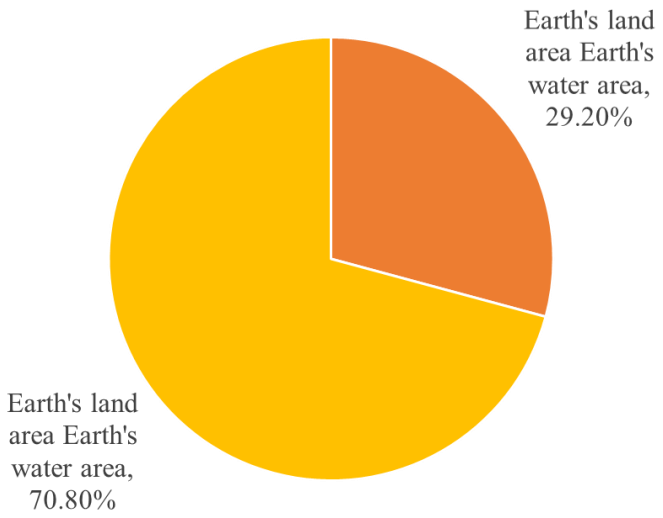

Figure (1.1) Ocean percentage on earth

The oceans are an omitted resource, which can be a major contributor to our future energy needs. There is a claim on finding an economical way to harness energy from the ocean, in the quest for a non-polluting renewable energy source. As shown in figure (1.2), there are ocean energy forms that are being investigated and exploited as potential sources for power generation, such as solar energy, wave energy, offshore wind energy, tidal energy and ocean current energy, but these can only be beneficial if cost-effective technology can be advanced to exploit such resources reliably and cost-efficiently [21, 22]

One of the most important advantages of tidal energy is the fact that it is much less affected by climate change; whereas wind, wave, and solar energies are much more affected by climate changes. A grace of the tidal current resource is being gravity-bound, both spatially and temporally, and it is quantifiable. Devices, that are designed for tidal energy removal come in many different shapes, sizes and forms, though, principally, they all connect either potential energy or kinetic energy from the tide and convert it into electricity. In the past few years, there has been a special focus on kinetic energy extraction, and it is expected that this specific principle of operation, particularly regarding the horizontal axis tidal turbine (HAMCT) concept will be the concern in many researches [23]. The most significant advantages of marine current energy are predictability and reliability. It is the gravitational interaction of the Earth-Moon-Sun

systems that has been driving the astronomic nature of tides and making marine tidal currents highly predictable with 98% accuracy for decades [21]

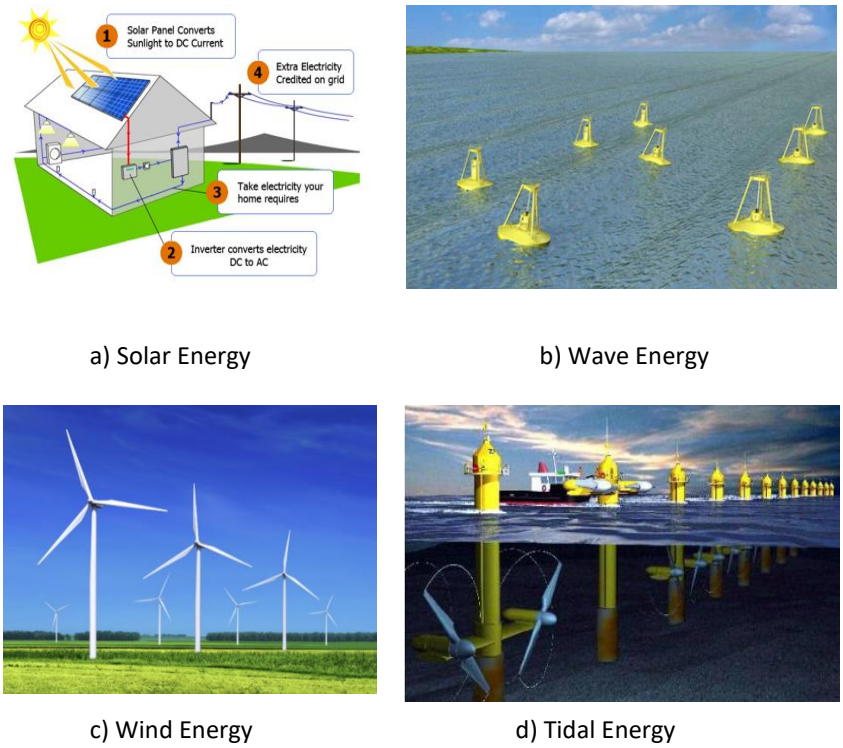

a) Solar Energy

b) Wave Energy

c) Wind Energy

d) Tidal Energy

Figure (1.2) Forms of renewable energy [21, 22]

The two primitive methods for generating electricity from marine tidal energies, is either by building a tidal barrage across an inlet for river or a bay as shown in figure (1.3), or by extracting energy from free-flowing tidal currents. However, a major aspect that cannot be looked over for this solution is that a large barrage system would change the hydrology and may have negative effects on the local ecosystem. Thus, during the last few decades' engineers have switched them researches towards technologies that capture the kinetic energy from tidal-driven marine currents. The potentially available electricity from marine current energy, extracted with the present technologies, is estimated at approximately 75 GW in the world and 11 GW in Europe [24].

In recent years, several horizontal axis and vertical axis marine current turbines (MCT) have been developed around the world [4]. The majority and most applied of MCT devices are horizontal axis turbines with a spin axis parallel to the current flow direction. The main obstacle related to vertical axis turbines are relative low self-starting capability, high torque fluctuations and generally lower efficiency than horizontal axis turbine. Researchers believe that currently only horizontal axis MCTs are the most advanced technical and economical solutions for large-scale marine current turbines with a power capacity of over 500 kW [21, 23]

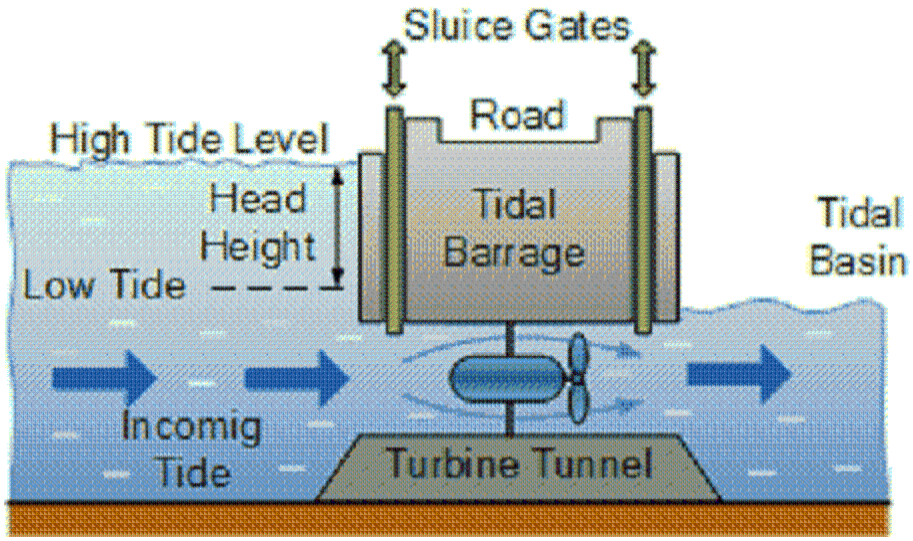

Figure (1.3) Tidal barrage system [25]

Most of tidal sites are relatively bi-directional, in spite of that some sites can have a flow reversal of 20° or more away from 180°[26] such as the flow around islands, where a swipe upon flow reversal of around 35° from recti linearity is apparent. Experimentation and numerical studies show that an increase in turbine yaw angle results in a harmonious power decrease, and consequently a fully straight-lined flow is more desirable [27]

1.2 Horizontal Axis Marine Current Turbines (HAMCT)

There are two types of rotating marine current turbines horizontal axis (HA) and vertical axis (VA). This classification is according to the turbine's axis of rotation with respect to flow streamwise direction. In HAMCT, the axis of rotation is parallel to the flow [28] . In comparison with VAMCT, HAMCT tends to have higher efficiency, but are more complex in design; as it

requires blades which combine twist and taper [29]. It is important to mention that the peak efficiency of HAMCT ranges from 39% to 48% [30]. The direction of the flow is significantly important to determine the turbine efficiency, this is due to the fact that the rotor or the blades must be rotated between the receding tide and flood tides, or else bi-directional blades are used [31, 32], in addition to the higher efficiency, VAMCTs also tend to have lower rotational velocities than HAMCTs, which although is still noticeable, reduces the problem of generator matching [29].

Figure (1.4) Horizontal axis MCT [33]

HAMCT designs are different according to how many blades the rotor has and how the device is fixed in position. The most developed HAMCT is the 1.2MW SeaGen, figure (1.4), developed by Marine Current Turbines (MCT), it is pile driven and has one rotor, having 2 blades. Installed in 2008, it is the first commercial scale tidal stream turbine to generate power in UK waters [33].

1.3 Environmental Aspects of MCT

Although the present work does not involve environmental analysis, it is important to outline the overall interactions between MCT and marine environment as a limitation of the proposed work in this thesis. Tidal energy density depends on different factors, for instance depth and weather [34]. These factors contribute to the decision of where to locate MCTs, with each device having a minimum rated flow velocity and a securing mechanism that may only fit for a given depth range. On the other hand, MCTs have direct and indirect effects on the surrounding marine environment and life [35]. The main regulatory factors that must be considered when assessing the environmental impact of MCTs are environmental protection, biodiversity conservation, as well as the prevention of interference with legitimate uses of the sea, such as shipping [36]. In some cases, developers and researchers face great difficulties and spend huge time in getting the necessary approval and license. Many tidal flow devices are still in varied stages under development. Therefore, there have been few studies into the environmental effects of these technologies. Yet, the studies which have been done are either based on predictions or have been unproven [37], with few exceptions.

A remarkable consideration is that the quality of the water surrounding MCT could change significantly after device installation. For example, turbulence may change due to the effects of sediment transport and deposition caused by the altered tidal flows and current streams which may occur due to these devices. The effect of this on marine life is uncertain. A successful type could be negatively affecting and vacating the area, whereas the opposite is also a possibility; where new type is used. Even though water quality was not included in the SeaGen environmental monitoring program; a species of mussel not found in the area prior to deployment was subsequently found on the monopole structure and was considered a positive addition to the biodiversity [38].

The influence on shipping is one more consideration and this may limit the location and size of device arrays. Also, contamination from the machinery used should be considered such as the release of hydraulic fluids, lubricants, etc. [38]. No evidence has yet been found that Electromagnetic fields from generators and rites affect the migratory and feeding habits of marine mammals and fish. Nonetheless, this is still a debatable area [39].

There is a little chance of creatures, such as fish, mammals or even diving birds, striking turbines. There is also consideration of the cavitation effects causing sudden pressure changes that could harm fish [40]. Some device developers and researchers have tried to lessen the risk to marine life in their designs, such as the Open Hydro and the Alstom Hydro, which both incorporate an open center allowing safe passage for fish and marine mammals [41, 42].

The construction of MCTs has an influence on the surrounding environment, from mooring systems, such as anchors and foundations, to the laying of transmission cables and pipes. In the case of SeaGen, this was found to be temporary and the structure has since become a prosperous homeland for marine creatures [43]. It is also remarkable that high noise levels during construction could be an issue [44]. Marine mammals can predict operational noise of SeaGen up to 1.4 km away from the device, and have a local avoidance of around 250 m away from the device, although this may not be due to noise as the same notice was taken when the turbine was not operating (shutdown) [43].

1.4 Problem Statement and Significance

The problem addressed in this thesis concerns the limited hydrodynamic performance of HAMCT operating under marine current speed below and up to 2 m/s. Recent reviews clearly show a research gap in HAMCT operating under such condition of low marine current speed [4, 45-47].

The significance of this problem arises from the demand to adopt renewable marine energy technology in Egypt's north coast on the Mediterranean Sea. Under such conditions, the flow around MCT is transitional, as explained later in Chapters 3 and 4. As dictated by the generalized problem of turbulence[48], transitional flow over rotating turbines remains as an open-end question, such as all transitional shear-flow problems[49].

1.5 Research Objectives

The aim of this research is to improve the hydrodynamic performance of HAMCT under marine current conditions relevant to the south Mediterranean Sea. The research objectives set to achieve such aim are:

- To develop and validate a simulation model, using Computational Fluid Dynamics (CFD), that is capable of predicting the hydrodynamic performance characteristics of HAMCT Chapters 3 and 4.
- To propose and validate a novel method to improve the hydrodynamic performance of HAMCT using passive swirl-control strategy (VSG). The details are explained in Chapter 5.
- To identify the optimum range of swirl number that provides HAMCT hydrodynamic improvements. The details are explained in Chapter 5.

1.6 Research Scope and Methodology

The scope of this research is focused on the conception and evaluation of the VSG and its application to improve hydrodynamic performance of HAMCT under low current conditions. Despite the apparent simplicity of this novel concept, as it will be shown in the following chapters as its positioning upstream of the turbine requires full hydrodynamic evaluation to be carried out.

To fulfil the research scope, a CFD methodology has been devised to provide preliminary assessment for the VSG as a method to boost HAMCT hydrodynamic performance. CFD is an efficient and proven engineering tool to test and evaluate new fluid flow technologies without the need to build and operate expensive experimental test rigs. The methodology has been deconstructed as following:

I. First stage: Model Verification and Validation (Chapters 3 and 4)
II. Second Stage: Conception and evaluation of the VSG device (Chapter 5)

In the first stage, a CFD model of HAMCT was established based on existing experimental data available in literature. However, since all previously published studies are focused on high-current speed and high Reynolds number (i.e. fully developed turbulent flow), the validation exercise is the core of the CFD parametric study and had to be carried out on three steps, as illustrated in figure 1.5 and explained as following:

(a) Validation of the turbine-blade hydrodynamics (chapter 3): this first step aims at establishing the validity of the turbulence model and CFD solution strategy and ensure that the model predicts physically valid performance parameters (coefficients of lift and drag) of the blade hydrodynamics at Re = 190,000

(b) Validation of the full turbine model (chapter 4): the second step ensures that the CFD model predicts physically valid performance parameters. This was particularly challenging since there is no available experimental data on a full HAMCT at Re = 190,000

(c) Validation of the VSG (chapter 5): Swirl flow is mainly characterized by Rankine vortex structure which has exact equations to describe its velocity-component profiles. Validation of the VSG is necessary to ensure that the final CFD presents the swirl flow field generated by VSG accurately. This is presented in chapter 5 by comparing the CFD model results with the analytical solution of the Rankine vortex exact equations driven from Navier-Stokes equation.

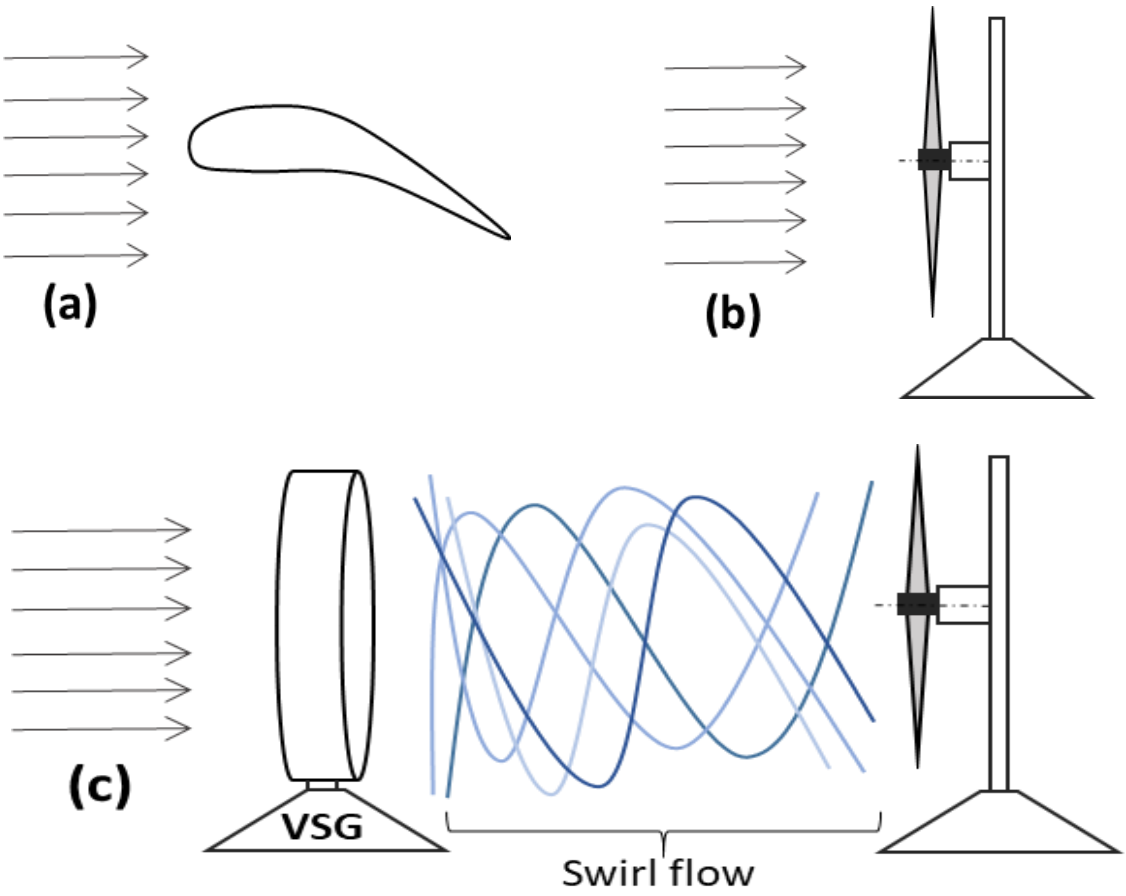

Figure (1.5) Illustration of the research methodology, hydrodynamic performance parameters like coefficients of lift, drag and pressure are validated first with a 2D CFD model to establish the modeling approach suitable for Re=190,000 as shown in (a). Then, further validation is carried out for a full-scale 3D model rotor as shown in (b). The VSG generates swirl flow field as shown in (c) that is validated by comparison with the analytical solution of the Rankine vortex exact equations.

1.7 Contribution to Knowledge

Primary contribution: Conception and validation of a novel vane swirl generator to improve the hydrodynamic performance of marine current turbines under low-current speed.

Secondary contributions:

- Created a unique validated CFD dataset for HFSX hydrofoil hydrodynamics under transitional flow conditions for the first time as open-access: Available at: http://dx.doi.org/10.17632/p3y3xjmpjt.1
- Created the first validated CFD model of 3D HAMCT hydrodynamics under transitional flow conditions (Re = 190,000).
- Proposed and validating a novel swirl generator for improving HAMCT hydrodynamic performance.
- Identified the swirl number and angle of attack ranges that provide hydrodynamic performance improvement for HAMCT

CHAPTER 2

Literature Review

2.1 Background

Compared to wind turbines, published studies of HAMCT are very scarce, figure (2.1) show a comparison between Scopus records of HAMCT papers vs wind turbine papers in the past ten years. The lack of publications on HAMCT is due to the rapidly increasing focus from large energy companies on HAMCT. Research findings have immediate economic value and researchers are more inclined to file patents rather than publish papers in this field. The scarcity of literature in the field poses limitations on the availability of data, operating conditions and simulation modalities used to establish CFD models.

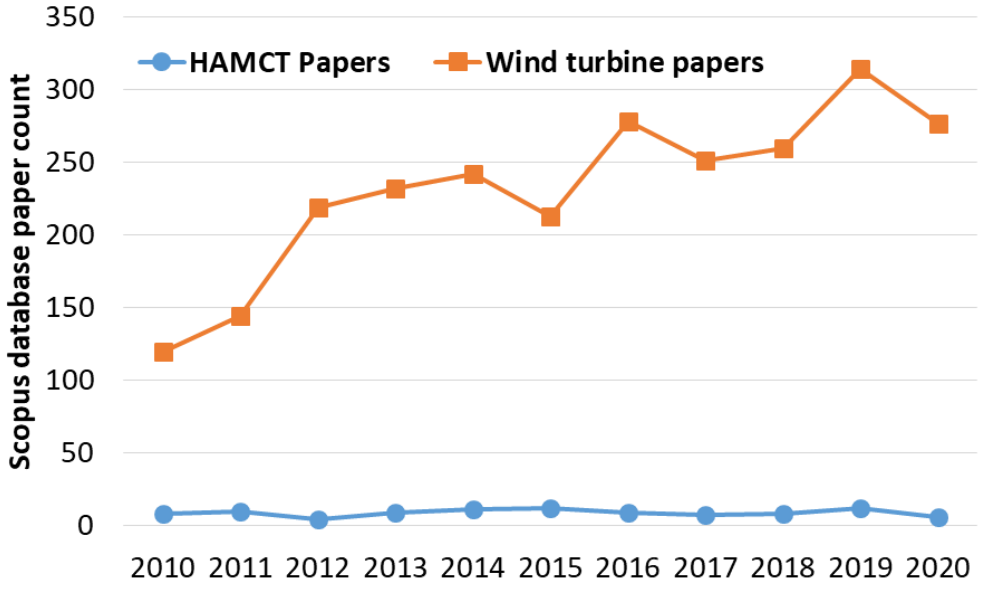

Figure (2.1) Paper count on HAMCT vs wind turbines from Scopus database.

The total number of published studies on HAMCT since 2010 was found to be 102 papers. The papers focusing on the hydrodynamic performance was found to be 53 papers, with 34 papers reporting CFD results and 19 papers reporting experimental results. Figure (2.2) summarizes the literature search and classification. The papers were obtained, read, classified and used to establish the basis for this thesis. Only one general review paper [50] could be identified in the same period.

This chapter reviews previous CFD works on HAMCT to establish context of the proposed contribution. The review scope is focused on CFD studies done to investigate HAMCT hydrodynamics. The objectives of this review are:

1- To identify the CFD modelling approach and strategy used to study the hydrodynamics of MCT.
2- To identify previous works related to hydrodynamic performance improvement methods

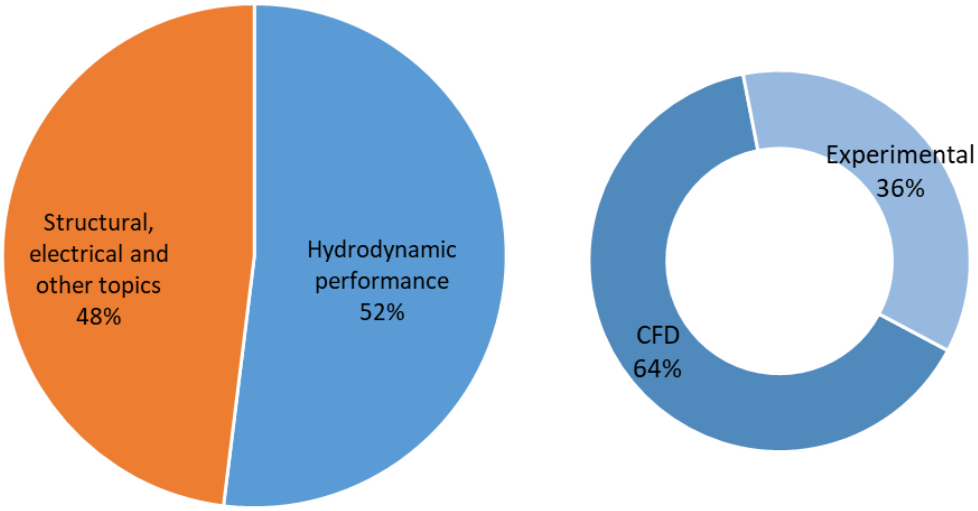

Figure (2.2) Classification of Scopus indexed papers on HAMCT by topic identified keywords. A total number of 34 CFD papers was published since 2010.

To achieve the first objective, previous works were discussed in relation to their CFD approach mainly categorized by the dimensional consideration. Two dimensional (2D) studies are reviewed first. Then, three dimensional (3D) studies are reviewed with a focus on flow regime and modeling setup. To achieve the second objective, a discussion of previous improvements methods is presented and summarized. Tabulated summaries of all studies covered in this chapter are presented in the thesis' appendix.

2.2 Terminology of HAMCT Hydrofoil

The basic terminology, force analysis and hydrodynamic parameters are sketched in figure (2.3) The Angle of Attack (AoA) is a primary hydrodynamic operation parameter since it controls the separation and reattachment of the flow. The force analysis represents the

hydrodynamic performance; as the hydrofoil converts hydrodynamic power to work to rotate the turbine rotor. The forces are usually expressed in non-dimensional drag and lift coefficients that are derived to give characteristic indication of the hydrodynamic performance. The Chord length is important in calculating the energy capacity of the turbine as well as the operating Reynolds number in some cases.

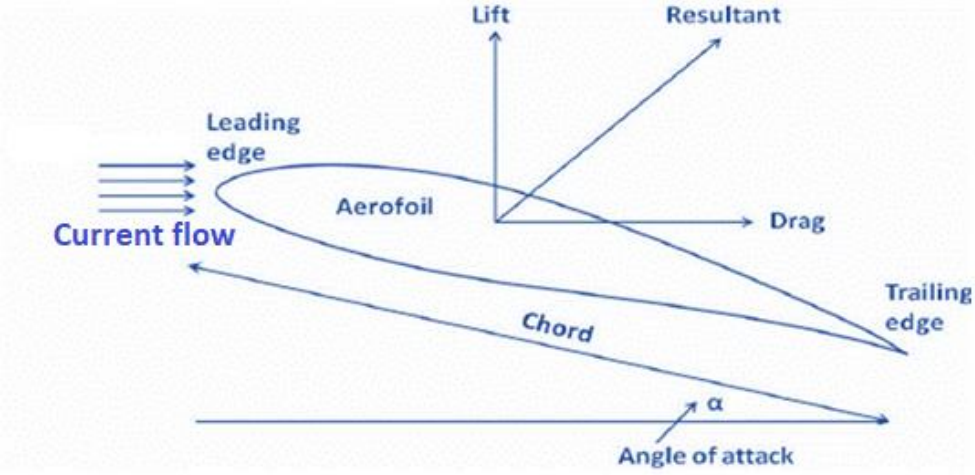

Figure (2.3) Hydrofoil terminology, force analysis and hydrodynamic parameters.

2.3 Computational Fluids Dynamics (CFD)

The most commonly used techniques in research and development in industry these days are Blade Element Momentum (BEM) codes [51], Finite Element Analysis (FEA) [52], and Computational Fluid Dynamics (CFD) [53]. Technological development has boosted the accuracy of codes resulting in several powerful tools that, when used either singly or in combination with each other, can give vital information to the performance of a marine current turbine in varying flow conditions [26]. There is a special focus being imparted to common and quantifiable marine sources, such as marine currents, or tides. There is a need for renewable energy sources to become more vital, the design and optimized MCTs are essential, as they face different forces in their argumentative sub-sea environment.

CFD is a powerful tool which, when used correctly, can give valuable data to monitor the performance of MCTs. It is significant not to

underestimate the use of simpler CFD techniques, like panel codes, at the groundwork design stage where an insight into cavitation characteristics and energy extraction can be achieved, which describes the need for further work. RANS solvers are required to model the complex flow situations taking place around the turbines at a more advanced design stage. Finally, a coupled fluid-structural analysis is required to better study how the flow affects the structural integrity of both the rotor and the supporting structure. It has been noted from the experimentation and calculation, that a surge in turbine yaw angle causes a consistent power decrease, and so a fully rectilinear flow is required. Computational fluid dynamics (CFD) is one of the branches of fluid mechanics that uses numerical methods and algorithms to solve and analyze problems that involve fluid flows. CFD is an effective tool which, when used either singly or in synchronization with other tools, can provide important data regarding the performance of a marine current turbine in varying flow conditions. It also obtains the turbine performance data, lift and drag that can be converted into thrust, torque and power estimates, and also pressure distribution on the device, enabling the computation of probable cavitation. CFD can give a detailed image of the flow around the turbine, leading to a more advanced outlook on potential environmental problems, such as scour, erosion and the change in tidal magnitude, and can provide important data concerning the positioning of MCTs arrays [26]. Figure (2.4) illustrates the process of CFD modeling process for HAMCT. Published CFD studies do not always report all the details of the CFD modeling process. Some papers lack information about some steps making the reproducibility of model results very difficult.

Figure (2.4) The CFD modeling process

2.4 Review of 2D studies

Historically, Two-dimensional methods were first developed to solve the Linearized Potential equations. Later on, the Two-dimensional methods, using conformal transformations of the flow about a cylinder to the flow about a hydrofoil, were developed in the 1930s. The existing computer power at the time paced the development of three-dimensional methods.

For hydrofoil design, codes such as XFOIL, use a conformal transformation and an inverse panel method. XFOIL is a linear vorticity 15 stream function panel method with a viscous boundary layer and wake model [54]. It has been recognized to be suitable for producing section performance data and cavitation criteria for a marine current turbine at the preliminary design stage, however care should be taken to recall the apparent underestimation of drag and the overestimation of leading edge pressure coefficient [55]. Some two-dimensional analysis codes also show fundamental section structural characteristics, such as second moment of area, with minor modifications to the base section made within the program. These data can be used for the basic structural analysis of the turbine blade, which is vital at early stage of the design process [56].

Two-dimensional CFD models are quite mainstream in MCT research. Many researchers use 2D models to conduct parametric optimization and design. Goude and Agrene used the 2D vortex method to compare the hydrodynamic performance of single and double turbine-systems. They studied the NACA0021 hydrofoil. They found that The two-turbine system had highest coefficient per turbine than single turbine [57]. Kevadiya and Vaidya used a 2D CFD model to study the effects of varying angle of attack on the hydrodynamic performance coefficients for hydrofoil NACA4412. They found that the Lift/Drag ratio increases with increase in angle of attack up to 8°. After 8°, Lift/Drag ratio decreases with increase in angle of attack [58]. Wang et al [59] compared the hydrodynamic performance of five hydrofoils under varying angle of attack. They used a 2D Lattice Boltzmann Method (LBM) solver. They found that the flow around the hydrofoil is greatly related to the angle of attack. They pointed out that as the angle of attack increases, trailing-edge vortex is gradually produced on the wing back.

Shiu et al conducted a parametric 2D CFD study to design of a new hydrofoil family for HAMCT. Compared to NACA 44 foils of equivalent thickness, their newly developed MHKF1-180 and MHKF1-240 foils had better left-to-drag ratio and lower susceptibility to cavitation and noise [60]. Nedyalkov and Wosnik investigated the performance of bi-directional hydrofoils using 2D CFD modeling. They showed that bidirectional foils may provide a more cost-efficient way to account for the bi-directionality of the tidal currents, as no yaw or pitch control is required for horizontal-axis turbines utilizing blades with such shapes [61]. Karthikeyan et al [62] analyzed two design parameters primarily responsible for the hydrodynamic performance of HAMCT. There are blade pitch-angle and number of blades per rotor. They found that, changing the blade pitch-angle and reducing the number of blades can improve the turbine's coefficient of power. That is due to increase in lift and reduction of losses caused by turbulence near the downstream of the turbine.

Two-dimensional analyses prove themselves to be powerful tools at the preliminary design stage for a tidal turbine and they should not be underestimated at the preliminary design stage. Yet, it is obvious that, for more integral design information, a more complex code eligible of modeling more complex situations in three dimensions is needed.[63].

2.5 Review of 3D studies

More detailed analysis of the performance of the turbine can be achieved by three-dimensional CFD models. 3D models calculate the hydrodynamic characteristics over the surface of the blade (and rotor in full models) under analysis to produce a pressure distribution and lift and drag data. These models can be employed as a more in-depth prediction of cavitation inception on the turbine blades and also as a source of detailed blade loading data for further structural calculations. 3D models are more computationally powerful than two-dimensional models since they capture more realistic hydrodynamics, however they are more difficult to perform and validate. It is possible to reproduce the helical wake characteristic of marine current turbines when using proper turbulence modeling approach to get a much more detailed picture over simulation [21, 54].

Lawson et al [64] used 3D CFD model to develop a methodology for predicting the lift and drag coefficients, bending moments and center of pressure in the turbine rotor. They found

that the velocity along the direction of the y-axis decreases considerably as the flow approaches the turbine rotor. Chen and Lam [65] investigated the slipstream between the seabed and the marine current turbine using a 3D CFD model. The axial component of velocity is the dominating velocity of flow below marine current turbine. Henriques et al [66] used 3D CFD to design, analyze and predict hydrokinetic performance of HAMCT with and without extreme gravity waves. By increasing the installation depth of HAMCT from the free surface, they showed that shaft loads and power coefficient of the turbine oscillate respectively. Otto and Vaz [67] investigated the flow structure around MCT using 3D CFD model. They found that large separation zones at the suction side of the blade are developed at low Reynolds number. Ikoma et al [68] used 3D CFD model to explore the possibility of improving the torque performance of a vertical axis MCT. Based on the cyclic pitching of turbine blades, their results suggested that significant increase in average turbine torque is possible. Li et al [69] studied the bidirectional characteristics on tidal current runner. Their research showed that the efficiency of the reversible turbine is lower than that of the turbine with standard hydrofoil. They also showed that the dynamic performance is completely identical between positive condition and reverse condition in bidirectional operation. Goude et al [70] used 3D CFD modeling framework to investigate three MCT configuration were studied: one turbine vertically aligned, and two horizontally aligned turbines rotating with opposite direction. The results show that the difference depends both on how much the velocity varies over the velocity profile, and on the shape of the velocity profile, where a linear profile causes a lower pressure coefficient (C_p) compared to a logarithmic profile.

2.6 Turbulence Modelling

Most flows of practical engineering interest are turbulent, and the turbulent mixing of the flow usually controls the behavior of the fluid. The turbulent nature of the flow plays an important role in the determination of many relevant engineering parameters, such as frictional drag, flow separation, transition from laminar to turbulent flow, thickness of boundary layers, extent of secondary flows, and spreading of jets and wakes. It is possible to solve the Navier Stokes Equations directly without any turbulence model. This means that the whole array of spatial and sequential scales of the turbulence must be resolved. Direct numerical simulation (DNS) captures all of the relevant scales of turbulent motion. Otherwise, this process is

extremely computationally expensive for complex problems, therefore there is a need for turbulence models to represent the smallest scales of fluid motion. The choice of which turbulence model to use, however, is an extremely essential matter [21, 71].

The two-equation turbulence models are reasonably accurate for fairly simple states of strain but are less accurate for modeling complex strain fields arising from the action of swirl, body forces, such as resilience, or extreme geometrical complexity. The Reynolds stress transport models deal with the notion of turbulent viscosity and determine the turbulent stresses directly by solving a transport equation for each stress component. This form of model can solve complex strains and can withstand non-equilibrium flows. However, it has not yet been widely adopted as an industrial tool because it is complex, expensive to compute, can lead to problems of convergence and also requires border conditions for each of the new parameters being solved.

The Reynolds-averaged Navier-Stokes (RANS) equations are time-averaged equations of motion for fluid flow. They are primarily used while dealing with turbulent flows. These equations can be used with approximations based on the knowledge of the properties of flow turbulence to give approximate averaged solutions to the Navier Stokes equations. The nature of RANS equations leads to the need for complex domain discretization schemes as well as complex modeling with large numbers of elements or cells. This often leads to complex mesh structures on which the equations must be solved and building such meshes is time-consuming [21, 72].

Turbulent flows contain many unsteady eddies covering a range of sizes and time scales. The RANS equations are averaged in such a manner that unsteady structures of small sizes in space and time are eliminated and become expressed by their mean effects on the flow through the Reynolds, or turbulent, stresses. These stresses need to be interpreted in terms of calculated time-averaged variables, in order to close the system of equations, thereby rendering them solvable. This requires the construction of a mathematical model, known as a "turbulence model", involving additional correlations for unknown quantities [71].

There is limited information about the turbulence modeling of HAMCT, however, the model is widely used in different types of marine turbine CFD models. Harrison et al [73] used

it to investigate how the actuator disc of a marine *tidal* turbine would affect the overall flow using CFD modeling. They showed that the SST $k-\omega$ model predicts flow wake similar to that shown in experimental work. Lain et al [74, 75] showed how the SST $k-\omega$ model can effectively predict hydrodynamic performance of a vertical-axis marine current turbine. Liu and Hu [76] used the model to investigate the hydrodynamic behavior of a turbine operating in the wake of an upstream turbine. In comparison with the Reynolds Stress Model (RSM), Marsh et al [77] found that the SST $k-\omega$ model accurately predicted power output for most rotational rates, at a significantly reduced computational cost. Leroux et al [78] validated the model with experimental measurements of horizontal-axis tidal turbines (HATT). Their results demonstrated similar levels of agreement as the works done by Chen et al [79] and Fertahi et al [80] in terms of validation and suitability of the SST $k-\omega$ model for marine turbine simulations.

2.7 Discussion and Conclusion

The literature review revealed important information regarding the hydrodynamic performance of HAMCT. It is clear that the available information is much less than such of the wind turbines. It is also clear that the former field is much underdeveloped than other types of renewable energy turbines.

The use of two-dimensional CFD models establishes a powerful, however limited, tool for investigating HAMCT hydrodynamics. 2D models are used in literature to investigate different hydrofoil characteristics under different types of flow. 2D models are also used for optimization and selection of HAMCT hydrofoils.

The use of three-dimensional CFD models helps better understanding of the HAMCT hydrodynamics and flow structure. Although 3D models are more difficult to construct and perform than 2D models, they give better parametrization framework for manipulating HAMCT hydrodynamics and study their characteristics.

Previous works on HAMCT hydrodynamics aimed at studying their unique features and investigate the effects of design and operational parameters on the flow around the turbines and its generated power and efficiency. No previous studies were conducted to improve the

hydrodynamic performance be means of upstream flow control. Previous works were only limited to hydrofoil shape and turbine configurations.

Turbulence modeling is critical in 3D CFD models. The SST $k-\omega$ model demonstrated reliable predictions of MCT hydrodynamics in the majority of studies. Fewer number of studies have reported the use of Spalart-Almaras (SA) model [81, 82], RSM [77] and $k-\epsilon$ model [83].

Through the literature review process, only one study could be identified as a *complete* benchmark reference for this thesis. The study by Gounder et al [84] reports numerical and experimental studies are carried out on a HAMCT hydrofoil working under conditions that are very similar to the conditions of the Northern coast of Egypt, as discussed in Chapter 1. They studied the HFSX hydrofoil series using 2D, 3D CFD models and validated their work with in-house experimental platform mimicking the hydrodynamics of Fiji island shoreline.

The benchmark case, as published in Renewable energy journal, reported detailed results from CFD models and BEM analysis. The validation procedure of the present work is conducted based on the benchmark study, in addition to further references published by the same group [85-87].

CHAPTER 3

Two-Dimensional CFD Modeling of HAMCT Blade Hydrodynamics

3.1 Introduction

Energy generation from marine currents is a promising technology for sustainable development. The success of using marine current turbines to tap the ocean hydrodynamic energy depends on predicting the hydrodynamic characteristics and performance of such turbines. This chapter presents an analysis of the two-dimensional flow using commercial CFD software over a marine current turbine blade. The 2D flow is simulated for HF-SX NACA foils S1210 and HF1020 which is modified from S1210 NACA foil at various angles of attack with Reynolds number of 190,000, which represents the marine current flow.

The hydrofoils are designed with considerations for lift and drag coefficients. The flow is simulated by solving the steady-state Navier-Stokes equations coupled with the k-ω shear stress transport (SST) turbulence model. The aim of this work is to study the effect of the angle of attack on the lift and drag coefficients. The computational domain is composed of non-homogenous structured meshing, with sufficient refinement of the domain near the foil blade in order to capture the boundary layer effects. Hence, all calculations are done at constant flow velocity while varying the angle of attack for every model tested. The results have shown that the drag and lift coefficients (C_d and C_l coefficient) increases with increasing the value of the angle of attack, ratio C_l/C_d curve related on performance at the peak 6^o angle of attack.

In this chapter, curves for the lift, drag and power coefficient characteristics of the NACA foils were developed. Dependence of the drag coefficient C_d and lift coefficient C_l on the angle of attack was determined using the turbulence model. Turbulent flows are significantly affected by the presence of walls, where the viscosity of the affected region has large gradients in the solution variables and accurate presentation of the near wall region determines successful prediction of wall bounded turbulent flows. In fluid dynamics, turbulence or turbulent flow is a fluid regime characterized by chaotic, stochastic property changes. This includes low momentum diffusion, high momentum convection and rapid variation of pressure and velocity in space and time.

3.2 Analysis of Forces of MCT Blade

The main contribution of the present research work is the introduction of the VSG concept. Such concept depends on altering the flow-induced force components on the turbine by increasing the tangential force to improve the lift. Therefore, a complete understanding of the force analysis on the MCT turbine must be explained. The force analysis is important in order to explain the effects of swirl on HAMCT hydrodynamics, as shown later in the thesis.

The calculations of hydrodynamic performance measures using CFD is only possible to explain through such force analysis, as shown later in the remaining of the thesis. First the nomenclature of the hydrofoil is explained, then the force analysis is explained.

3.2.1 Hydrofoil Nomenclature

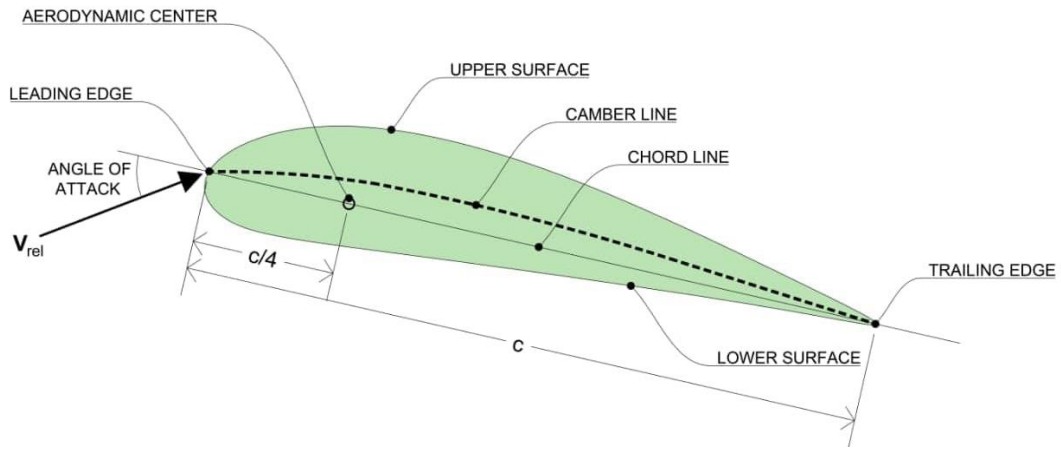

Figure (3.1) Hydrofoil nomenclature.

A specific description of a hydrofoil and its nomenclature is given in Figure (3.1) A hydrofoil actually has an upper and a lower surface. In the majority of the hydrofoils, the curvature of the lower surface is less than that of the upper surface. The intersection points of both surfaces at the front and back regions are known as leading and trailing edges, respectively. Chord line is the line connecting the leading and the trailing edges; its length is denoted by c. Camber line is the line which is the locus of the mid-points

between the upper and the lower surfaces of a hydrofoil, and is defined as the vertical distance between the chord line and the camber line, the greatest value of that distance is called the maximum camber. The thickness of the hydrofoil is measured by the distance between the upper and the lower surfaces measured perpendicular to the chord line. The geometric angle between the relative velocity vector, Vrel and the chord line is called the angle of attack (AOA) and is denoted by α. The span is defined as the perpendicular distance of the blade relative to the cross section [88, 89]. Hydrofoils are mostly numbered by using a few parameters such as the maximum camber, the maximum thickness, the position of the maximum camber, the position of the maximum thickness, and the nose radius. And also, hydrofoils are identified by the coordinates of both the upper and lower surfaces [90]

3.2.2. Hydrodynamic Forces

A hydrofoil immersed in a stream flow is subjected to numerous forces due to pressure and velocity changes and the viscosity of the fluid. The description of the forces on a hydrofoil section is given in Figure (3.2). The forces affecting the hydrofoil are drag force, F_D, lift force, F_L and pitching moment, M_P. The force that is exerted on the body by the fluid, parallel to the flow direction is called drag force, which is generated from the viscous friction and the unequal pressures at the hydrofoil surfaces [89]. When the fluid moves over the hydrofoil, due to the camber and the angle of attack, the velocity of the fluid particles at the upper surface becomes higher than that of lower surface. Low pressure zone is generated at the upper surface of the hydrofoil due to high flow velocity while the lower surface produces a high pressure zone due to lower flow velocity. Thus, a lift force is generated due to the unequal pressure distribution between two surfaces of hydrofoil. The lift force direction is normal to the chord line. Likely, the pitching moment is created as a function of the integral of the moments of pressure forces over the surfaces of the foil. The application point of these three loads on the hydrofoil is mostly reasonable to be at $c/4$ distance from the leading edge on the chord line [91]. The hydrodynamic forces change and are affected by the flow velocity, density of the fluid and the frontal area as well as the size, the shape and the orientation of the body [92].

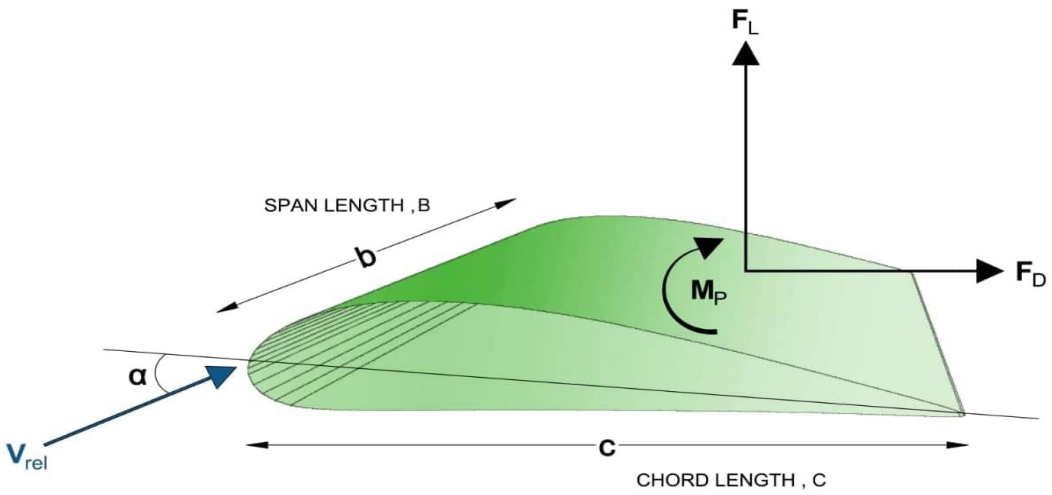

Figure (3.2) The resultant loads on hydrofoil

3.2.3 Angle of Attack (AOA)

If a person puts his arm out through the window of car that is moving at a high speed, he can feel his arm pushed backward. If he holds his arm straight with his hand parallel to the road, and changes the angle slightly, he can suddenly feel that it is drown upwards. The hand and arm work in the same way as the wing of an airplane and with the right angle of attack, he can feel a strong lift force. AOA is the angle between the incoming flow and a reference line on the airplane or wing, as shown in figure (2.3). Most commercial jet airplanes use the airplane body as center line or longitudinal axis as the reference line [93]. It makes no difference what the difference line is as long as it is used consistently. As the nose of the wing turns up, AOA increases, and lift increases. Drag goes up also, but not as quickly as lift. During take-off an airplane reaches up to a certain speed and then the pilot "rotates" the plane that is, the pilot uses the controls so that the nose of the plane comes up and, at some AOA, the wings generate enough lift to take the plane into the air. Since the wing is fixed to the airplane body, the whole plane has to rotate to increase the wing's angle of attack [93].

3.2.4 The Effect of Reynolds Number and Angle of Attack

The Reynolds number (Re) has a great importance on the behavior of the foils. The relative magnitude of the viscous forces becomes more than the inertial forces if the Re number decreases. This leads the surface friction and pressure gradients to increase. This process will result in increasing the drag coefficient and reducing the lift coefficient [89]. In uniform foils, the lift coefficient Cl is equal to zero at zero angle of attack (α). At small angle of attacks, the lift coefficient is of small value and starts to increase linearly with increasing the angle of attack. While, Cl can be increased at small α by using a cambered foil [89, 94]. After α reaches a certain point a sudden drop happens in the foil performance and then it stalls. This point is known as maximum lift. For negative angle of attacks, the lift behavior of the foil is approximately the same [89, 94]. Mostly, the drag coefficient increases with the increase in angle of attack.

3.2.5 Coefficient of Drag and Coefficient of Lift

The coefficient of drag is defined as:

$$C_d = 2F_d/\rho A v^2 \quad (3.1)$$

where F_d is the drag force on a blade, ρ is the fluid density and v is the free-stream flow velocity. In fluid dynamics the C_d is a dimensionless quantity that is used to measure the drag or resistance of an object in a fluid environment such as air or water. C_d is used in the drag equation where a lower drag value coefficient indicates the object will have less aerodynamic or drag [89, 93]

The coefficient of lift is defined as:

$$C_l = 2F_l/\rho A v^2 \quad (3.2)$$

where F_l is the lift force acting on the hydrofoil. A fluid flowing across the surface of a body produces a force on it. Lift force is the component of this force that is perpendicular to the oncoming flow direction. It differs from the drag force, which is the component of the surface force parallel to the flow direction. If the fluid is air, the force is called an aerodynamic force [89].

3.3 Mathematical & Numerical Details

For all incompressible flows, the solver solves conservation equations for mass and momentum. Additional transport equations are also solved when the flow is turbulent. The equation for conservation of mass or continuity equation can be written as follows:

$$\frac{\partial \rho}{\partial t} + \nabla . (\rho \vec{u}) = S_m \quad (3.3)$$

Equation (3.5), is the general form of the mass conservation equation and is valid for incompressible flows. The source S_m is mass added to the continuous phase from the dispersed second phase and any user-defined sources. Conservation of momentum in an inertial reference frame, described by equation (3.5) [95].

$$\frac{\partial}{\partial t}(\rho \vec{u}) + \nabla . (\rho \vec{u} \vec{u}) = -\nabla p + \nabla . \left(\overline{\overline{\tau}}\right) + \rho \vec{g} + \vec{F} \quad (3.4)$$

where ρ is the static pressure, $\overline{\overline{\tau}}$ is the stress tensor and $\rho \vec{g}$ and $\vec{F}$ are the gravitational body force and external body forces. $\vec{F}$ Also contains other model-dependent source terms such as porous- media and user defined sources.

The commercial software ANSYS (i.e. FLUENT) is used for CFD model discussed below. Continuity and momentum equations are solved for all types of flow via a finite-volume method. To account for the effects of turbulence, a variety of models are available, ranging in complexity from one-equation models to LES. The turbulence models used in this work belong to the standard k-ω SST model [95]:

3.3.1 Turbulence Modeling

In the following sections of this chapter, six different turbulence models are examined to demonstrate the appropriateness of the SST $k - \omega$ model in transitiona flow regime. These models are of the RANS type of turbulence models. The five models compared to the SST $k - \omega$ model are three versions of the $k - \epsilon$ model, the Reynolds stress model, the Spalart-Almaras (SA) model. All these models are well-established in turbulence modeling methods in CFD.

In order to make the thesis brief and concise, the detailed transport equations of the tubrulence models have been skipped here. The detailed equations are available in ANSYS Theory Guide [96]. Only the SST $(k-\omega)$ model, which is specifically derived for transitional flow is explained.

The transport equations (3.7) and (3.8) for the standard k-ω model equations are given below,

$$\frac{\partial}{\partial t}(\rho k)+\frac{\partial}{\partial x_i}(\rho k u_i)=\frac{\partial}{\partial x_i}\left(\Gamma_k \frac{\partial k}{\partial x_j}\right)+G_k-Y_k \tag{3.5}$$

$$\frac{\partial}{\partial t}(\rho \omega)+\frac{\partial}{\partial x_i}(\rho \omega u_i)=\frac{\partial}{\partial x_i}\left(\Gamma_\omega \frac{\partial \omega}{\partial x_j}\right)+G_\omega-Y_\omega \tag{3.6}$$

where,Γ_k, G_k and Y_k are the diffusivity, generation and dissipation of turbulent kinetic energy and Γ_ω, G_ω and Y_ω diffusivity, generation and dissipation of ω.

The k-ω model accounts for Re effects in the inner region of the boundary layer but is highly sensitive to the values of k and ω in the free stream. The SST k-ω model couples the standard k-ω model with a modified version of the k-ε model via a blending function. The transport equations for the SST k-ω model were developed by Menter. The expressions for the terms Γ_k, G_k, Y_k, Γ_ω, G_ω and Y_ω are different with different constants and limiters for the turbulent viscosity and production of kinetic energy. The revised model constants are based on experience [95, 97].

There is also an additional cross-diffusion term in the equation which arises from the modification of the k-ε model into equations based on k and by substitution of ε with k-ω. This term is given below in equation (3.9),

$$D_\omega=2(1-F_1)\frac{1}{\omega\sigma_{\omega,2}}\frac{\partial k}{\partial x_j}\frac{\partial \omega}{\partial x_j} \tag{3.7}$$

where F_1 is a blending function and the empirical constant ($\sigma_{\omega,2}=1.17$).

Through blending both models, the SST k-ω model incorporates the advantages from both the standard k-ω model and the k-ε model, giving more accurate and reliable predictions for many types of flow, including the flow over a foil [98].

3.4 NACA Four-Digit Hydrofoil Profile

In this work, the HF1020 NACA foil is utilized, Figure (3.4). The NACA X foil series uses the same thickness forms as the 4-digit series, but the mean camber line is defined differently. The final two digits indicate the maximum thickness (t) as percentage of chord [99].

3.4.1. Calculation of the Hydrofoil Coordinates

Compute the mean camber-line y_c ordinate for each x position, using the following equations. Using geometry of the blade to determine the values of p, m and k_1:

$$y_c=((k_1 m^3)/6)\,(1-x);\ \text{for } x>p \qquad (3.8)$$

The final coordinates for the foil upper surface (x_u, y_u) and lower surface (x_L, y_L) are given by:

$$x_u \equiv x - y_t(\sin\theta)$$

$$y_u \equiv y_c + y_t(\cos\theta)$$

$$x_L \equiv x + y_t(\sin\theta)$$

$$y_L \equiv y_c - y_t(\cos\theta)$$

Where $\theta = \arctan(\Delta y_c/\Delta x)$

The chord length is 1 m and domain height is set to approximately 20 chord lengths. This size should be sufficient to properly resolve the inner parts of the boundary layer.

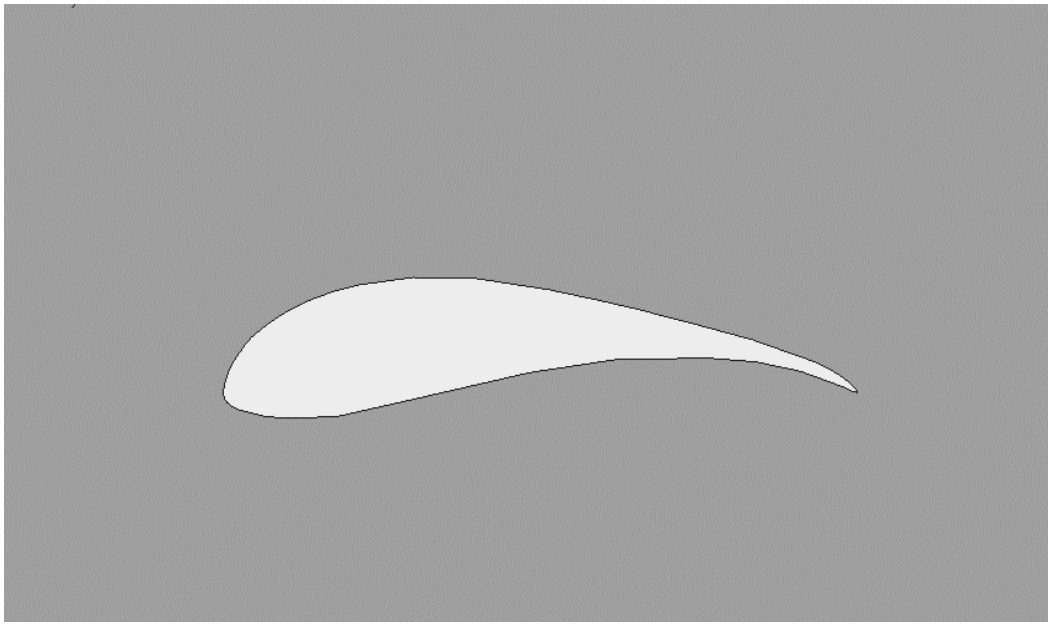

Figure (3.4) NACA HF1020 foil

3.4.2 CFD Model and mesh generation

The first step in modelling a problem involves the creation of the geometry and the meshes with a pre-processor. The majority of time spent on CFD project in the industry is usually devoted to successfully generating a mesh for the domain geometry that allows a compromise between desired accuracy and solution cost. After the creation of the grip, a solver is able to solve the governing equations of the problem. The basic procedural steps for the solution of the problem are the following. First, the modelling goals have to be defined and the model geometry and grid are created. Then, the solver and the physical models are stepped up in order to compute and monitor the solution. Afterwards, the results are examined and saved and if it is necessary revisions are considered to the numerical or physical model parameters [100].

CFD model of NACA HF1020 is meshed by ANSYS ICEM CFD, as shown in Figure (3.5). For converged solution and saving calculation time, model is meshed by hexa-element. Fine mesh and small element with inflation at location are close to NACA shape. Element size grows along two axes from NACA shape to boundaries [85]. To get optimal results, the criteria of elements are very important, and number of element of

best quality mesh is less than bad mesh. Assessing the quality of good or bad grid will be evaluated by: a) Skewness Ratio, acceptable value is less than 0.54, ideal is 0, b) Aspect Ratios, acceptable value is less than 1.5, ideal is 1, c) the Jacobian Ratio is 1 and d) Warpage are 0 deg. If parameters of mesh are close to these criteria, result can be converged [101]. Meshing process depends heavily on the experience of the engineer, especially in using the meshing method and element size.

The model is a closed domain, and all boundaries are open. Except for the inlet boundary, the outlet boundary and wall of NACA shape, inlet is set by a velocity of 3m/s for S1210 and 2m/s for HF1020, gauss pressure is zero, and turbulent intensity is 2.8%. Outlet is set by gauss pressure of zero, turbulent intensity is 2.8% and wall is NACA shape [84, 85]

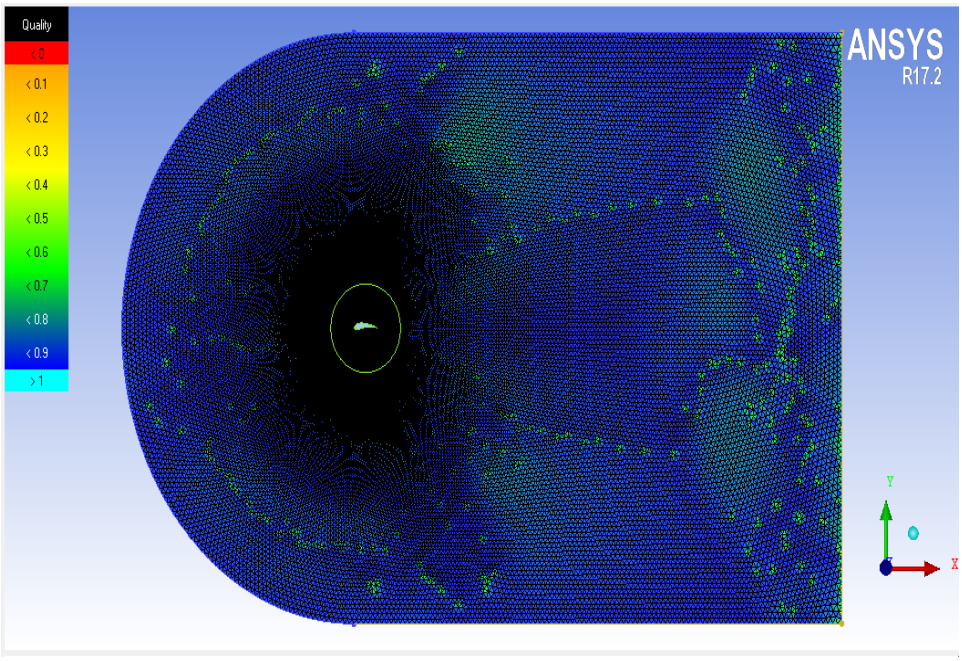

Figure (3.5) Computational domain and meshing in ICEM NACA HF1020

For S1210, the mesh is generated with 90400 elements and 91000 nodes. All of elements are quad-elements. For HF1020, the mesh is generated with 194981 elements and 99936 nodes. All of elements is Hexa-elements. The quality of mesh is shown as table of mesh criteria.

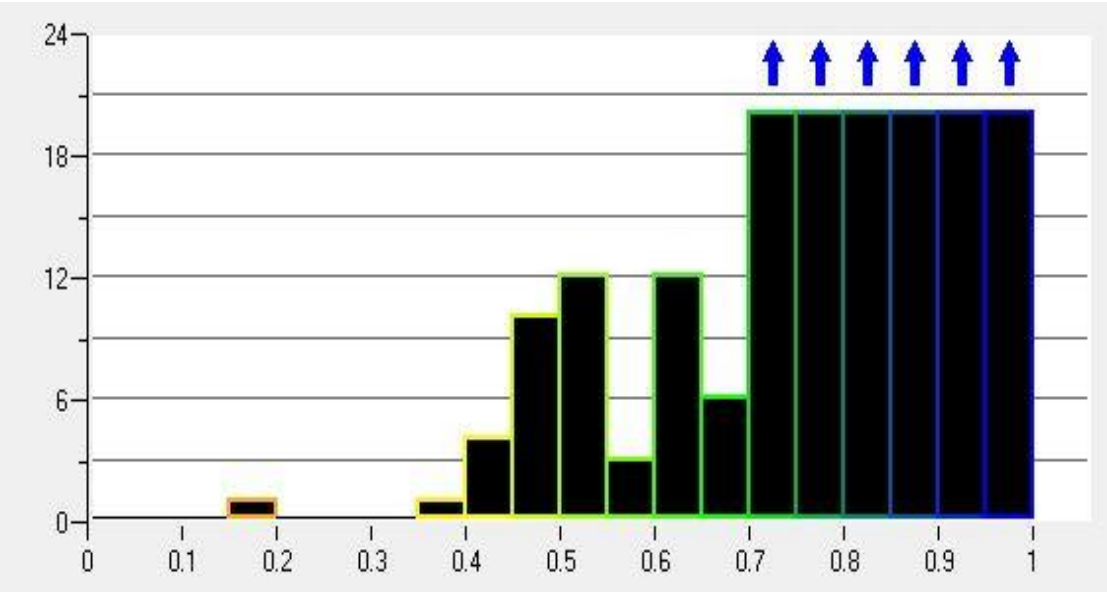

Figure (3.6) Mesh quality for HF1020

The quality of mesh can show that the result is acceptable as shown in figure (3.6). Maximum of Skewness ratio is 0.43. This is the main criteria for CFD mode [85]. The Reynolds number can be calculated by:

$$Re = \frac{(Inertial\ forces)}{Viscous\ forces} = \frac{(mass)(acceleration)}{(dynamic\ viscosity)\left(\frac{velocity}{distance}\right)} = \frac{\rho v L}{\mu} \qquad (3.9)$$

From Reynolds number, two parameters of turbulent flow can be calculated, turbulent intensity of CFD model is formulated as follows [102] :

$$I = 0.16 \times (Re)^{-1/8} \qquad (3.10)$$

where *Re* is the Reynolds number, I is the turbulent intensity, thus, the value of intensity is 2.489965%.

3.4.3 Mesh Sensitivity Analysis: Verification

Mesh optimization is done by many solving trials with different values of mesh elements to choose the optimum value which gives results near to the experimental C results of the benchmark study, the curves shown below in Figure (3.7), show the grid independence study for mesh elements.

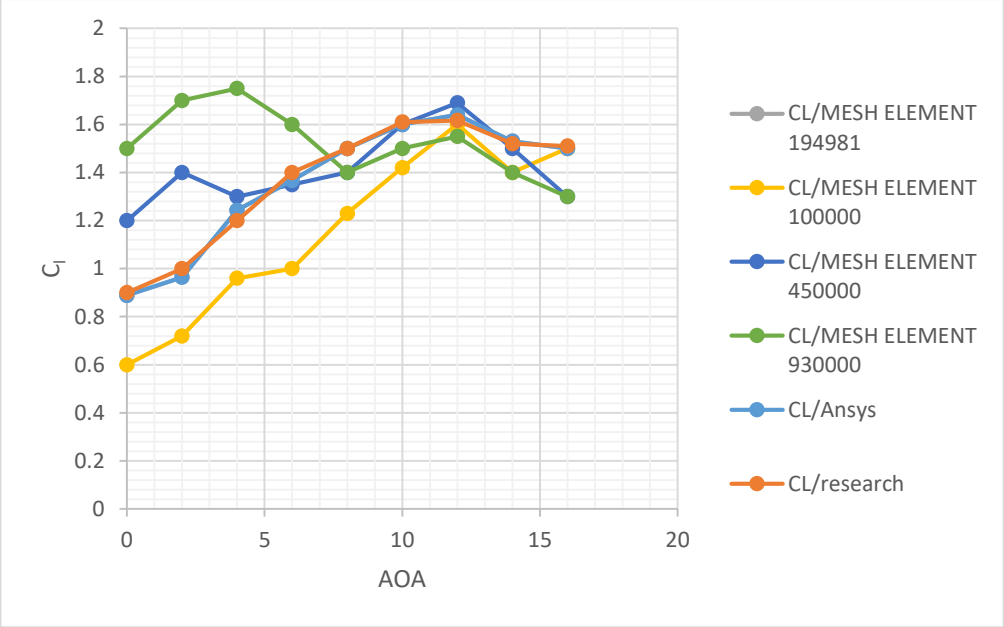

Figure (3.7) Mesh optimization for NACA HF1020

Operation of solving process is set by absolute pressure, reference temperature. Model of NACA HF1020 is simulated in case of depth of 91 m from sea water level [103]. So, hydrostatic pressure in this case is absolute pressure, and it is calculated by the following formula [104, 105].

$$P_{absolute} = P_{hydrostatic} + P_{atmospheric} = g \times \rho \times h + 101325(Pa) \qquad (3.11)$$

Where, g is gravitational acceleration (m/s^2), p is density of water (kg/m^3) and h is depth (m); the absolute pressure is 992426.122 (Pa) and reference temperature is $295\ K$ [106]. In order to validate the present simulation, the Re is 1.9×10^5; velocity of water investigated is 2 m/s; the density of the water at given temperature is 998 kg/m^3; and the viscosity is $0.00103\ Pa.s$. This is an assumption close to reality and it is not necessary to resolve the energy equation. A segregated, implicit solver is utilized. Calculations were done for angles of attack ranging from 0 º to 15º. The foil profile, boundary conditions and meshes were all created in the pre-processor ICEM. The pre-processor is a program that can be employed to produce models in two dimensions, using structured meshes, which can consist of all quadrilateral elements.

The resolution of the mesh is greater in regions where greater computational accuracy is needed, such as the region close to the foil. Nodes also increase the required computer memory and computational time. The appropriate number of nodes can be determined by increasing the number of nodes until the mesh is sufficiently fine so that further refinement does not change the results [107]. The boundary and initial conditions for the 2D CFD models are shown in table (3.1).

Table (3.1) Details of the boundary and initial conditions of the 2D CFD models

Boundary / Initial condition	Settings	Value (unit)
Inlet velocity	Constant velocity	2 m/s
Inlet turbulence intensity	Percentage and hydraulic diameter	2.48%
Outlet pressure	Constant pressure	0.9 MPa
Water density	Constant density (incompressible flow)	998 Kg/m^3
Water viscosity	Constant viscosity	0.00103 Pa.s
Meshing	tetrahedral	194981 cells
Convergence criteria	Residuals	10^{-6}
Spatial discretization	2^{nd} order upwind	--
Time discretization	None, steady	--
Turbulence model	SST $k-\omega$	--

3.5 Establishing the 2D CFD Model of HAMCT Hydrodynamics

On a foil, the resultants of the forces are usually resolved into two forces and one moment. The component of net force acting normal to the incoming flow stream is known as lift force and the component of the net force action parallel to the incoming flow stream is known as the drag force. The curves of the lift and the drag coefficient are shown for various angles of attack. Simulations for various angles of attack were done in order to be able to compare the different C_l and C_d coefficients. Accordingly, the model is solved with a range of angle of attack from 0 to 15º. For each simulation, the results are calculated from numerical data and solution converge after 347 iterations. Numerical values show that C_l is 1.0530 and C_d is 0.01509 at zero-

degree angle of attack. For high quality of mesh, the solution is converged where the value is accepted. From these values, the graph will be plotted, thereafter a holistic view of the dependence of lift coefficient and drag coefficient on the angle of attack can be determined. Hence, it can determine the best angle of attack and design turbine blades to get highest efficiency. Also, from results, we can get contour of pressure, velocity around NACA shape and the maximum value and minimum value of each variable. Contour of pressure shows locations that have maximum pressure; also, it can be noticed that the separation point, transition point, location have turbulent flow, which causes a cavitation phenomenon.

In figure (3.8-a) it's clear that for the S1210 NACA foil, at angle of attack 0^o, flow is symmetric with respect to the blade chord. On the other hand, the NACA HF1020 hydrofoil has asymmetric flow at angle of attack 0^o, figure (3.8-b). This is observed by depicting the pressure distribution at the suction and compression sides of the airfoil. However, to determine the cases with highest ratio, it is a must to get the numerical values at top and bottom surface of NACA shape.

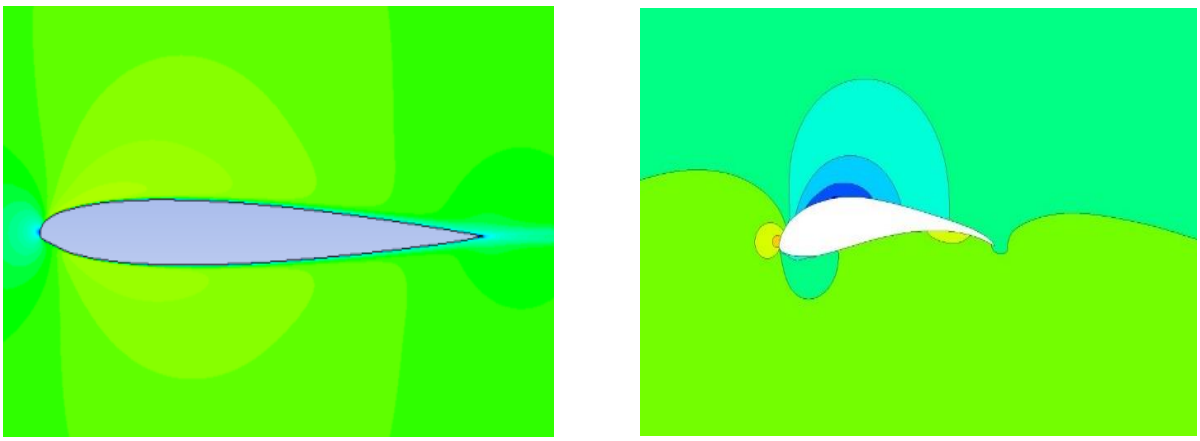

(a) (b)

Figure (3.8) Pressure contours at AOA zero (a) S1210 (b) HF1020

To choose the best turbulence model to use in the simulation, a lot of trials have been done on SST $k-\omega$, RSM and SA turbulence models. Only the SST $k-\omega$ model was able to achive the required converegence criteria. The other two models showed oscillations in the

residuals history and did not achieve the required convergence criteria. The following results are all obtained using the SST $k-\omega$ model.

3.5.1. Turbulence Models Comparison and Validation of the 2D-CFD Model

In order to test different turbulence models and decide which model to use with the transitional flow conditions (Re = 190,000), 54 simulations cases were conducted in parametric settings. The comparison between turbulence models included three versions of the fully-developed turbulence model $k-\epsilon$ (standard, realizable and RNG) in addition to the Spalart-Almaras (SA), Reynolds stress (RSM) and SST $k-\omega$ models. The results of the coefficients of drag and lift (C_d, C_l) were compared to the experimental measurements of the benchmark case[84].

Table (3.2) lists the values of C_l calculated by different turbulence models compared to experimental measurements and shows the error percentage for each set of results. Some of the models did not converge in all cases, as shown in the table. It can be seen that all three $k-\epsilon$ models had large error range varying from 0.07% to 142.6%. The SA model had error range varying from -0.64% to 91%. The RSM model had error range varying from -19% to 154.97%. The SST $k-\omega$ had the least range of error varying from 15.7% to 28.5%. The non-converged cases were not considered in estimating the limits of error range. Only the $k-\epsilon$ RNG and SST $k-\omega$ models converged in all cases.

Table (3.2) (a) Comparison of different turbulence models calculations of the lift coefficient(C_l). Each record represents a simulation case. Records shaded in red colour have not converged during solution. (b) Error percentage for each model compared to experimental measurements. Positive (+) and negative (-) signs represent over- and under-prediction, respectively.

(a)	(C_l)						
Angle	Exp	k-epsilon (STD)	k-epsilon (RLZ)	k-epsilon (RNG)	SA	RSM	SST k-omega
0	0.91	2.65	2.57	2.09	1.74	2.32	1.05
2	1.10	2.68	2.67	2.27	1.76	4.35	1.40
4	1.30	2.75	2.64	2.19	1.80	2.62	1.53
6	1.40	2.79	2.69	1.09	1.86	1.19	1.80
8	1.55	2.78	2.71	2.34	1.89	5.74	1.90
10	1.65	2.71	2.64	2.37	3.92	1.34	1.93
12	1.69	2.51	2.63	2.30	1.71	1.72	2.05
14	1.60	2.14	2.13	3.21	1.59	7.32	1.98
16	1.59	3.55	1.59	1.71	9.27	6.42	1.90
(b)	Error %						
Angle	Exp	191.44%	182.13%	129.52%	91.02%	154.97%	15.71%
0	0.91	144.01%	142.66%	106.44%	59.80%	295.06%	27.27%
2	1.10	111.51%	103.15%	68.67%	38.83%	101.76%	17.69%
4	1.30	98.96%	92.15%	-22.38%	32.71%	-15.09%	28.57%
6	1.40	79.63%	74.75%	51.20%	22.26%	270.00%	22.58%
8	1.55	64.24%	60.13%	43.37%	137.52%	-19.00%	16.97%
10	1.65	48.46%	55.33%	35.89%	1.05%	2.07%	21.30%
12	1.69	33.66%	33.04%	100.58%	-0.64%	357.74%	23.75%
14	1.60	123.50%	0.07%	7.35%	482.99%	303.92%	19.50%
16	1.59						

Another comparison for showing different turbulence models performance with respect to coefficient of drag (C_d) is shown in table (3.3). The percentage of error in the C_d calculations by the fully-developed turbulent flow models is extremely high due to the complex flow structure associated with transitional flow. Such complex structure cannot be captured with these models due to the assumptions in their equations. However, the SST $k-\omega$ model calculated very good values of C_d compared to experiments with error percentage varying from

-9% to -17.14%, as shown in the table. The transtional flow structure predicted by the SST $k-\omega$ is shown by means of pressure and vorticity contours later in this chapter.

Table (3.3) (a) Comparison of different turbulence models calculations of the drag coefficient(C_d). Each record represents a simulation case. Records shaded in red colour have not converged during solution. (b) Error percentage for each model compared to experimental measurements. Positive (+) and negative (-) signs represent over- and under-prediction, respectively.

	(C_d)						
Angle	Exp	k-epsilon (STD)	k-epsilon (RLZ)	k-epsilon (RNG)	SA	RSM	SST k-omega
0	0.02	8.72	8.39	1.11	5.98	2.43	0.02
2	0.023	7.74	5.23	9.49	6.55	2.35	0.02
4	0.026	4.89	5.68	8.91	5.29	2.61	0.02
6	0.028	1.98	2.88	5.72	3.07	2.35	0.02
8	0.03	1.92	7.49	3.34	1.79	2.23	0.03
10	0.033	6.75	5.61	7.94	9.14	2.10	0.03
12	0.043	1.22	9.04	5.71	8.26	5.67	0.04
14	0.084	1.79	1.66	1.08	9.82	7.54	0.08
16	0.13	2.81	2.19	1.64	1.60	5.96	0.11
Angle		Error %					
0		43493.25%	41868.70%	5466.35%	29807.75%	12051.45%	-15.00%
2		33535.00%	22619.61%	41165.74%	28369.52%	10119.26%	-17.39%
4		18693.69%	21754.31%	34160.46%	20232.35%	9925.54%	-15.38%
6		6971.46%	10169.82%	20330.50%	10851.11%	8301.93%	-14.29%
8		6301.20%	24866.50%	11047.17%	5857.83%	7318.00%	-13.33%
10		20365.82%	16894.91%	23945.55%	27596.30%	6262.91%	-9.09%
12		2741.70%	20933.26%	13176.88%	19104.67%	13095.28%	-18.60%
14		2034.71%	1875.71%	1184.27%	11585.68%	8875.50%	-7.14%
16		2059.13%	1581.14%	1159.42%	1131.67%	4487.26%	-15.38%

Figure (3.9) shows relationship between C_l and angle of attack. The C_l is directly affected by angle of attack, at angle of 0-degree, C_l = 1.053 which is minimum value, at angle of 5 degrees, C_l = 1.5991, at 10 degrees, C_l is 1.9364 and at 15 degrees, C_l is 1.958. In general, the lift coefficient increases with the increase of angle of attack. In addition, the lift coefficient is proportional to angle of attack where the trend of curve is reduced

when angle of attack increases, which means that the rate of increasing of lift coefficient is decreased when angle of attack increases more than the value of 12º.

To further indicate the agreement of lift and drag coefficients calculated by the SST $(k-\omega)$ model and experimental results of NACA HF-SX[84, 85], the results are presented graphically in figures (3.9) and (3.10). The numerical results of C_l and C_d are in qualitative and quantitative agreements with experimental results.

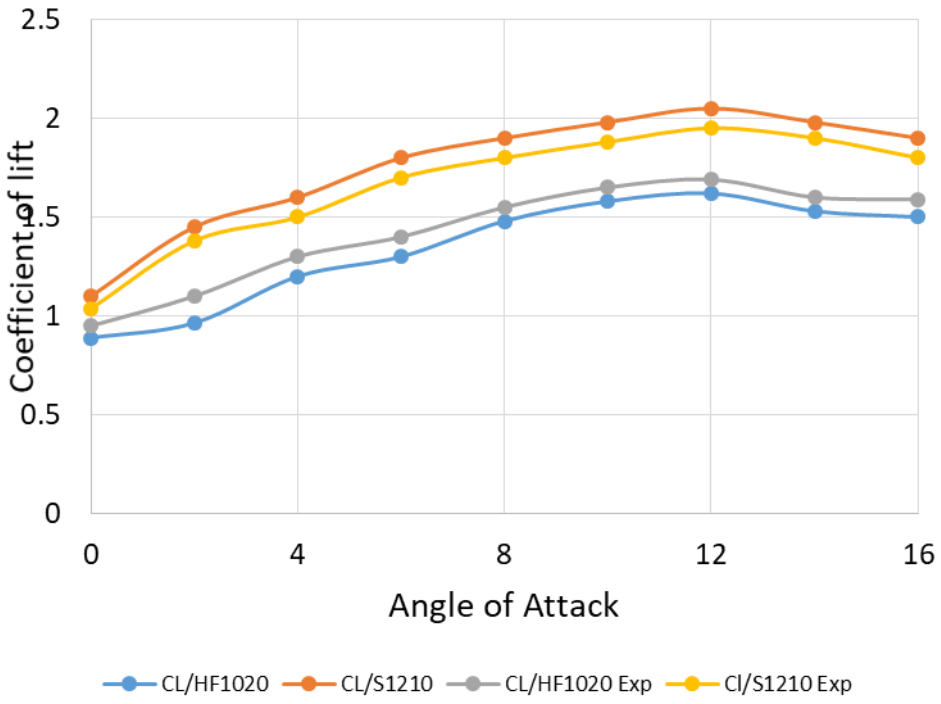

Figure (3.9) Cl for NACA S1210, HF1020, experimental[84]

Figure (3.10), shows the relationship between C_d at different angles of attack. At angle of 0-degree C_d = 0.01509 (i.e. minimum value of C_d); at angle of 5-degree C_d = 0.01868; at 10 degrees, C_l is 0.02938 and at 15 degrees, C_l is 0.08203. The peak of the ratio C_l/C_d is at around 7 º angle of attack, as shown in from Figure (3.10) below. Similar to the lift coefficient, the drag coefficient also increases with angle of attack. In spite of this curve being non-linear, it is similar with lift coefficient curve, and it covariates too, so the drag coefficient is proportional to angle of attack. Also, slope of curve is increased

when angle of attack increases, because the speed of increasing of lift coefficient will be increased when angle of attack increases.

Based on drag coefficient curve ,figure (3.10) of proposed model and experimental results of NACA HF-SX [87], the drag coefficients are proportional to angles of attack. The trend of proposed model and experimental results relatively agree [84]. Moreover, magnitude of lift coefficient at angle of attack levels is also nearly equal; e.g., at 15 degrees in two models, drag coefficients values are about 0.08.

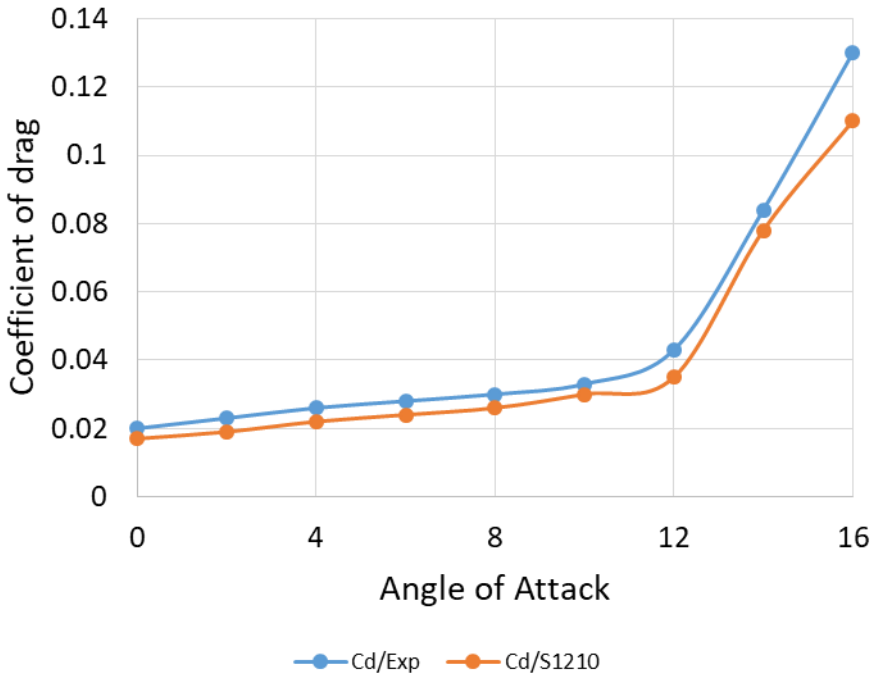

Figure (3.10) C_d for NACA S1210, experimental[84]

3.5.2 Error Analysis for the SST $k-\omega$ Model Calculations

Since the SST $k-\omega$ model calculated hydrodynamic performance parameters that was found to have very good agreement with experimental results, only this model had been used in this research. In order to evaluate the overall impact of CFD error on the simulations, a comparison between the hydrodynamic performance ratio is shown in figure (3.11). The comparison shows the ratio C_l/C_d at different angles of attack for the CFD simulations and the experimental measurements of the benchmark case[84].

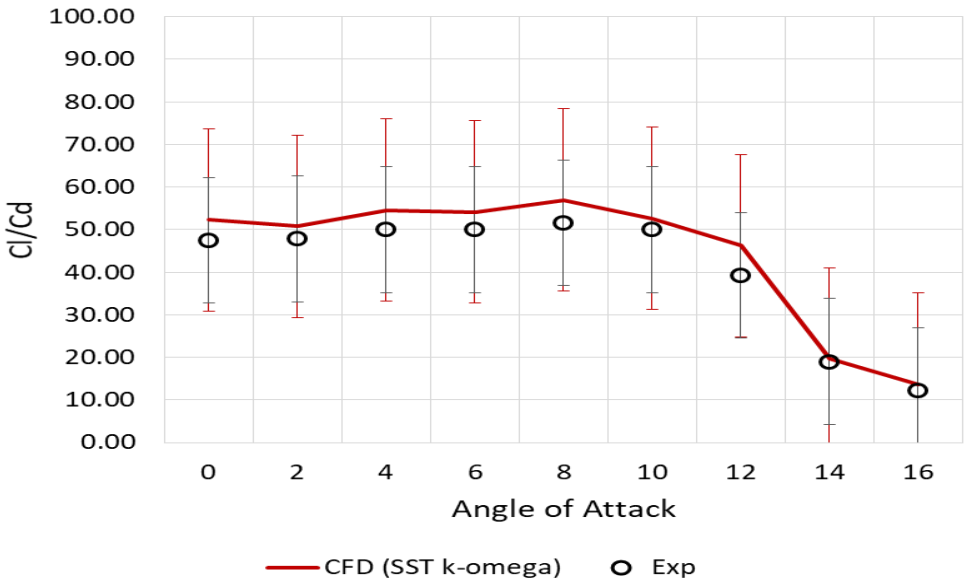

Figure 3.11 Comparison between the hydrodynamic performance ratio (C_l/C_d) for the CFD simulations and experimental measurements[84]. Average and standard deviation values of the CFD and reference datasets are 44.54±16.16 and 40.84±14.82. Error bars represent standard deviation.

Also, figure (3.12) below, shows the values for error percentage difference between the simulated HF1020 foil and the compared experimental values for C_l from the experimental results for the other research [84]. A maximum error is at AOA of 2 degrees which equals 3.56%, which is acceptable value for error.

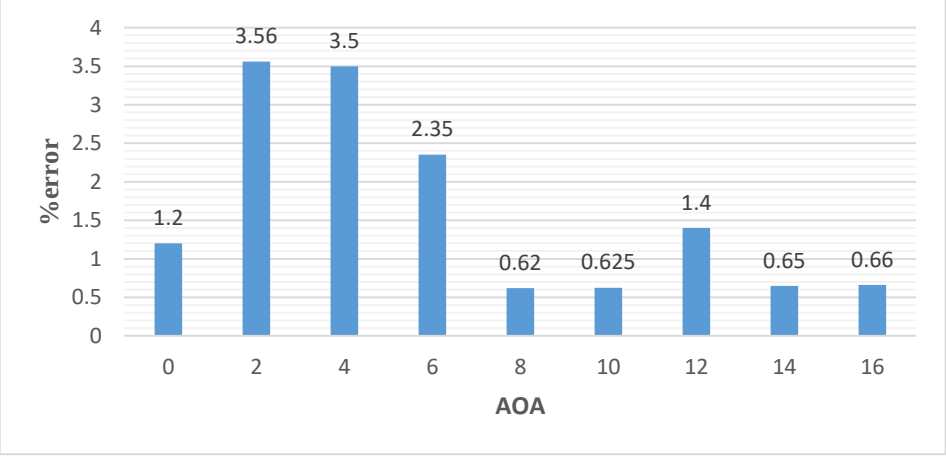

Figure (3.12) Error percentage curve for Cl validation results for HF1020

3.5.3 Pressure Coefficient Validation

Another parameter for validation is the Pressure coefficients Cp, it is calculated for the simulated foil HF1020 at angle of attack 6 and 10 and the output curves are compared with the other research[84], the two curves are shown in figure (3.13) and have a good agreement with other experimental research [84].

As it is shown in figure (3.13), the negative values of C_p (upper surface) indicate the suction side, while the positive C_p values (lower surface) indicate the pressure side of the hydrofoil. The agreement between the CFD results and benchmark experimental measurements is very good at transitional flow regime as shown in two angles of attacks indicated in figure (3.13).

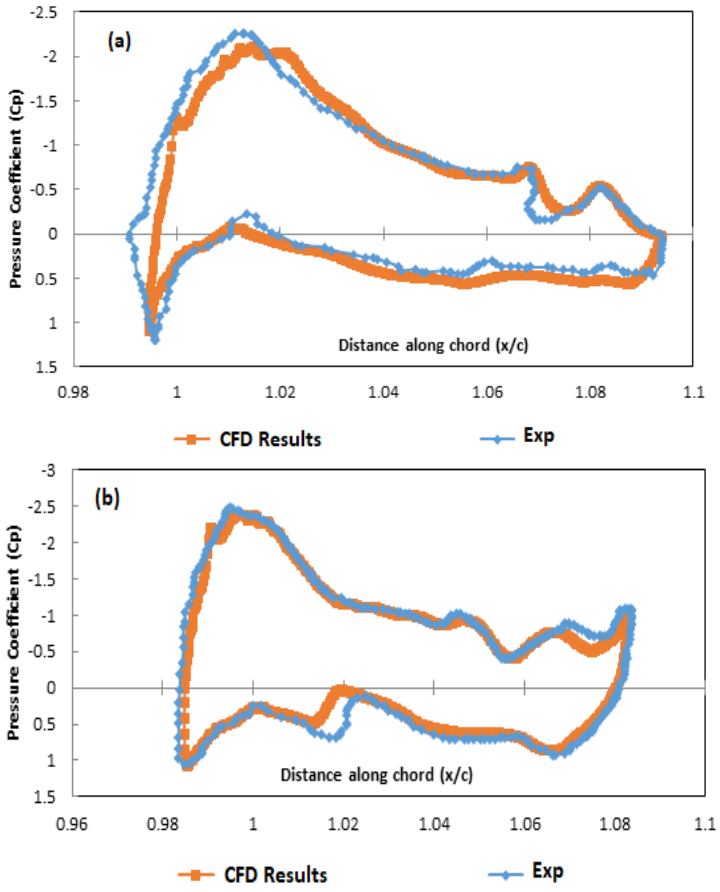

Figure (3.13) Validation of the pressure coefficient CFD simulations and experiments established in the benchmark case [84] for transitional flow regime (Re=190,000) at (a) 6º and (b) 10º Angle of Attack. X-axis represent the non-dimensional distance along chord represented by (x) coordinate divided by chord (c).

3.6 Calculations of Power based on Hydrodynamic Lift

Power is generated due to hydrodynamic lift. Hydrodynamic losses occur due to drag. Therefore, the generated power varies with the angle of attack. In order to demonstrate such variation by the 2D CFD model, the power is calculated as function of the lift coefficient and flow field variables as following:

$$P = \frac{1}{2} C_l \rho A v^3 \qquad (3.12)$$

where P is the power (W), C_l is the lift coefficient, ρ is the water density (Kg/m^3), $A = c \times L$ is the chord length (m) and v is the flow velocity (m/s). The swept area is calculated as using unity product of chord and unit length, 0.1 m [108, 109]. The variation of hydrodynamic power and losses with AoA are plotted in figure (3.14) and listed in details in table (3.4).

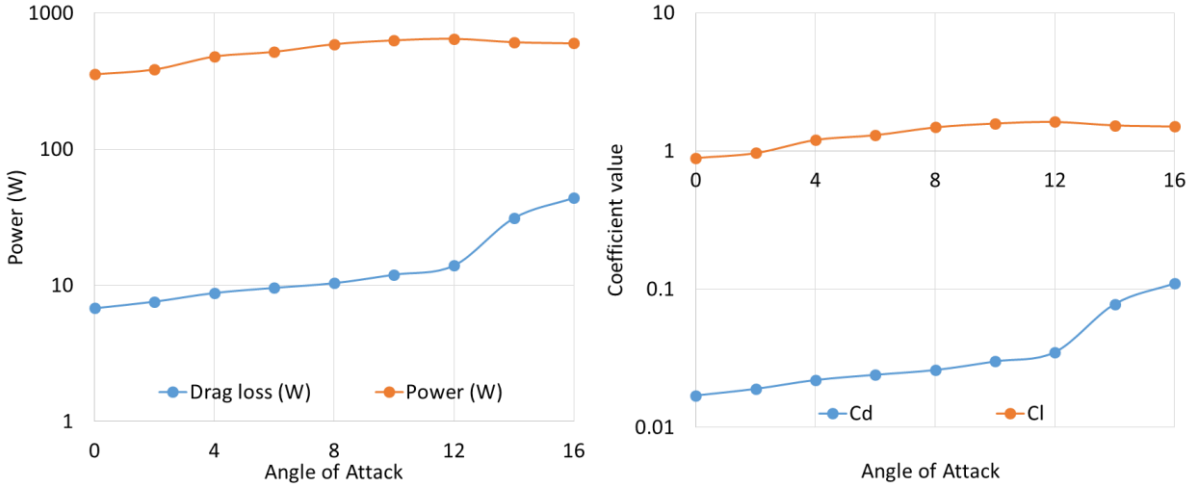

Figure (3.14) AoA Variation of (a) Hydrodynamic power and losses compared to (b) AoA variation of hydrodynamic performance parameters

3.7 Flow Structure: Pressure and Vorticity

3.7.1. Stall angle

To describe a stall angle, assume an HAMT with a constant rotation speed and fixed blade pitch angle. When flow velocity increases, the tip speed ratio decreases and the relative wind angle increases causing an increasing in the angle of attack. A turbine with this characteristic is possible to be controlled. When flow velocity increases to a certain value, the turbine becomes less efficient, at this angle of attack, it's known as a stall angle. When stall angle is accrued, it causes a loss of lift and torque. Consequently, some zones of the blades are in stall. [25]

3.7.2. Boundary layer separation:

Vortices are generated in the wake when current flows over an Aerofoil of a turbine blade. The vortices are generated by a mechanism which is called boundary layer separation.

Separation point is a point at which the flow fluids prevent flow back of the fluid, boundary layer separation must occur [110]. As the boundary layer separates from the surface a wake is formed in the downstream region. The point at which boundary layer separate occurs is dependent on a parameter called Reynolds number as shown in figure (3.15).[111]

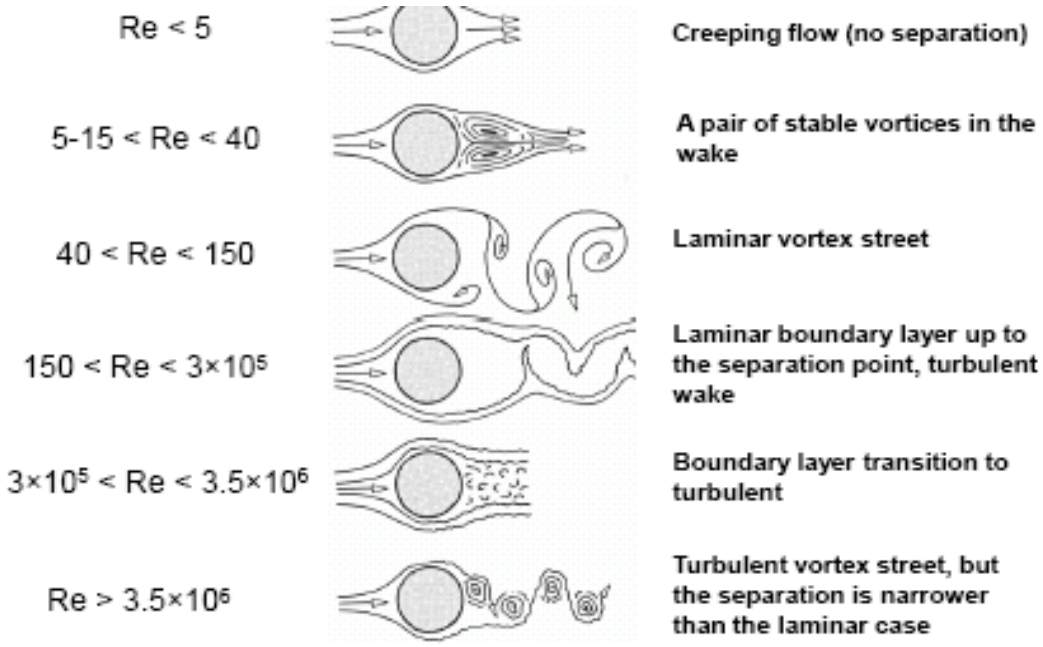

Figure (3.15) Vorticities at different Reynolds number[111]

3.7.3 Analysis of pressure and velocity distributions around the hydrofoil

In 2D CFD models, the variation of AoA is parametrized by running one simulation for each AoA. In reality, AoA varies due to the twist angle of the blade. Therefore, the most meaningful way of analyzing the flow structure in 2D CFD models is qualitative analysis using contour plots. It is primarily important to analyze the flow structure under transitional flow regime to demonstrate the relevance of the transitional SST $k-\omega$ model, as explained earlier in this chapter. The purpose of studying the flow structure through pressure and vorticity fields is to show the influence of AoA on the flow structure. This is essential to the main contribution of this research that is the concept of VSG.

Figures (3.16) and (3.17) show the distribution of pressure and vorticity at nine different AoA. The separation zone can be identified as the region with negative pressure on the upper surface of the hydrofoil. It is clear in figure (3.16) that such region varies considerably in size and magnitude according to the AoA. The variation is nonlinear as

the flow undergoes transition. This is further explained by figure (3.17) where the vorticity contours are shown. The vorticity contours show the regions where the flow undergoes rapid vortex generation downstream the hydrofoil.

It can be noticed that, pressure distribution in top and bottom domains (compared to chord) is asymmetric (i.e. non-symmetric) in all AoA values with a minimum difference at 0^o angle of attack. This explains the results presented in table (3.2) where the minimum value of lift coefficient is observed at such AoA. In this case, and if a unity blade length is considered, it is much harder to rotate such blade compared to other AoA values, where pressure distribution has larger differences between upper and lower surfaces. With larger AoA values, pressure distribution on the lower surface always has the larger values than the case of 0^o angle of attack. This further explains the increase in lift coefficient shown in table (3.2).

From vorticity contour shown in figure (3.17), it can be seen when the angle of attack is increased, regions with high vorticity values increase. Separation occurs further upstream the hydrofoil when the AoA is increased. At zero AoA, the flow is attached to the hydrofoil downstream to the trailing edge, when the AoA increases, as seen at 12^o and 16^o, the flow separation appears further upstream.

It is important to notice the complexity of the vortex structures associated with flow separation. This complexity causes modeling difficulty as indicated earlier in this chapter with fully-developed flow turbulence models. Also, it is important to notice the correlation between the size and magnitude of the separation region as it appears and increases proportional to the AoA and the increase of drag coefficient and losses shown in figure (3.14). Separation of boundary layer and appearance of this vortex structures causes drag to increase.

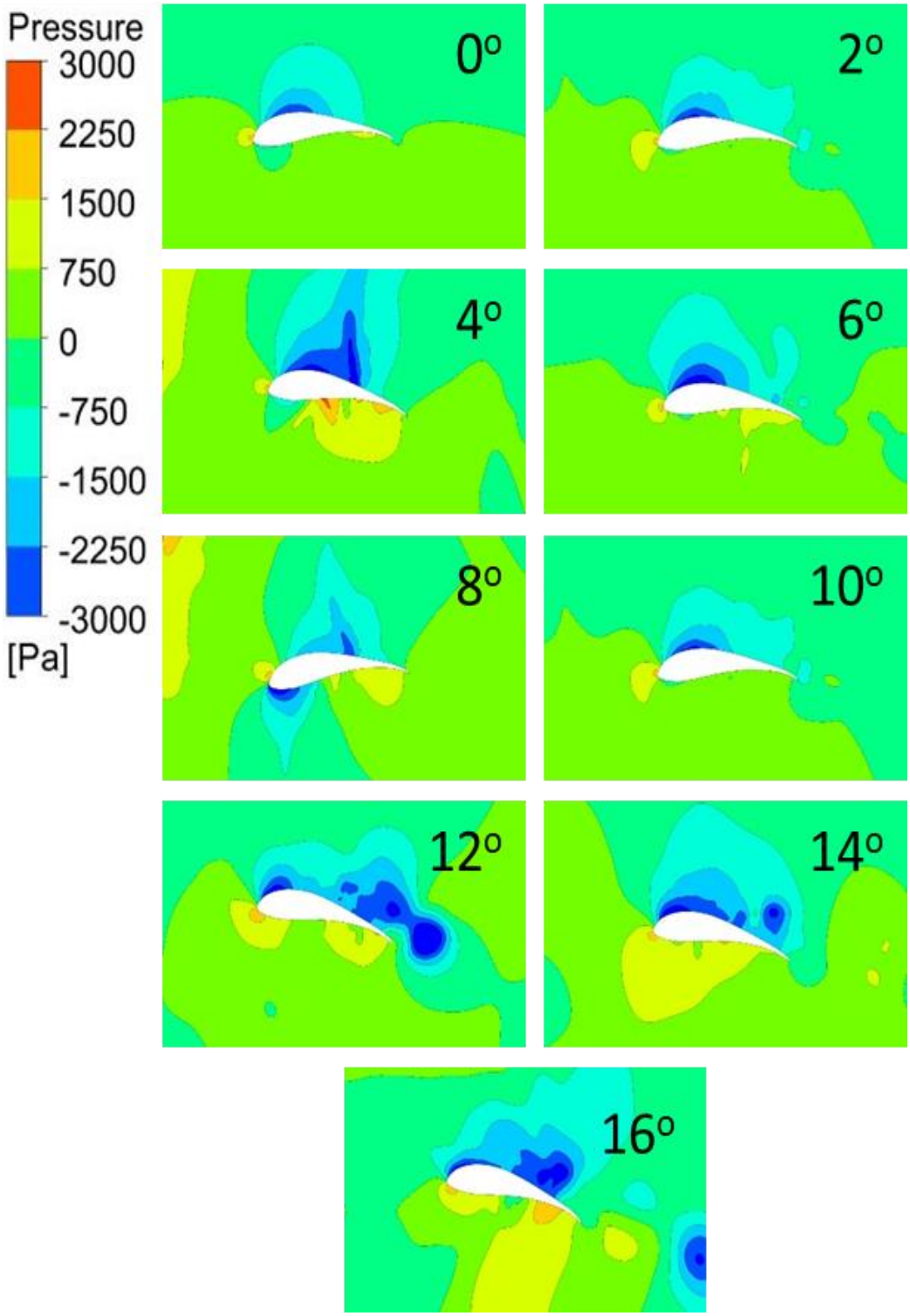

Figure (3.16) Pressure contours showing the variation of pressure distribution around the hydrofoil with respect to different AoA values (0º-16º).

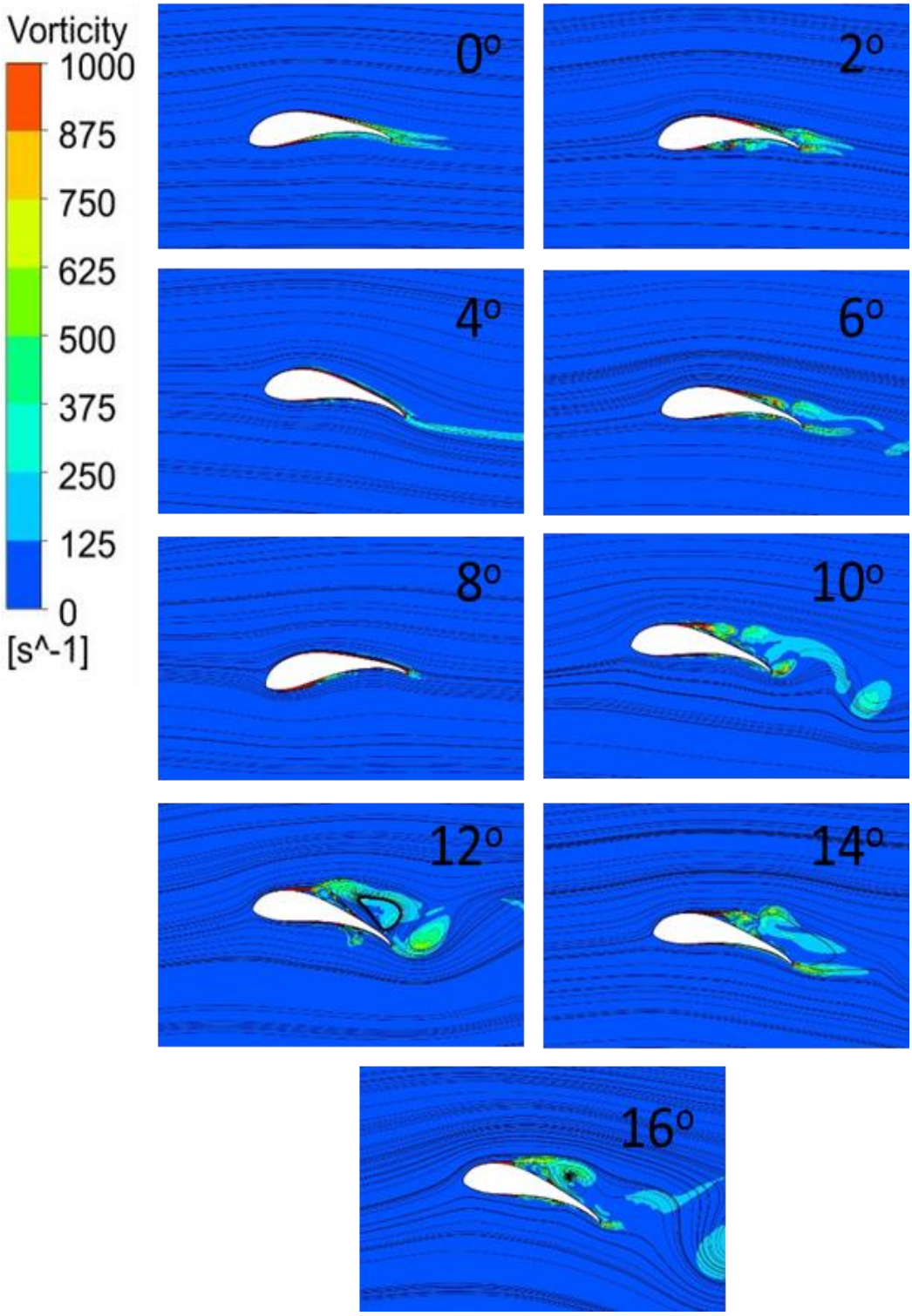

Figure (3.17) Vorticity contours showing the variation of separation region around the hydrofoil with respect to different AoA values (0º-16º).

3.8 Chapter summary

A 2D-CFD model representing transitional flow over a HAMCT hydrofoil section has been developed, verified and validated. The computational domain was discretized to 194,981 tetrahedral cells and the steady-state solver was used. Turbulence was modeled using the SST $k-\omega$ model that is specifically derived for transitional flow. Comparisons with five turbulence models showed that the SST $k-\omega$ model predicts with hydrodynamic parameters with modeling error range from -18.6% to 28%, depending on the angle of attack.

The 2D CFD model predicted average hydrodynamic performance ratio of 44.54±16.16 while the experimental benchmark dataset had an average ratio of 40.84±14.82. This modeling error was deemed quite acceptable given the transitional flow regime and the assumptions made in the steady 2D CFD model. The hydrodynamic power and drag losses were both found to be directly proportional to the angle of attack.

For the local distribution of pressure coefficient on the hydrofoil, the 2D CFD model predicted a pressure profile that is generally similar to the experimental measurements. Minor spatial differences exist due to the meshing and modeling assumptions.

The overall performance of the 2D CFD model in simulating transitional flow over the hydrofoils analyzed in this chapter is representative of the problem. The model was found capable of predicting physically realistic values of the hydrodynamic performance parameters and local pressure on the hydrofoil.

Based on the results of analyzing the flow field around the hydrofoil of turbine, the performance of HF1020 foil can be affected by the angle of attack. This is clearly shown by the drag and lift coefficients in fig (3.9) and fig (3.10), where C_d and C_l coefficients increase with increasing the angle of attack for a certain limit value. Hence, from C_l/C_d curve fig (3.11), the blades performance reaches the peak at around 6^o angle of attack.

At zero angle of attack, there is a relatively small lift force generated, and if it is desired to increase the lift force and the value of lift coefficient, the angle of attack has to be increased. By doing that obviously the amount of drag force and value of lift coefficient also increased, but the increment in drag coefficient is slightly lower than lift force.

The analysis of the flow structure around the hydrofoil, at varying AoA values, showed the complexity of the transitional flow regime. Non-symmetric low-pressure regions and vortex structures have characterized the near flow around the hydrofoil. The trend of hydrodynamic performance parameters was found to be associated with the flow structure. The increase of AoA generates large vortex structures attached to the upper surface and trailing edge of the hydrofoil. This increases the drag. While the low pressure region, associated with higher AoA values increase the lift.

CHAPTER 4

Three-Dimensional CFD Modelling of Full-Scale HAMCT Hydrodynamics

4.1. Introduction

After establishing the 2D CFD model of the HAMCT hydrodynamics, the modeling strategy and approach are extended to develop a full-scale 3D CFD model of HAMCT. The 3D model represents a three-blade turbine similar to the design experimentally investigated by Goundar et al [84, 112]. The 3D CFD model was established based on the outcome of the 2D CFD model. The near-wall mesh refinement, streamwise meshing density and solver setup were all adopted from the 2D CFD model. The purpose of the 3D CFD model is to establish the final modeling approach that is used to conceptualize and validate the VSG device.

4.2 Turbine design

When designing HAMCT hydrofoils, important hydrodynamic characteristics must be studied such as, the pressure distribution on the hydrofoil's surface, the minimum coefficient of pressure(C_p), coefficient of lift(C_l), coefficient of drag(C_d), and hydrodynamic performance ratio (C_l/C_d) [84]. The turbine hydrofoil considered in this work is NACA HF1020 with an average chord of 21 cm along the entire blade and a maximum thickness of 3.36 cm. The turbine will run at a fixed TSR. The main reason for choosing a NACA foil is that complete performance data is available, and an experimental research is done by other researcher to be compared with the results.

The number of blades is a vital choice when designing a turbine. Too few blades will result in an uneven pulsating torque since the blades only produce torque during certain parts of a revolution on a turbine, the number of blades was simply chosen to be three. At a later stage it might be interesting to change the number of blades to compare how it affects the performance [84]. The model was 3D represented on Rhino software, as shown in figure (4.1), with blade data from (Xfoil) program to get desired dimensions, then import to ANSYS (fluent) to perform the study on the turbine, 3 bladed turbines, in cylindrical domain is used in 3-D simulation, with 3m total blade radius.

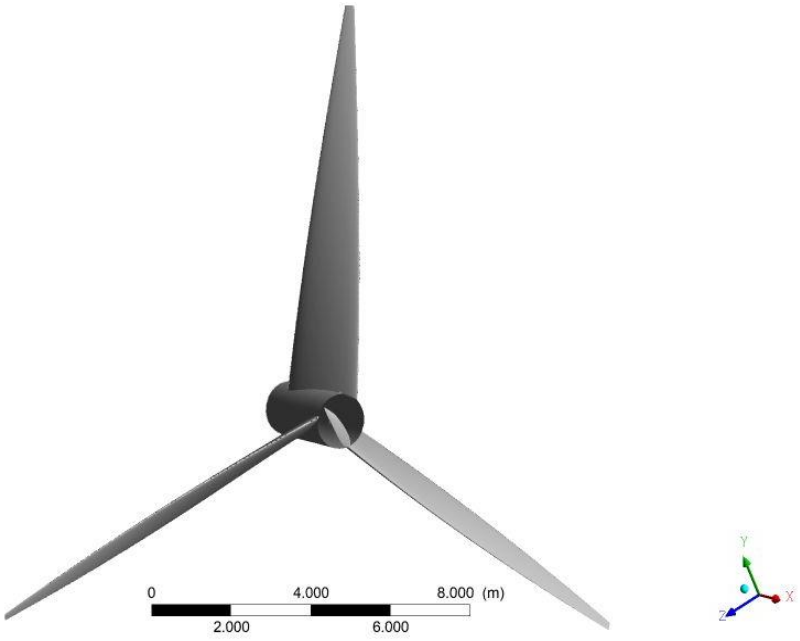

Figure (4.1) 3-bladed turbine model HF1020

4.3 3D CFD Model Development

The computational domain in this simulation is chosen similar to the bench mark study and is sized to allow for full development of the upstream flow and to minimize blockage effects. The computation domain is a cylinder with a radius of 5m and a stream wise length of 15m. Figure (4.2) shows the computational domain and mesh topology. The inlet of the computation domain is a steady axial velocity of 2 m/s.

The 3D computational domain is developed with a Hex-cells meshing, as shown in figure (4.2). The mesh is generated with $3.4x10^6$ computational grid cells. The number of meshing is decided based on the 2D CFD as the product of the 2D CFD mesh count and the length of the 3D CFD domain. The mesh quality statistics is very good average skewness ratio is 0.2416, and maximum of skewness ratio is 0.983. The histogram of mesh quality metrics is shown in figure (4.3). Fine mesh and small element with inflation at location are close to the turbine. Element size grows along two axes from NACA shape to boundaries. For optimal results, the properties of elements are very important, and number of element of best quality mesh is less than bad mesh. To confirm quality of good or bad grid [85], parameters to be evaluated are a) Skewness

Ratio, acceptable value is less than 0.6, ideal is 0, b) Aspect Ratios, acceptable value is less than 1.5, ideal is 1, c) the Jacobian Ratio is 1 and d) Warpage are 0 deg. If parameters of mesh are close to these criteria, result can be accepted [101].

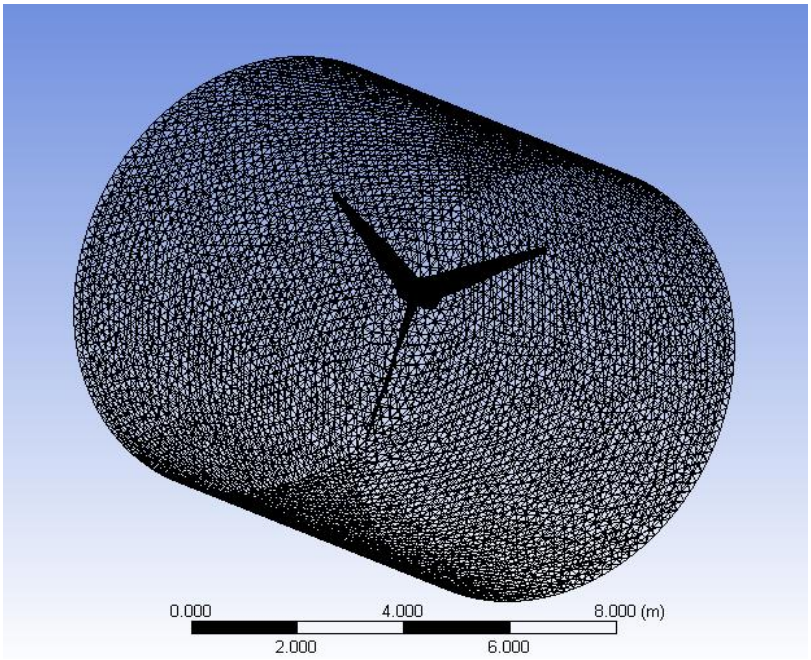

Figure (4.2), Model Mesh using hexa element as implemented in ICEM software for the mesh generation

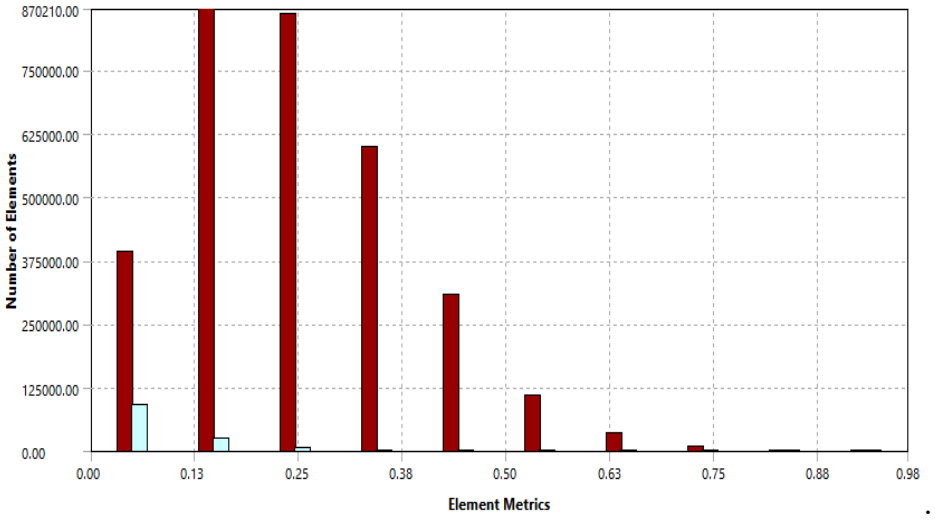

Figure (4.3), Statistics of elements based on meshing criteria (Histogram)

4.4 Physical Properties and Solver Settings

The 3D CFD model employs a third order-accurate MUSCL discretization scheme. Although, to model the turbulence terms of the governing equations, the shear stress transport SST k omega turbulence model is selected. To model the transport of turbulent shear stress, the SST k omega turbulence model can be used, because it gives accurate predictions on the onset and amount of flow separation under adverse pressure gradients and has been effectively used in the CFD simulation of water. While the outer domain remains in a dynamic state [100].

A uniform turbulence intensity of 2.8% is set and modeled at the inlet [114]. A pressure outlet boundary is applied at the outlet of the domain. And the intensity of turbulence is ignored, to improve the stability of the numerical simulations, symmetry boundary conditions were used at the side wall of the cylinder. To avoid the wall defects, the symmetry boundary is used and consider the wall as part of longer domain and symmetry (i.e. slip) boundary to eliminate the wall effect and impose the far-field stream condition [113]. It is usually noticed that turbulence intensity plays an important role on the act of a water current turbine. The performance fluctuations dramatically increase with the turbulence intensity. The wake dissipates much faster as the turbulence intensity increases, this work focuses on the velocity on normal axis plus the swirl effect of turbine positions [100]. The boundary and initial conditions of the 3D CFD model are shown in figure (4.1).

Table (4.1) Details of the boundary and initial conditions of the 3D CFD model. Number of blades is 3, turbine diameter $D = 10\ m$

Boundary / Initial condition	Settings	Value (unit)
Inlet velocity	Constant velocity	2 m/s
Inlet turbulence intensity	Percentage and hydraulic diameter	2.48%, D
Outlet pressure	Constant pressure	0.9 MPa
Water density	Constant density (incompressible flow)	998 Kg/m^3
Water viscosity	Constant viscosity	0.00103 Pa.s
Meshing	tetrahedral	3.4 million cells
Convergence criteria	Residuals	10^{-5}
Spatial discretization	3rd order (MUSCL)	--
Time discretization	None, steady	--
Turbulence model	SST $k-\omega$	--

4.5 3D Model Validation and Results

4.5.1 Model Validation

In order to validate the 3D CFD model, 16 3D simulations were conducted to calculate the power-coefficient against varying tip speed ratio (TSR). TSR is a characteristic parameter for HAMCT operation expressed as: $TSR = \omega \times r/V$ and it represents the ratio between the turbine blade-tip and current velocities [85, 114]. At low current velocities, such as the conditions adopted in this work to represent south Mediterranean currents, turbines cannot work at high TSR, therefore, their power coefficient is relatively low compared to conditions where high current velocity exist. However, for the sake of validating the 3D CFD model, different TSR values are adopted to setup different simulations to demonstrate the model validity. In The power coefficient can be calculated from the CFD results as following:

$$C_{Pw} = \tau\omega / \left(\frac{1}{2}\rho A V^3\right) \quad (4.1)$$

The available data from the benchmark case [112] reports only power coefficient vs TSR. There is no other data available in published literature that matches the operating conditions of the HAMCT in this thesis. Each simulation of the following validation set is conducted with 3.4×10^6 grid cells, second-order scheme and steady flow setting. The solution is considered converged when all residuals are less than 10^{-5} in absolute value. All validation was conducted at current speed of 2 m/s and Reynolds number of 1.9×10^5.

CFD results have over-predicted the power-coefficient for 1.5<TSR<4 and under-predicted the power-coefficient at higher TSR. This change in trend is justified by the strong tip-vortex separation in high TSR values which is mostly not captured in CFD models, as previously reported [76, 115]. The average positive and negative errors are 7.8% and -7%, respectively. This validation exercise shows that the 3D CFD modeling framework is reliable and produce physically acceptable results. In order to extend the validation exercise, another comparison was conducted between the 3D and 2D models. This comparison aims to show the third-dimensional effect on predicting the hydrodynamic performance

parameters. It is very important to combine both validation exercises in order to demonstrate the reliability of the modeling approach.

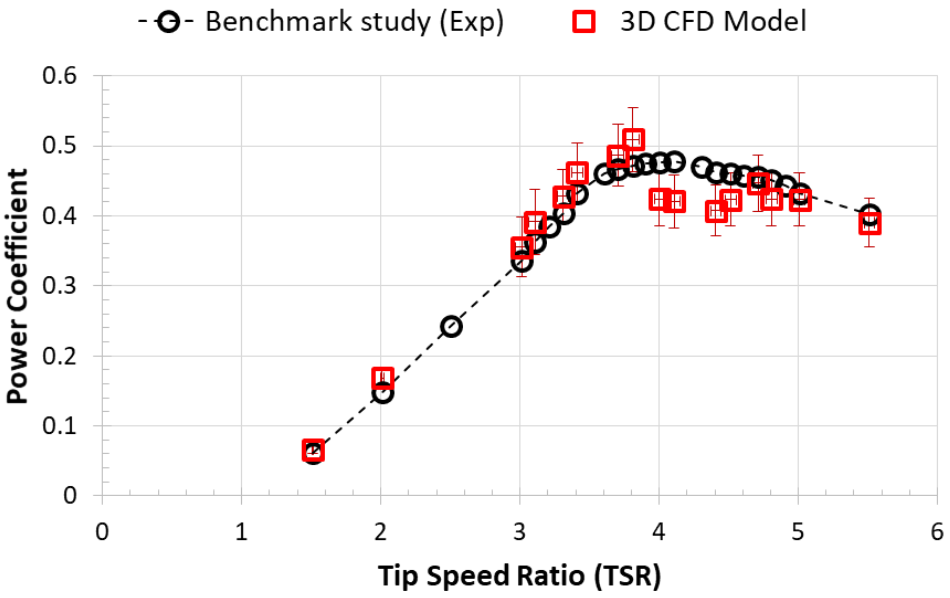

(a)

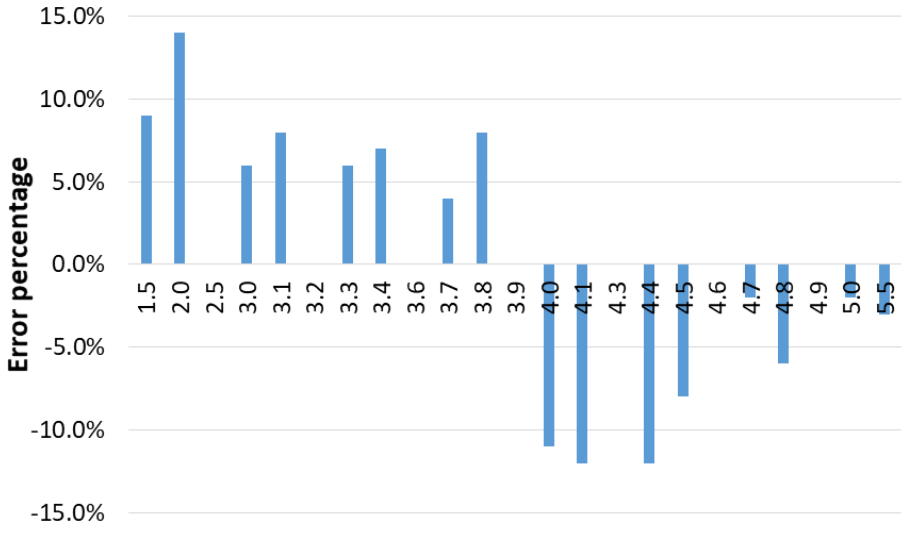

(b)

Figure (4.4) Validation of the 3D CFD model with experimental data from benchmark case in (a) and error percentage in (b). Error bars in (a) represent numerical uncertainty due to meshing and solution convergence. Sign in (b) represent under vs over prediction of power coefficient. Each point represents a complete CFD simulation.

Figure (4.5) shows the results of the 2D and 3D CFD models in comparison with the 2D experimental measurements established by Goundar et al [107] which is the validation reference for the present study. As shown in figure (3.12), the 2D model represents the experimental measurements with maximum error of 3.56%. However, in figure (4.5), the difference between 3D CFD model and both 2D sets is quite substantial (average 65%). This difference is not resulting from error, and it can be physically justified. The justification for this difference is due to the aspect ratio ($AR = l/c$) where l and c are the blade span and chord length, respectively. Based on the dynamic similarity theory, 2D aerodynamics defines the aspect ratio of a 2D hydrofoil model as infinite ($L = \infty$), since the blade span is assumed infinite too[108, 116]. Hence, the lift coefficient has maximum values. However, in the 3D turbine model where the span has a finite length, the values of C_l are significantly lower. Colonies et al [116] and Robin et al [117] showed that such difference is within 60% in non-twisted blades. In the present work, as shown in figure (4.6), the average difference is 65% with the 3D twisted-blade turbine CFD model, as shown in figure (4.6). Therefore, the 3D model in the present work is validated.

In addition, the value of C_l predicted by the 3D model is hardly varying with the AoA, as shown in figure (4.5), contrary to the values predicted by the 2D model and experiments. This insensitivity to AoA variation is due to the twist profile of the blade. In the present turbine model, the twist profile dictates a change in the twist angle at 2.46^{o} per unit blade length. This twist profile is similar to the twist profile investigated by Sayers et al [118] and Cotton et al [119]. They established the fact that due to the twist profile of the blade, the values of C_l are almost constant with respect to the change in AoA, which is evident in figure (4.5).

The reduction in C_l in the 3D model is also explained by the Betz limit which is the theoretical maximum efficiency for a wind turbine, conjectured by German physicist Albert Betz in 1919[120]. Betz showed that this value is 59.3%, meaning that at most only 59.3% of the kinetic energy from current flow can be used to spin the turbine. Given the relation between power and lift coefficient(C_l), this means that the value of such parameter in 3D should be 59.3% less, at least from the theoretical value in 2D. In 2D flow, the generated

power is theoretical assuming infinite blade length. In the results presented in figure (4.6), the reduction of the 3D blade C_l is well below the Betz limit.

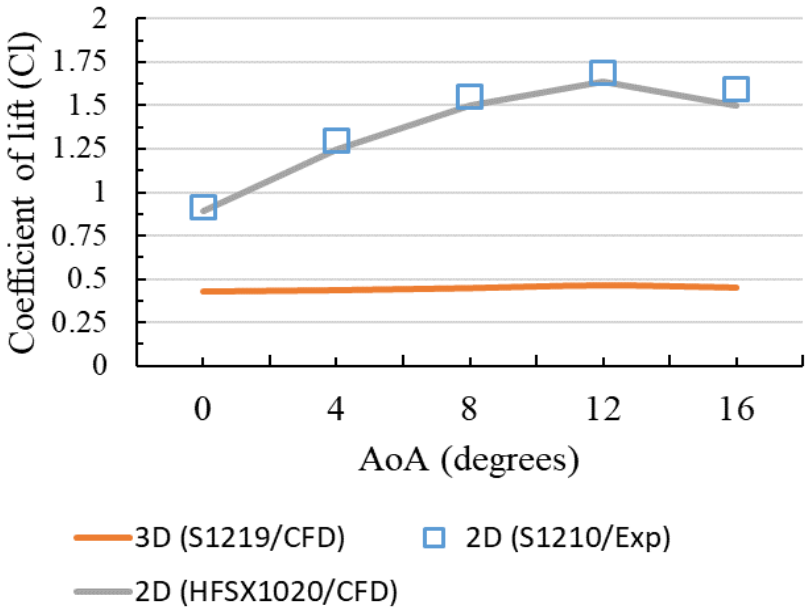

Figure(4.5) Comparison between 2D and 3D C_l using CFD and experimental measurements [107]

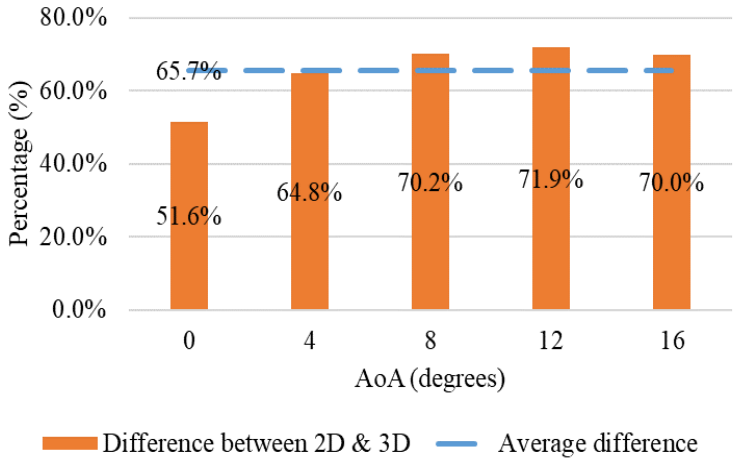

Figure (4.6) Difference in C_l due to AR between 2D and 3D CFD models as function of the AoA.

4.5.2 Pressure and force contours on the blades

Many features and parameters can be obtained in fluent ANSYS that can help in performance evaluation and indicate many variables such as pressure, velocity, forces, turbulence on the HAMCT and its blades, for example figure (4.7) shows the pressure contour for the HF1020 foil turbine blades.

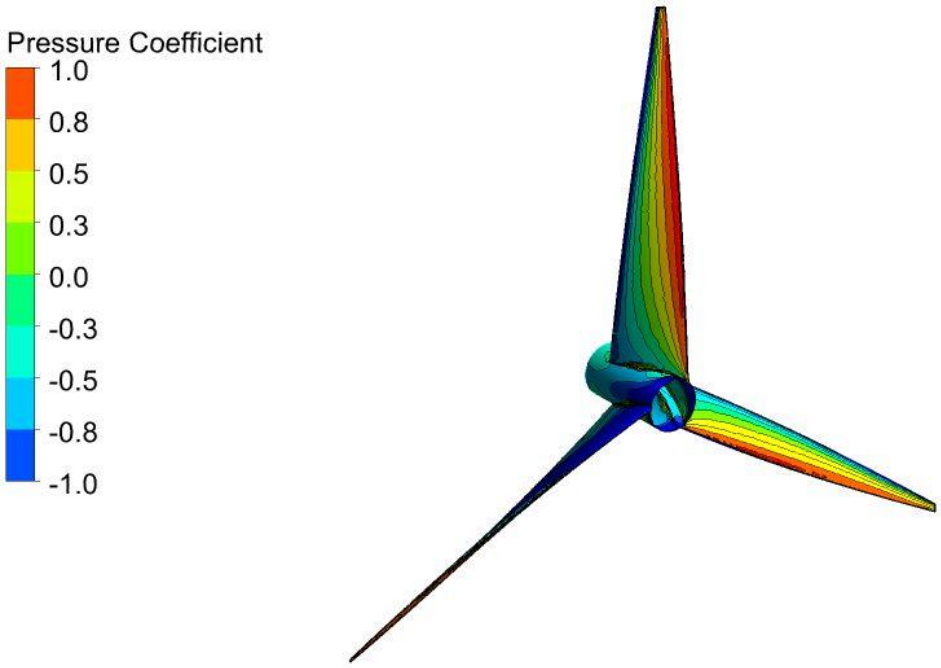

Figure (4.7) pressure contour for the HF1020 foil turbine

From figure (4.7), it is clear that the maximum pressure coefficient will happen on the leading edge of the turbine blades. The distribution of pressure on the turbine blade matches the results of the 2D simulation qualitatively and demonstrates similar trend. Another parameter can be monitored on the turbine which is the forces vectors on the MCT. Forces distribution in figure (4.8) shows that the maximum values for forces on the blades will happen on the hub and the edges of the turbine blades which leads to high stresses and loads on the edges of the turbine blades.

Turbine blade is subjected to many forces, the resultants of the forces are mainly resolved into two forces and one moment. The component of net force acting normal to the incoming flow stream is known as lift force and the component of the net force acting parallel to the incoming flow stream is known as the drag force [121], as observed in figure (3.2). The contours of the net force on the turbine blades are shown in Figure (4.8). It can be seen that the regions where maximum force is exerted on the turbine blades are near the blade center in streamwise direction.

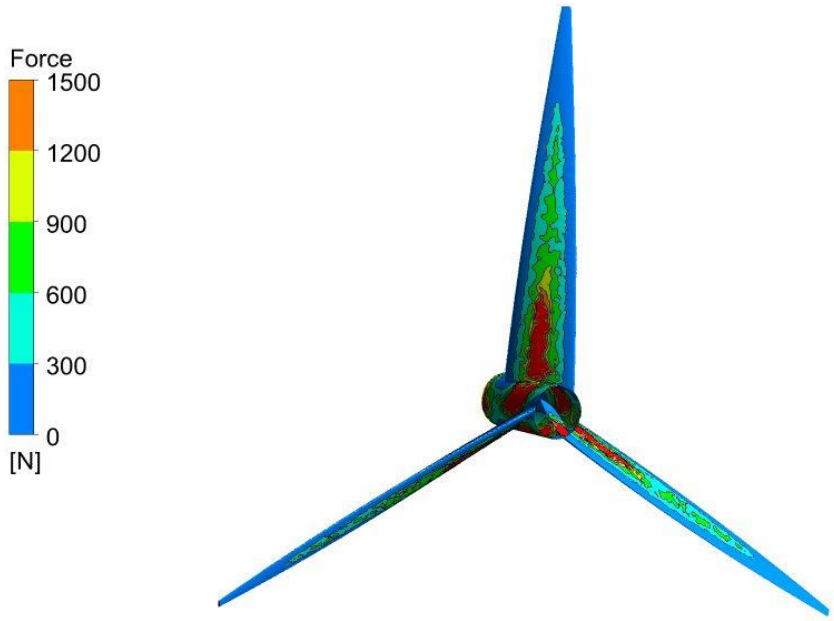

Figure (4.8) Net force field acting on MCT blades

4.5.3 Velocity, turbulence and separation characteristics of HAMCT

The velocity contours around the 3D model is shown in figure (4.9) where the contour plane is located at the middle plane of the turbine. The distribution of velocity signifies the rotation direction of the turbine and shows the acceleration due to separation at the turbine blade. Figure (4.10) shows the contours of turbulence kinetic energy production (production of K) at the mid-plane of the turbine. Figure (4.11) shows the separation bubble denoted by iso-surface of the second velocity invariant (Q-criterion). It is clear that there is some sort of symmetry between the blades, however, the transitional flow dictates spatial variation between the flow characteristics of the three blades.

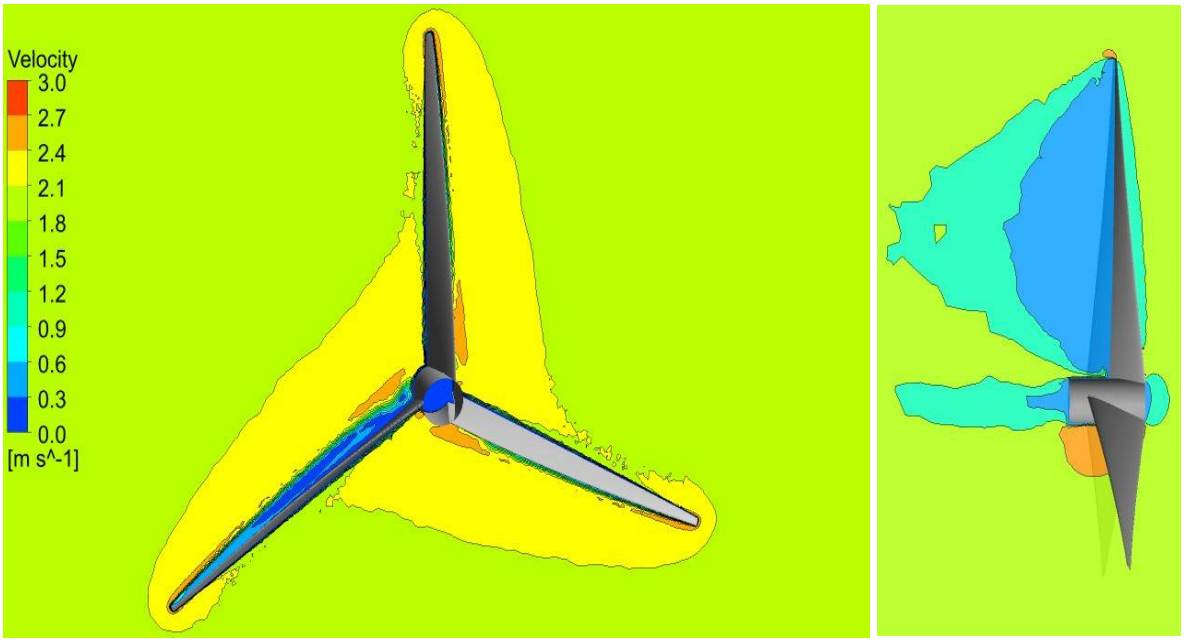

Figure (4.9) Contours of velocity magnitude around the 3D HAMCT model at Reynolds=1.9x10^5.

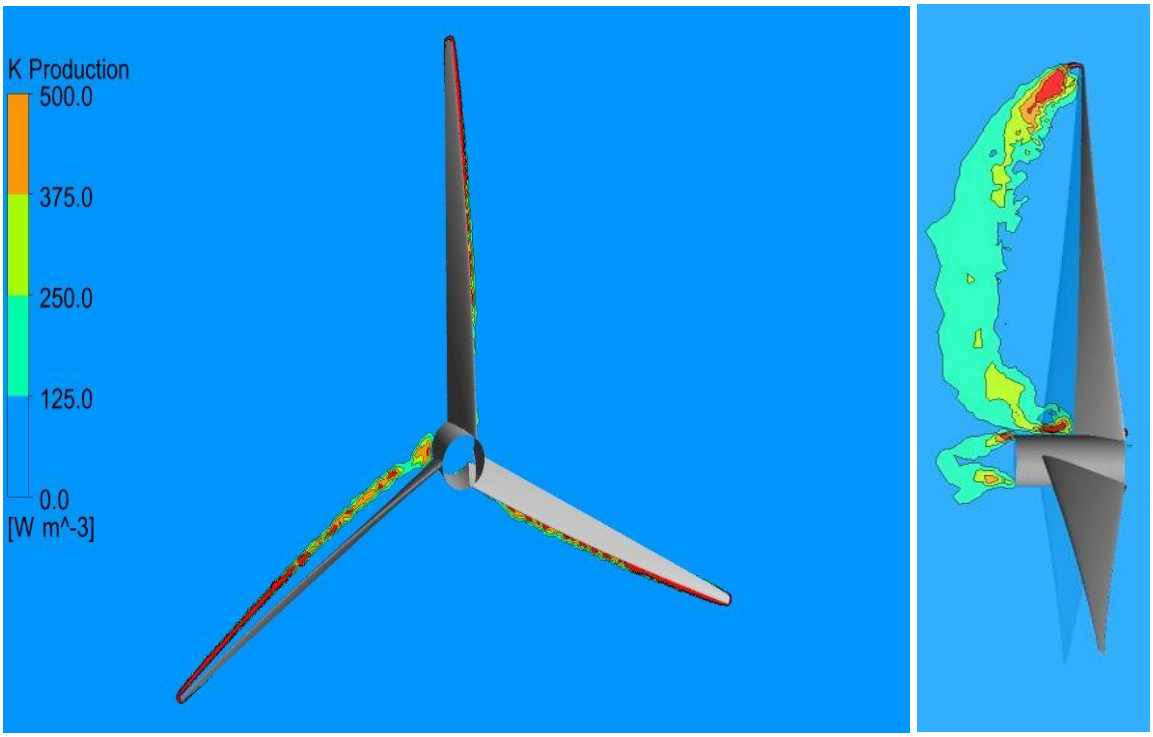

Figure (4.10) Production of turbulence kinetic energy

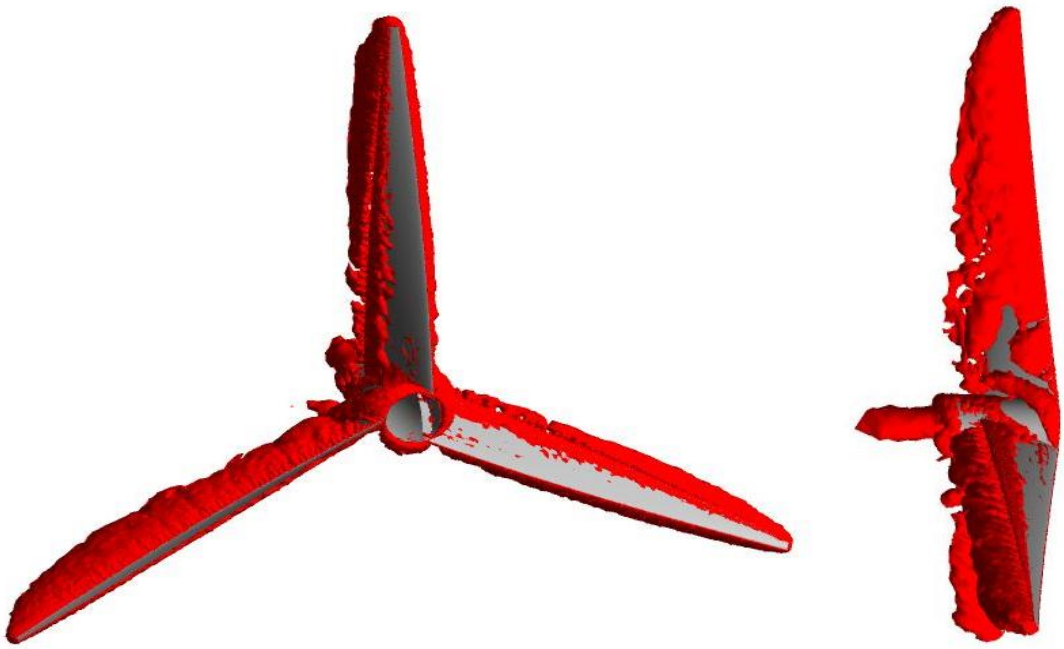

Figure (4.11) Iso-surface of constant Q-criterion at threshold value of 0.01 s^{-1}

4.6 Discussion and Conclusion

A 3D full scale CFD model of HAMCT was developed, validated and discussed. The model was developed based on the parameters and approaches used in the 2D model. The model was validated by a parametric comparison with measured power coefficient (C_p) derived from the benchmark study. The validation comparison revealed that the average positive and negative modeling errors are 7.8% and -7%, respectively.

The validation of the 3D CFD model was demonstrated by comparing the 2D and 3D lift coefficient with respect to previous reports and the Betz limit theory. It was found that the difference between 2D and 3D C_l values in very good agreement with both previous works and with the Betz limit theory. Pressure coefficient and force fields on the turbine blades are analyzed and shown to be consistent with the theory of operation. The flow structure around the turbine was outlined. It is shown that the flow around the turbine is characterized by attached separation region and downstream turbulence production zone. The 3D CFD model predicts hydrodynamic performance of HAMCT turbine and is concluded to be suitable for studying performance improvements brought by the VSG device.

CHAPTER 5

Hydrodynamic Performance Characteristics of Novel Swirl Generator for Improving HAMCT

5.1. Introduction

Swirl flows can be seen in natural flows, for instance, tornadoes and typhoons, and have been broadly used in engineering applications [122]. For example, aeronautics, heat exchange, spray drying, separation, combustion, etc. For decades, their significance and complexity have been the focus of many research investigations. A complete review of the complex nature of the research into the swirl and vortex breakdown can be found in [122]. In aeronautic applications, amplified lift and stability of the wing is caused when leading-edge vortices shed from a delta wing induce a velocity field. Yet, these vortices can under particular conditions be linked to the angle of attack of the wing [122].

A swirl flow can be defined as one undergoing concurrent axial and vortex motions. It is caused through the application of a spiraling motion, a swirl velocity component (tangential velocity component) being imparted to the flow by either using swirl vanes,

entry swirl generators or through direct tangential entry into the chamber [123]. The curl or merely the distortion of the velocity field of such flows is known as the vorticity. Different angular velocities of different rings of particles causes this distortion when it exists. Hence, causing an object that is travelling on a circular path to revolve about its own axis as it goes along. The vorticity at one point can be defined as the ratio of the circulation round an infinitesimal circuit to the area of that circuit [124] in the case of a two-dimensional plane flow and is given by:

$$\text{Vorticity } \Omega = \frac{circulation}{area} = \frac{\partial v}{\partial x} - \frac{\partial u}{\partial y} \qquad (5.1)$$

Potential or free vortices are called at flows which have a tangential or swirl velocity w of type w = C/r, where w is the swirl velocity component, C is circulation and r is the radius. If every element of the moving fluid undergoes no net rotation (with respect to chosen coordinate axes) from one instant to another, therefore the vorticity of such flows tends to be zero and the local flow rotates as a static body. As a result, these flows are known as irrational. Forced vortices are the flows with solid-body rotation, for that the swirl velocity is given up w = C/r. The vorticity does not tend to be zero and such flows are known as rotational in this situation only

if every element of the moving fluid moves along a circular path and concurrently rotates about its own axis [122, 123]

There might be rotational motion in a single part of a flow field and irrotational motion in alternative part in practice. Moreover, all free vortices in real fluids have a central vortex core where the vorticity is non-zero. The creation of a free vortex flow can be caused by the conservation of angular momentum, where the circumferential velocity is sharply amplified as the radius decreases and ω finally decaying to zero at r = 0 since viscous forces begin to take over [123].

Differentiating between the free and forced vortices can be done through the radial position of the maximum value of the tangential velocity component: the maximum is found near the axis of symmetry in a free vortex; however, the maximum is found at the outer edge of the vortex in the forced vortex. The existence of a combined or Rankine vortex can be found in some situations where the forced vortex equation is satisfied at small radial distances and the free vortex equation for large radial distances as shown in figure (5.1) [125]. This type of vortex has been shown to develop, for instance, when introducing the flow tangentially at the periphery of a cylindrical chamber and exhausted at an axial nozzle [123, 124, 126-128]. Flow field and turbulence features have been exhibited by the central forced vortex region that seem to be considerably divergent from those seen in the surrounding non rotational vortex flow field. The inner or vortex core is usually referred to this central region. It is described as being free of shear but not free of vorticity. The core is commonly restricted to that region of the solid-body rotating flow but can also be stretched out to the radius of maximum tangential velocity. Table (5.1) [129] summarizes the characteristics of every type of vortex that can be distinctively defined [123, 130].

As well as classifying a swirl flow based on its type of vortex, it is possible to characterize the degree or intensity of the swirl through the usage of dimensionless local swirl number, as the degree of swirl has large-scale impacts on the flow fields [123] . For instance, the introduction of swirl into turbulent jets results in an increase in jet growth, rate of entrainment and rate of decay of the jet. The swirl number is defined as follows [131]:

$$S = \frac{G_\phi}{G_x r} \tag{5.2}$$

Where $r = R$; G_ϕ is the axial flux of angular moment and is given by

$$G_\phi = \int_0^R (\omega r)\rho u \, 2\pi r dr = \frac{2}{3}\pi R^3 \, \overline{uw} \tag{5.3}$$

G_x is the axial flux of linear moment and is given by

$$G_x = \int_0^R u \, \rho u \, 2\pi r dr + \int_0^R \rho \, 2\pi r dr = \pi \rho R^2 \bar{u}^2 \tag{5.4}$$

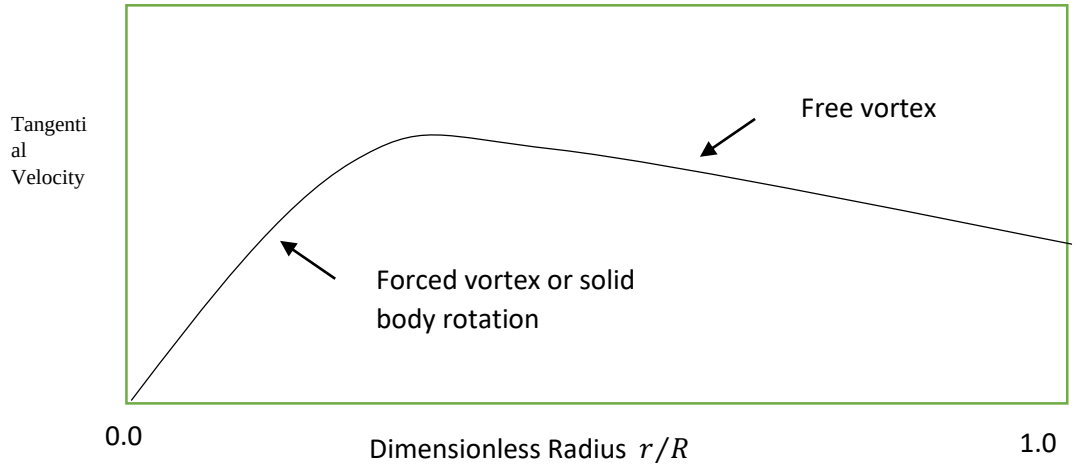

Figure (5.1) Qualitative representation of a Rankine vortex adopted based on [132, 133]

Table (5.1) Exact equations for calculating swirl flow velocity components

	Forced Vortex	**Free Vortex**	**Rankine Vortex**
Tangential velocity distribution w	$wr^n = constant$ Where $n < 0$	$wr^n = constant$ Where $n > 0$	$w = \frac{C'}{r}[1 - exp\left(-\frac{r^2}{R^2}\right)$
Angular velocity ω	C (constant)	$\frac{c}{r^2}$ $(fn\ of\ r)$	$fn\ of\ r$
Circulation Γ	$2\pi\omega r^2$	$2\pi C$	$2\pi C'[1 - exp\left(-\frac{r^2}{R^2}\right)$
Vorticity Ω	$4\omega = constant$	0	$\frac{4\pi C'}{R^2}[1 - exp\left(-\frac{r^2}{R^2}\right)$

The pressure term can be omitted that is assuming the static pressure is constant over the R [110]. The swirl number is typically used to define the level of swirl, as very weak swirl when

S_n < 0.2, a weak swirl corresponds to 0.2 < S < 0.5 and a strong swirl is when S > 0.5. A normalized swirl number (relative to the maximum swirl generated) can also be used to represent the data and is particularly useful as it can clearly show the level of the swirl and how it decays relative to the original level. This can be viewed by plotting the decay downstream of the TST against full recovery or as a downstream distance is normalized to the maximum distance for a recovery to 90% of the upstream velocity [123].

Representation of the data can be done through a normalized swirl number (relative to the maximum swirl generated) and is particularly beneficial since it can show evidently how it decays relative to the original level. This can be seen either through the plotting of the decay downstream of the TST against full recovery or as a downstream distance normalized to the maximum distance for a recovery to 90% of the upstream velocity [122].

5.2 Vane swirl generator (VSG) concept

This research aims at introducing a novel swirler concept to improve the performance of MCT. The novel swirler is basically a static structure which has swirl-generation vanes, installed upstream of MCT. The concept is sketched in the figure below. Study will be done on the swirl flow to compare the MCT performance with the flow without swirl effect, to contribute if it is better to use a swirler before the inlet flow of the MCT and its effect on the MCT performance. The hypothesis of this MCT-add on is to improve the swirl velocity field in the vicinity of the turbine, hence improve its hydrodynamic performance and efficiency. In addition, the presence of highly-streamlined velocity field will reduce separation layer and reduce stall.

In order to examine this research hypothesis, the validated 3D CFD model, which was presented here, will be used to conduct parametric study on the swirl number effects on blade hydrodynamic performance. The parametric study will consider ideal design characteristics from the hydrodynamic theory and propose evidence to examine the validity of the proposed hypothesis. As seen in the illustration shown in figure (5.2), the flow is coming in horizontal component Vx, the VSG will produce 3-dimensional velocities components (Vx, Vy and Vz), which will act as a swirl flow.

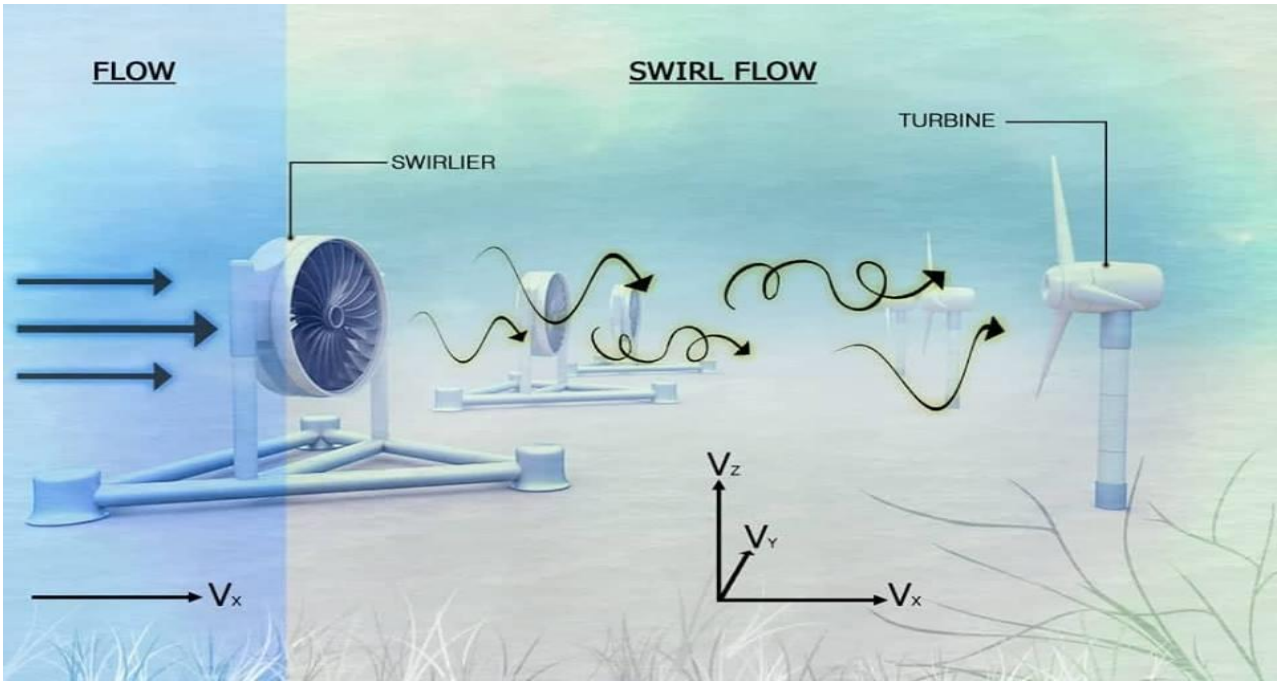

Figure (5.2), Swirler device before the inlet of MCT

5.3 Validation of the CFD solver with swirl flow

In order to demonstrate the solver validity with swirl flow, the exact equations describing the radial distribution of tangential velocity (table 5.1) was used to validate the CFD results. The use of exact equations in validating swirl flow is standard in CFD literature [132, 134-136].

In this validation exercise, only swirl flow is simulated and compared with the exact equations derived from the conservation of momentum, as shown in table (5.1). The exact equations provide reference for the velocity components as axial momentum is converted to tangential momentum downstream the flow. Figure (5.3) shows comparison between the CFD results and the forced vortex regime, as calculated using the exact equation, at two representative lines for$S_n = 0.1, 0.5$. The exact equation is devised from the Navier-Stokes equation of one-dimensional Rankine vortex (forced regime), while the CFD simulation here solves the Reynolds-averaged Navier-Stokes equation for three dimensional forced vortexes. That is why there are differences between the CFD vortex and exact vortex equation, as shown in figure (5.3). These differences are quantitative and do not affect the main flow field features which makes the CFD model valid for predicting swirl flow.

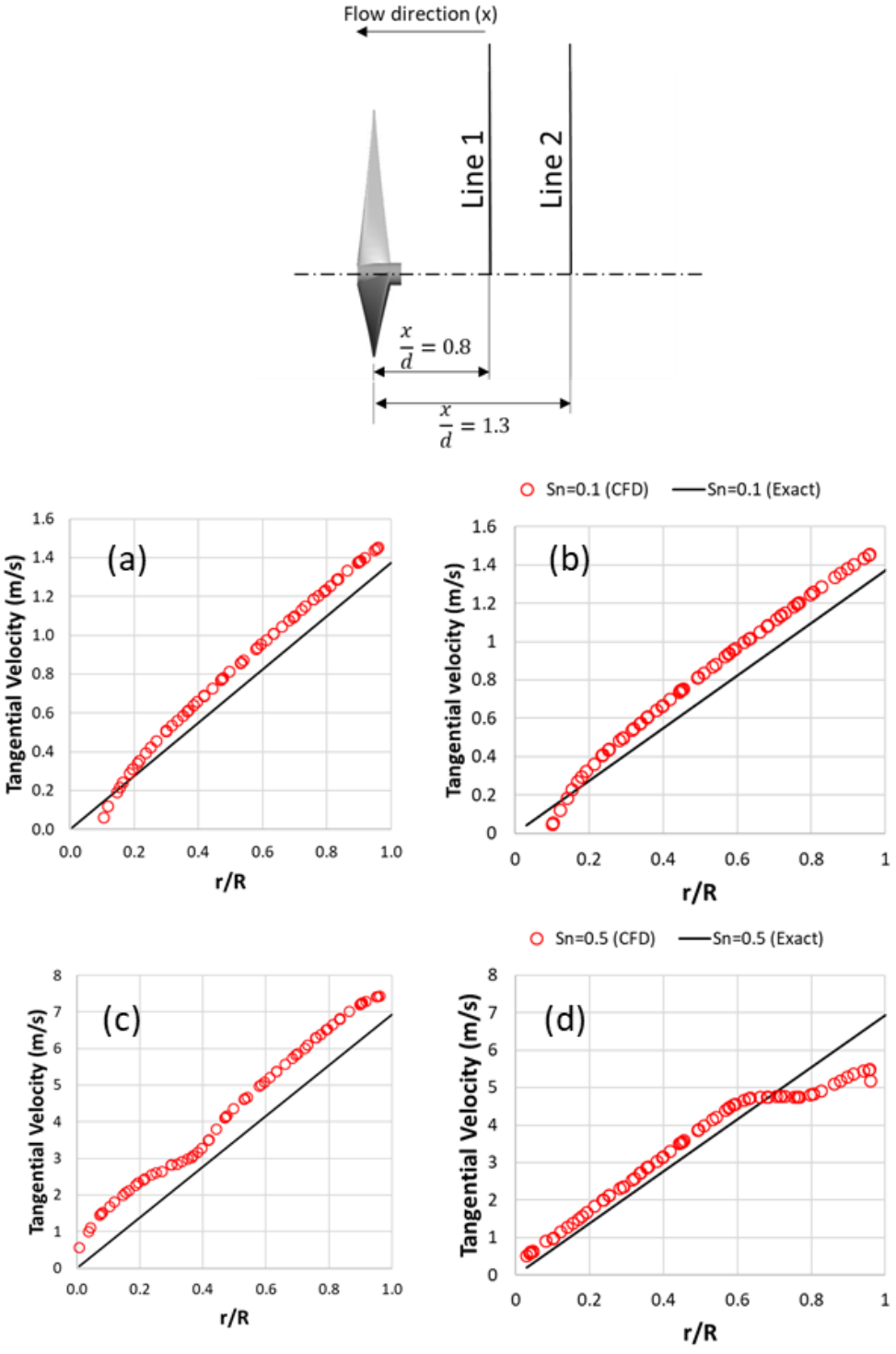

Figure (5.3), Validation graphs of the swirl flow showing the radial distribution of tangential velocity at (a,c) line 1 and (b,d) line 2 for swirl numbers (a,b) $S_n = 0.1$ and (c,d) $S_n = 0.5$.

5.4 Effects of VSG on HAMCT Hydrodynamic Performance Parameters (C_l and C_d)

In order to investigate the effect of swirl flow on the lift and drag coefficients, a parametric study has been conducted. In this study, the swirl number was varied by changing the boundary conditions, where each case represented a distinct twist-angle of the vanes. This parametric study is the core of optimizing the novel swirl generator concept proposed in this thesis. Five values of swirl number ranging from 0.1 to 0.5 (weak to moderate swirl) were tested in the study. For each swirl number, five values of AoA were simulated to examine the effects of swirl on C_l and C_d under varying current directions. Therefore, a total number of 25 cases were simulated in this parametric study. Each simulation case consumed approximately 36 CPU hours on 4 Intel core-i7 nodes and 8 GB of RAM. The lift and drag coefficients have been analyzed on each of the three blades for each case, and the ratios between C_l, C_d in swirl flow cases and C_l, C_d in zero-swirl case have been calculated. This ratio shows the change in C_l and C_d due to swirl flow. The differences between blades in C_l and C_d values come from the asymmetric nature of the flow, as reported in previous studies [137, 138].

Figure (5.4) shows the change in C_l and C_d: $\Delta C_l = \frac{C_{l\,swirl} - C_{l no\ swirl}}{C_{l\,no\ swirl}}$, $\Delta C_d = \frac{C_{d\,swirl} - C_{d no\ swirl}}{C_{d\,no\ swirl}}$. The changes in C_l and C_d determine the hydrodynamic performance gain, as indicated in figure 5.4. In figure 5.4, the area bounded by the red dashed line shows the conditions where there is positive increase in the lift coefficient and reduction ($\Delta C_d < 0$) in the coefficient of drag. To explain the surface plots in figure 5.4, the trends of ΔC_l and ΔC_d at each AoA value were plotted against varying S_n in figure 5.5. It is obvious that increasing S_n reduces C_d and improvesC_l. The values where ΔC_d are negative correspond to $S_n > 0.3$ and at the same range, there is significant improvement of C_l.

In figure (5.5), the gray boxes show the ranges of S_n that provide the best improvement in C_l where there is reduction of C_d. This is shown by depicting the difference in C_l and C_d with the variation of Swirl number for each angle of attack. Al low swirl number values, the improvement in lift is insignificant compared to the increase in drag. On the other hand, at high swirl number, the improvement in lift is significant compared to the increase of drag.

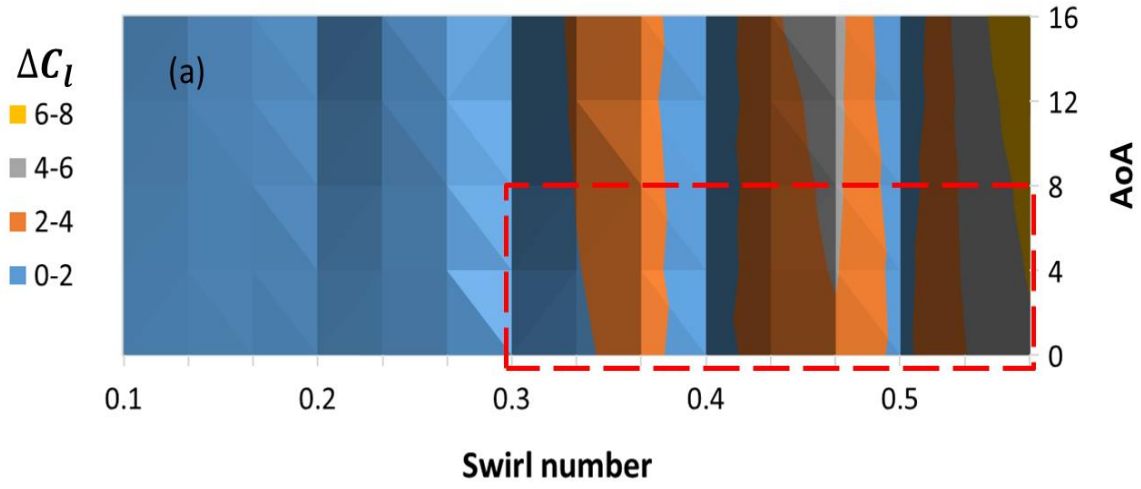

(a)

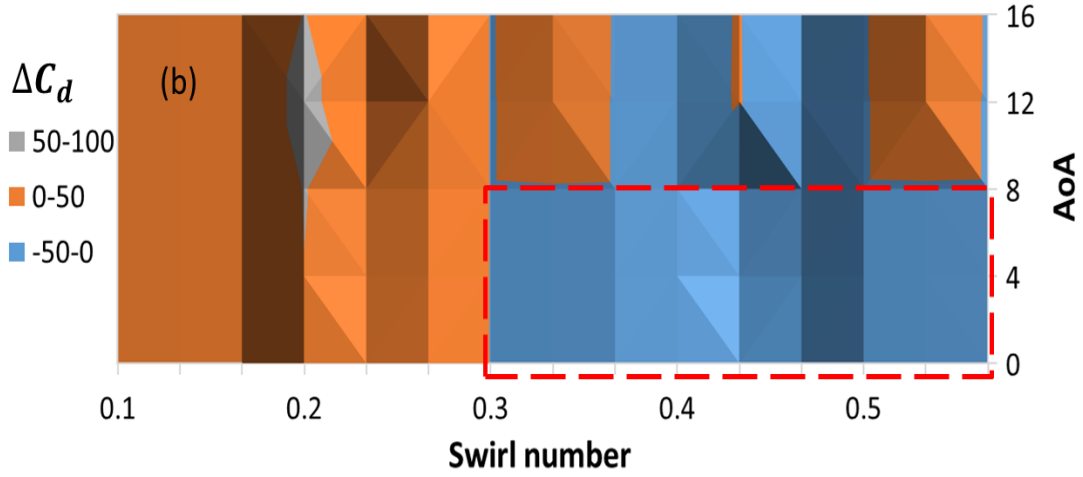

(b)

Figure (5.4), Surface plot of (a) ΔC_l and (b) ΔC_d due to swirl number variation as function of the angle of attack (AoA) for the three blades.

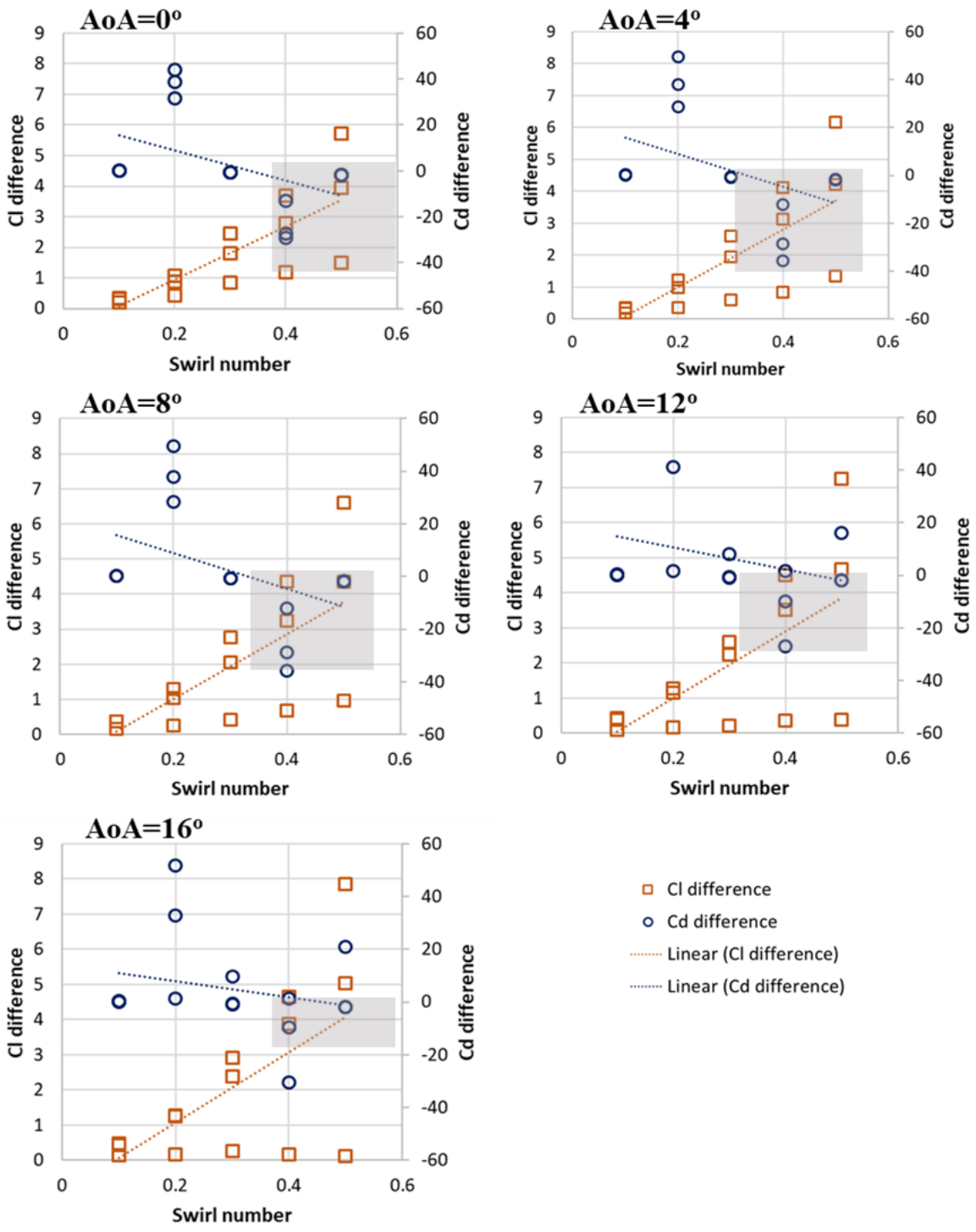

Figure (5.5), Quantitative graphs show the effects of varying S_n on ΔC_l and ΔC_d at different AoA

5.5 Effects of VSG on Power Coefficient

To explain the overall effects of VSG and swirl flow on the hydrodynamic performance of HAMCT, the power coefficient was calculated based on the same method used for validating the 3D model, as in section 4.5. Figure (5.6) shows the change of C_{Pw} according to the change in S_n and AoA. At $S_n = 0$ and AoA=0 (base case), it can be seen that $C_{Pw} = 0.18$ at TSR=2, which correspond to the conditions of transitional flow and low-current speed. The power coefficient value at no-swirl condition shows why HAMCT are not favorable in low-current speed.

When the swirl flow is introduced at low swirl number($S_n = 0.1,0.2$), the power coefficient does not improve. The power coefficient deteriorates due to the rapid increase in drag and mild improvement of lift, as shown in figures (5.4) and (5.5). When the swirl number of the VSG is increased ($S_n = 0.3,0.4,0.5$), the power coefficient obviously improves. The maximum power coefficient is obtained at $S_n = 0.5$ and AoA=12º.

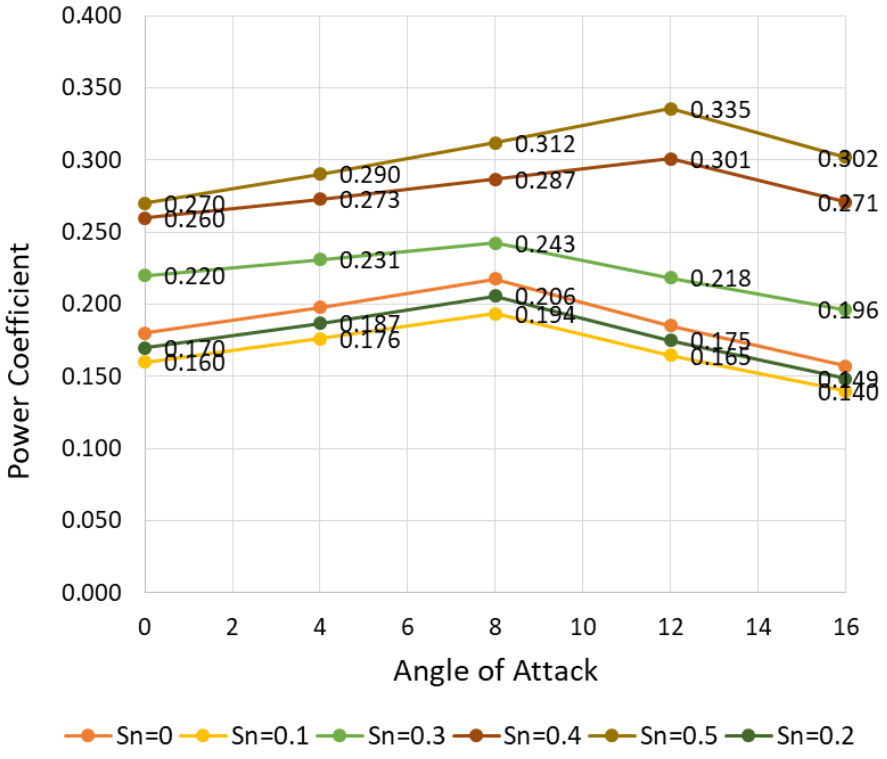

Figure (5.6) Hydrodynamic power coefficient (C_{Pw}) as function of S_n and AoA

5.6 Effects of VSG on blade pressure coefficient

Figures (5.7), (5.8) and (5.9) show VSG swirl flow effects on the pressure coefficient on the turbine blades for $0.3 \leq S_n \leq 0.5$ and $0 \leq AoA \leq 8$ which is the range at which swirl flow improved the blade hydrodynamic performance. Regardless of the AoA values, the swirl flow of VSG had a substantial effect on the pressure coefficient, as shown in the figures. The increase in the pressure coefficient corresponding to the increase of S_n explains the improvement in C_l, as reported in figure (5.5). It can be observed that the AoA had minimal effects on pressure coefficient compared to the change in S_n.

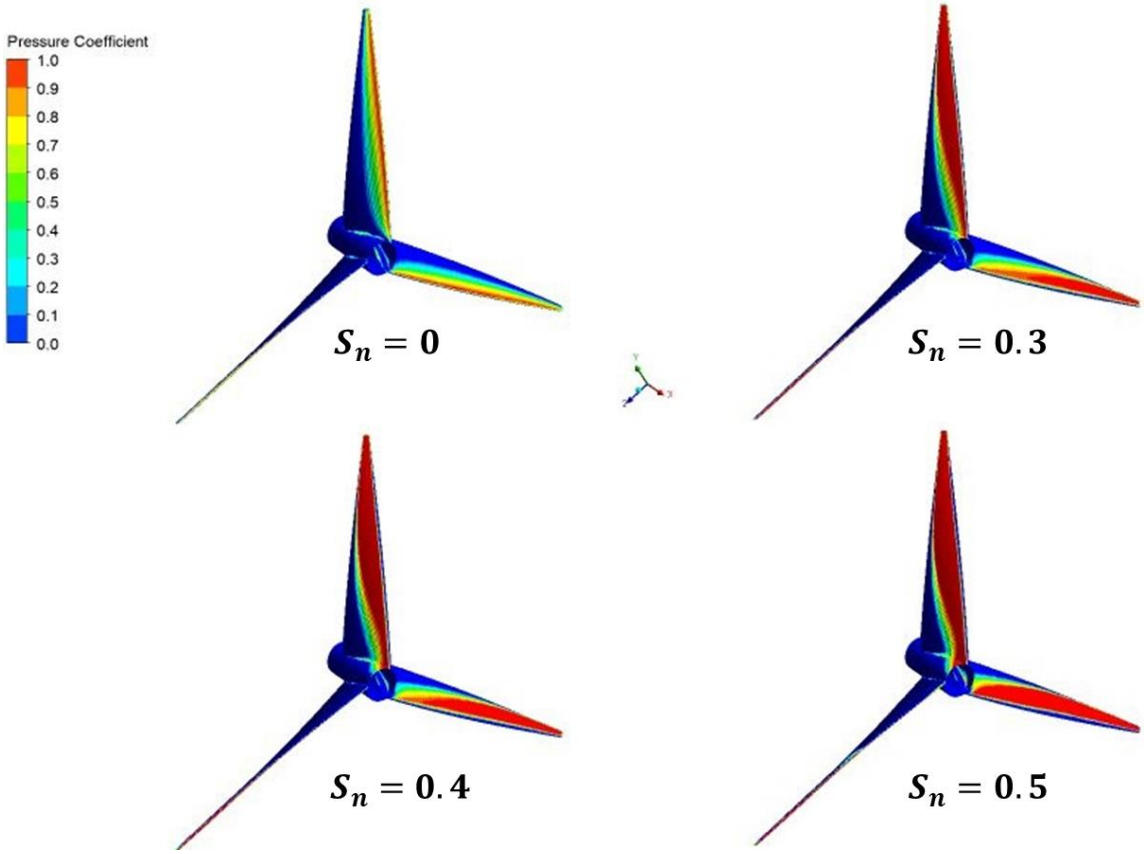

Figure (5.7), Effects of pressure coefficient on turbine blades due to the variation in S_n at AoA=0

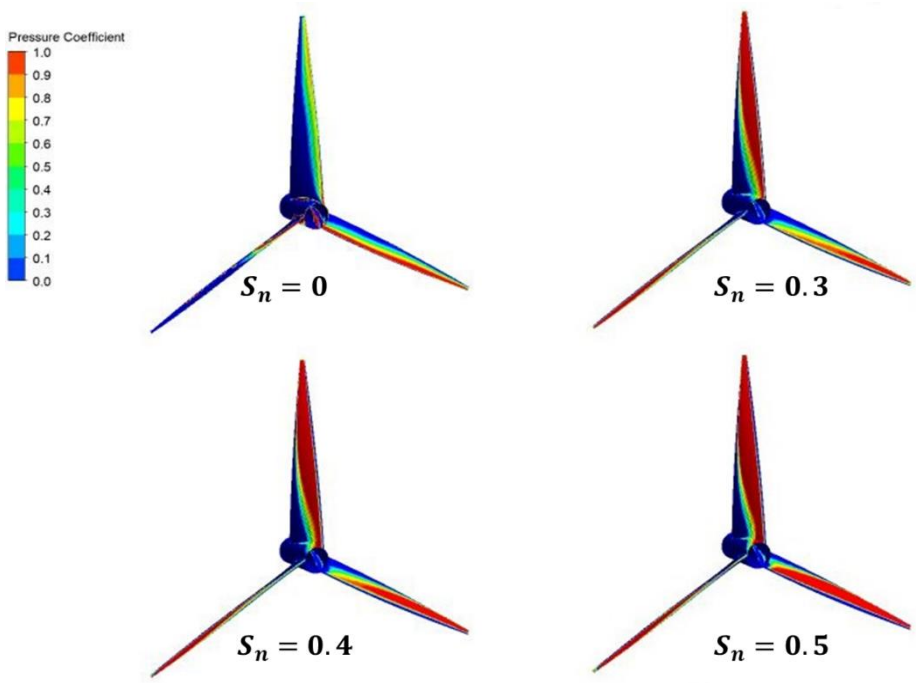

Figure (5.8), Effects of pressure coefficient on turbine blades due to the variation in S_n at AoA=4

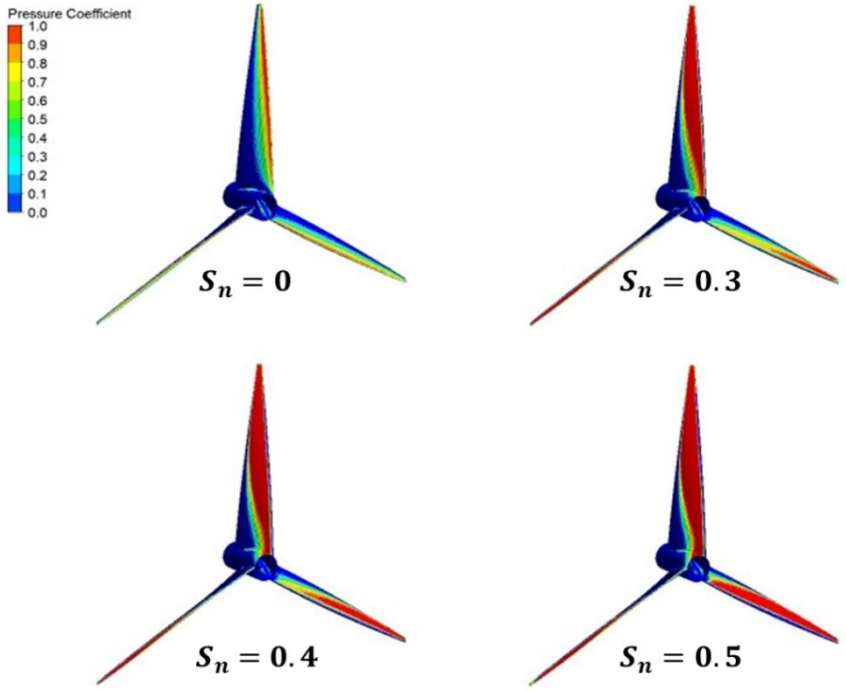

Figure (5.9), Effects of pressure coefficient on turbine blades due to the variation in S_n at AoA=8

5.7 Effects of VSG on velocity distribution around the turbine

The effects of SVG on flow velocity distribution is important to characterise the SVG performance. Figures (5.10), (5.11) and (5.12) show the effects of swirl on the hydrodynamic flow structure for $0.3 \leq S_n \leq 0.5$ and $0 \leq AoA \leq 8$ which is the range at which swirl flow improved the blade hydrodynamic performance.

At AoA=0^o figure (5.10), the variation of S_n resulted in increasing the flow asymmetry and blade recirculation zones (low velocity region near the blades). When the AoA increased to 4^o and 8^o (figures 5.11 and 5.12, respectively) the variation of S_n did not have profound effects on the velocity distribution, on the other hand, it helped to minimise the blade recirculation zones and keep it close to the blades.

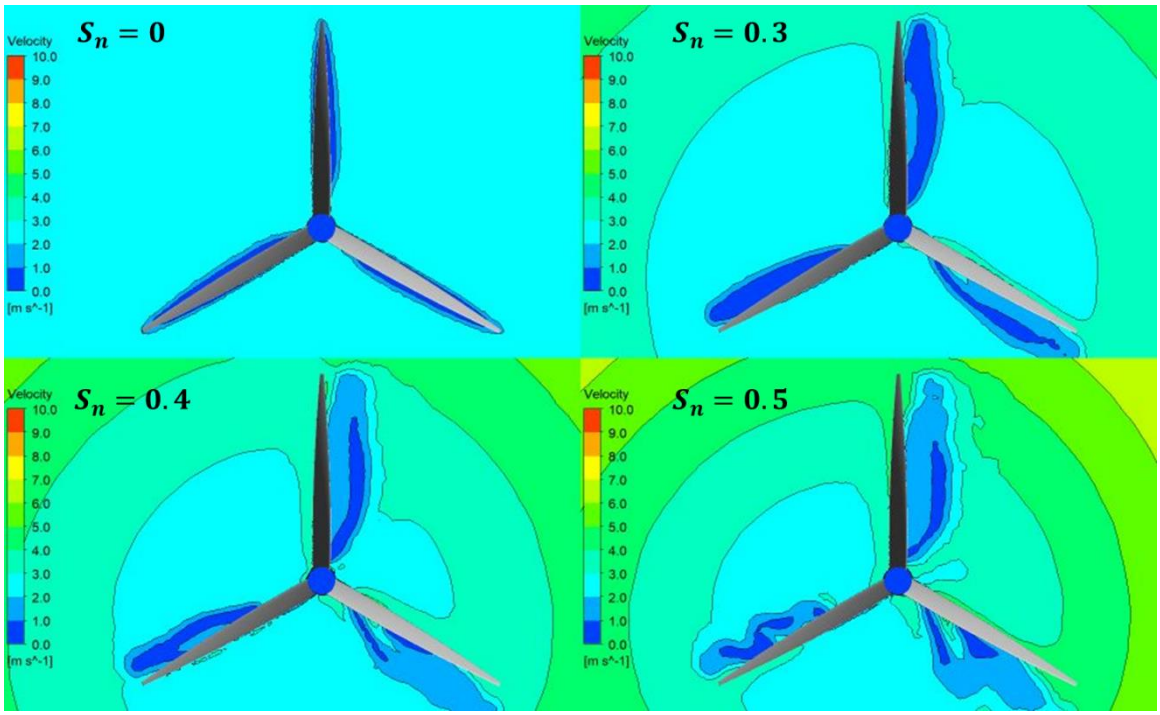

Figures (5.10), Effect of swirl flow on the velocity distribution on a mid-plane cross-section on the turbine at AoA=0 for various S_n values

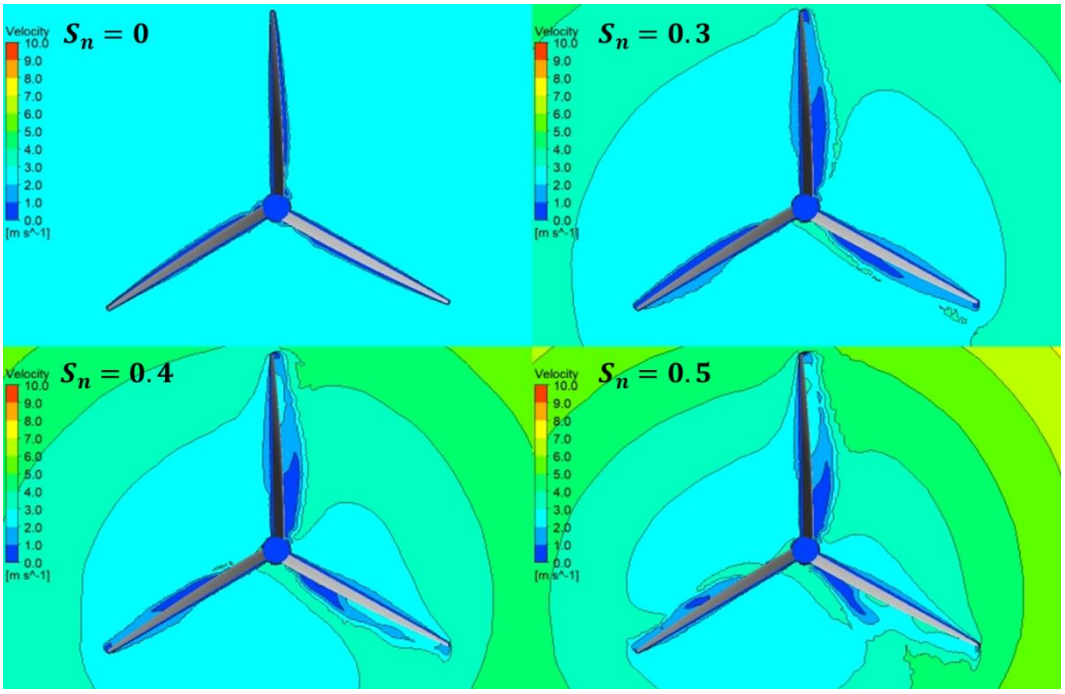

Figures (5.11), Effect of swirl flow on the velocity distribution on a mid-plane cross-section on the turbine at AoA=4 for various S_n values

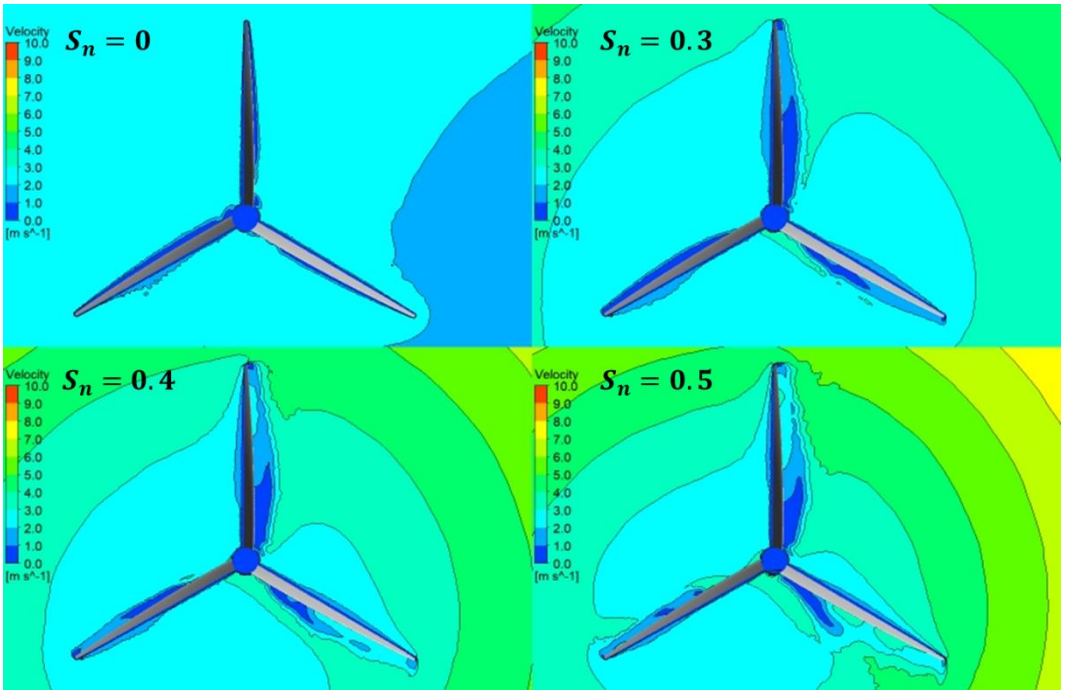

Figures (5.12), Effect of swirl flow on the velocity distribution on a mid-plane cross-section on the turbine at AoA=8 for various S_n values.

5.8 Effects of VSG on generation of turbulence kinetic energy around the turbine

The generation of turbulence kinetic energy is important to qualitatively characterise the effects of VSG on the turbine blade hydrodynamics. Figures (5.13), (5.14) and (5.15) show mid-plane cross section contours of the k generation at AoA=0^o, 4^o and 8^o, respectively, for different S_n values. It can be shown that the introduction of swirl flow increases the generation of k profoundly in all AoA values. The main region of k generation is attached to the blades and has maximum values that increase correspondingly to the increase in S_n. At AoA=0, the region of k generation is less attached to the blades than at AoA=4^o and 8^o.

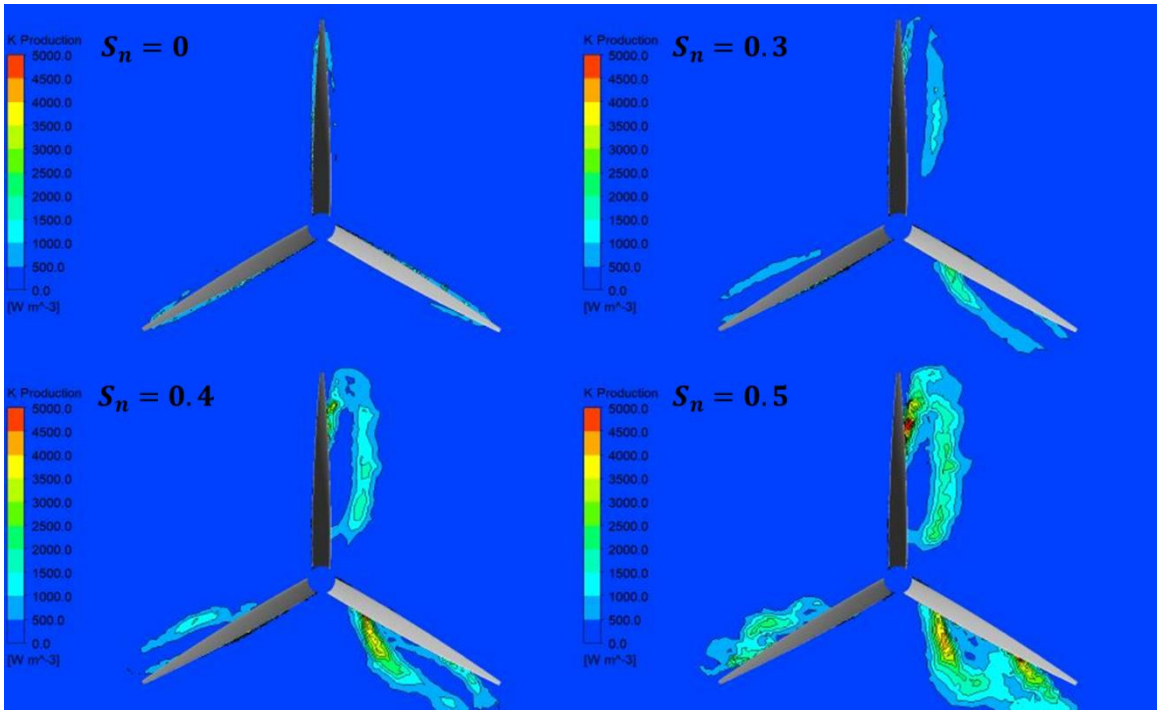

Figure (5.13), Distribution of k generation around the turbine on a mid-plane cross section at AoA=0 for different S_n values

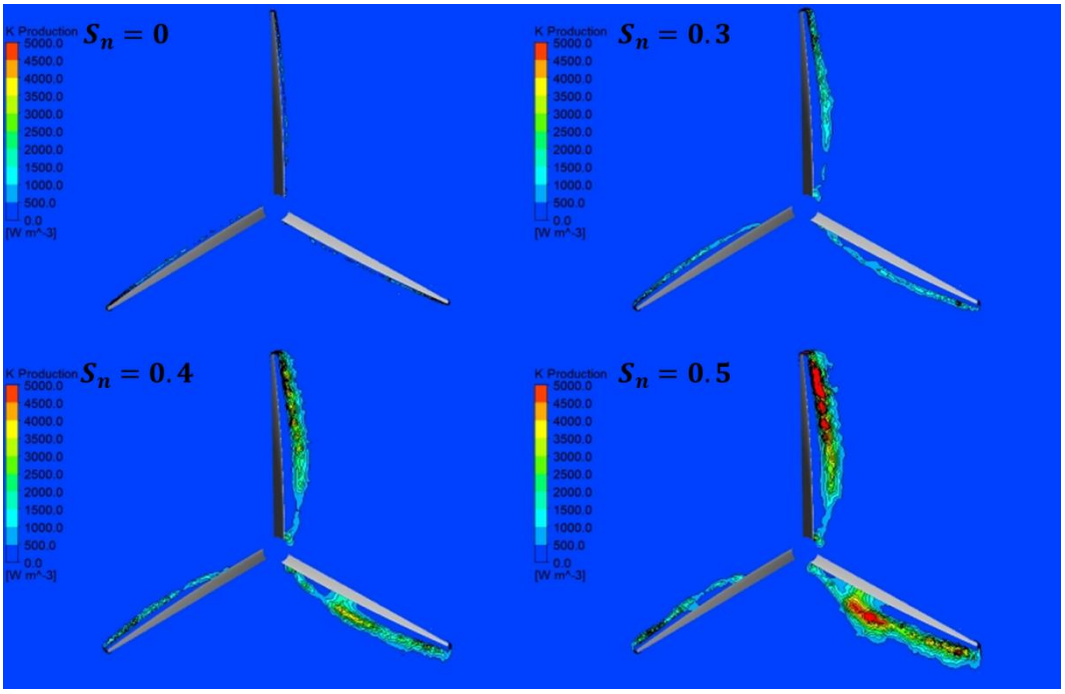

Figure (5.14). Distribution of k generation around the turbine on a mid-plane cross section at AoA=4 for different S_n values

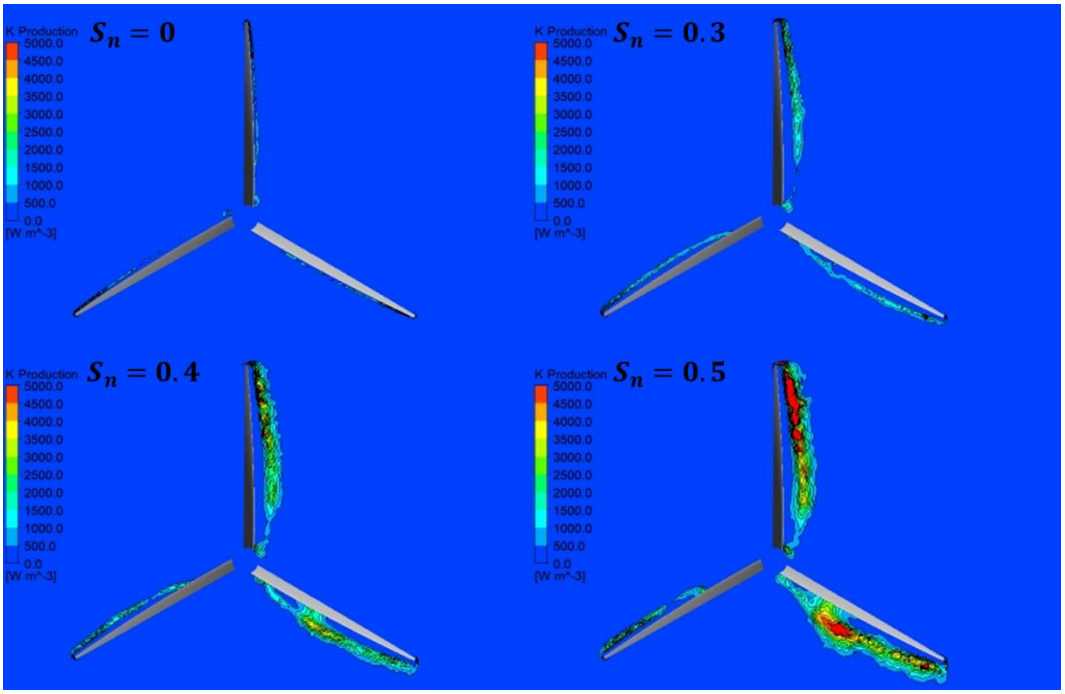

Figure (5.15), Distribution of k generation around the turbine on a mid-plane cross section at AoA=8 for different S_n values

5.9 Effects of VSG on separation around the turbine blades

Separation around the blades is best characterised by depicting the Q-criterion, that is the second invariant of the velocity vector. Figures (5.16), (5.17) and (5.18) show Iso-volumes of Q-criterion at relative values of 0.005 (1.35 S^{-1}) for AoA=0^o, 4^o and 8^o, respectively. It is clear that the introduction of swirl flow increases separation. However, the separation zone size is not significantly affected by the AoA values as much as it is affected by S_n value.

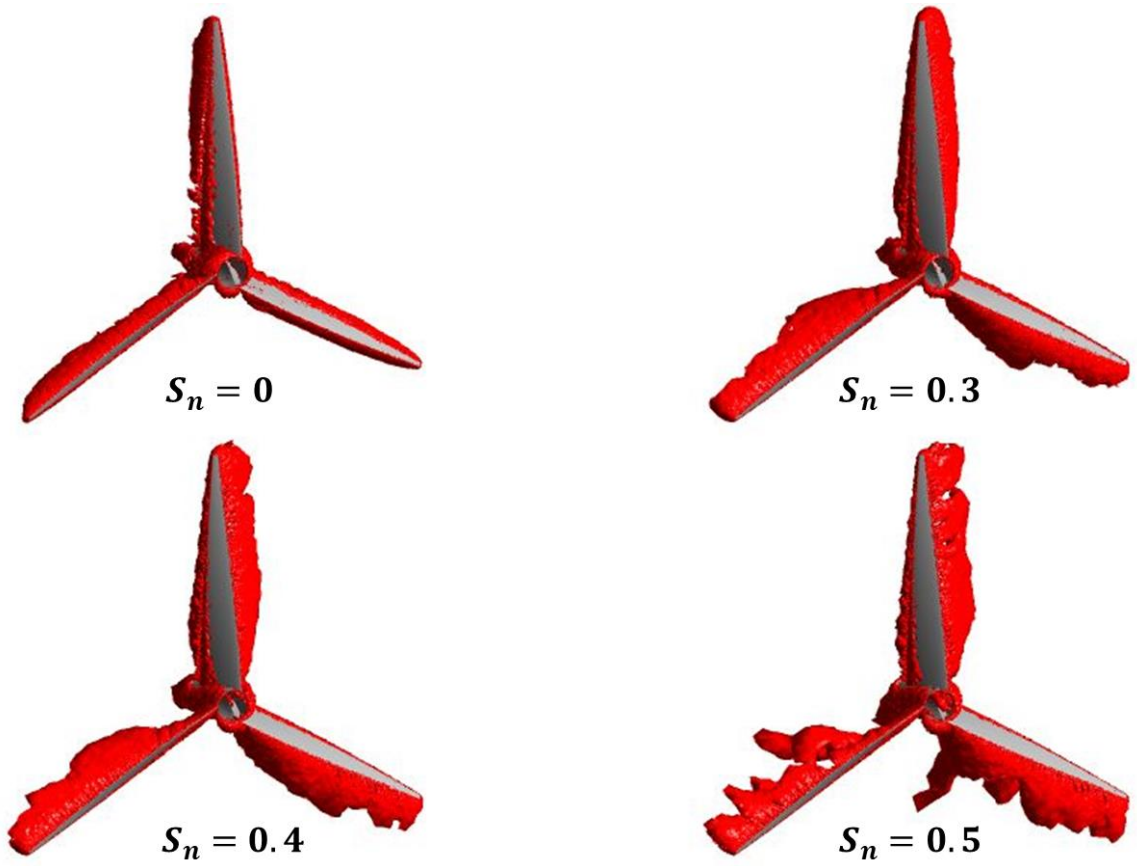

Figure (5.16), Iso-contours of Q-criterion at threshold relative value of 0.005 for AoA=0 and different S_n values

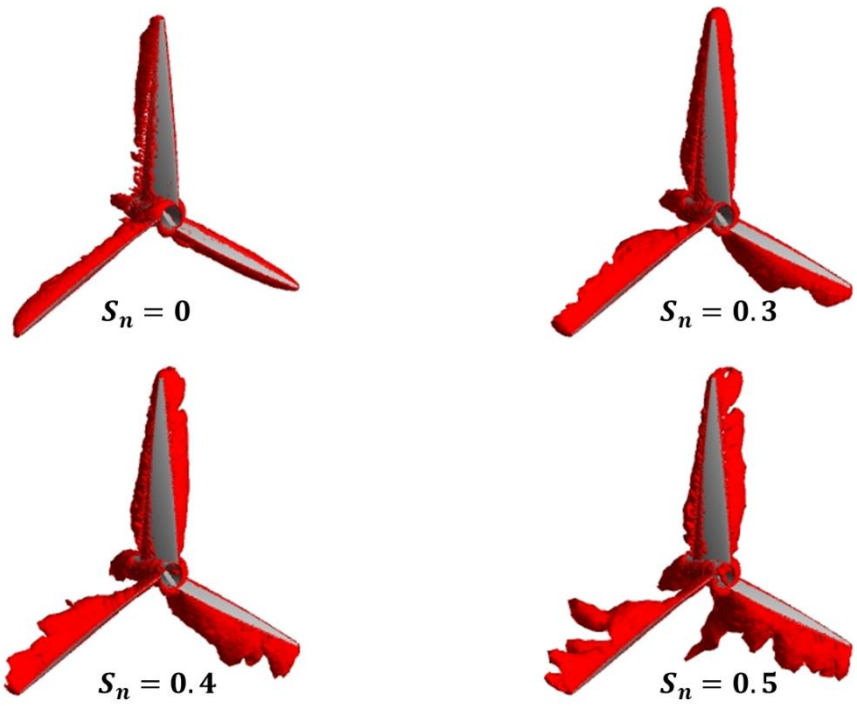

Figure (5.17), Iso-contours of Q-criterion at threshold relative value of 0.005 for AoA=4 and different S_n values

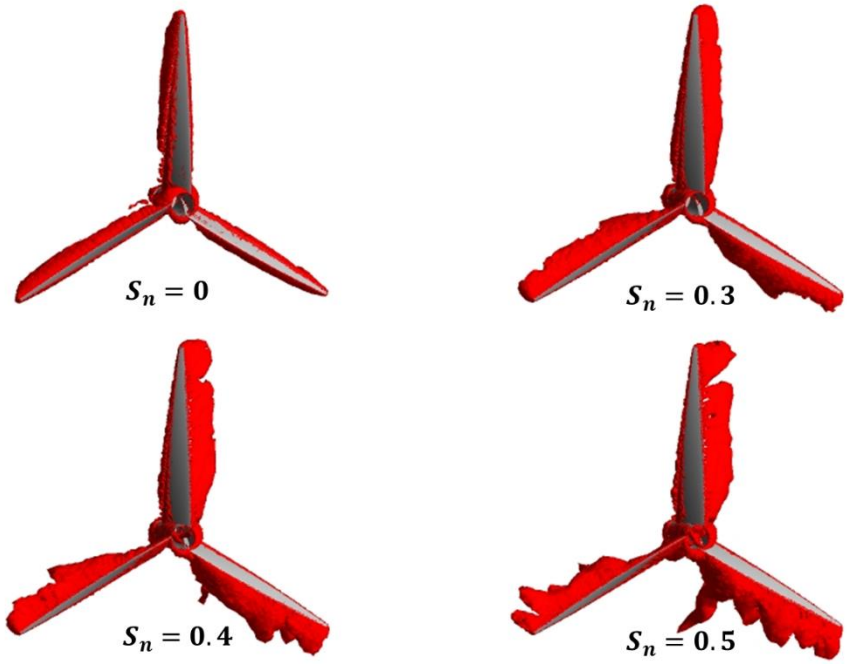

Figure (5.18), Iso-contours of Q-criterion at threshold relative value of 0.005 for AoA=8 and different S_n values

5.10 Discussion and Conclusion

A novel Vane Swirl Generator (VSG) to be installed upstream HAMCT has been conceptualized, validated a full-scale 3D CFD model. The model was validated on two stages: first by validating the HAMCT hydrodynamics predictions and comparison with benchmark dataset (Chapter 4), then by validating the swirl flow predictions and comparison with exact momentum transfer equations (Chapter 5). Complete validation of the 3D CFD model of HAMCT has been conducted, including validation for swirl flow.

Then, a parametric study comprising 30 simulation cases has been conducted and analyzed to demonstrate the effects of VSG on the hydrodynamic performance of HAMCT under transitional flow. It was found that the introduction of swirl flow improves the lift coefficient (C_l) for all values of swirl number (S_n) and angle of attack (AoA). However, the penalty of using swirl flow on the coefficient of drag (C_d) was high such that it left only the range of $0.3 \leq S_n \leq 0.5$ and $0° \leq AoA \leq 8°$ that is suitable for improvement.

Then, the effect of VSG on the power coefficient of the HAMCT was investigated. It was found that when VSG is operating at $S_n = 0.1,0.2$, the power coefficient of the turbine is reduced. This can be justified by the increase in drag coefficient at this range of swirl number. It was also found that VSG improves HAMCT's power coefficient with $0.3 \leq S_n \leq 0.5$ for all angles of attack. However, the highest improvement in C_p was found to occur at $AoA = 12°$ where it increased from 17.5% to 33.6%.

In order to understand the effect of swirl flow generated by the novel VSG on the HAMCT hydrodynamics, the pressure coefficient on the blades, velocity, turbulence and separation characteristics have been investigated. It was found that swirl flow has positive effect on the C_p corresponding to S_n increase and minimal effect corresponding to the variation of AoA. Swirl velocity component improved the distribution of velocity around the blades. As to the generation of turbulence kinetic energy, the introduction of swirl has resulted in increasing the k generation around the blades. Similar effects were observed on the size of separation zones around the blade as depicted by Q-criterion.

Chapter 6

Conclusions and Future Work

6.1 Conclusion of the CFD modeling of HAMCT

The use of CFD to simulate HAMCT has been covered in this thesis. Two dimensional models, with proper turbulence modeling and validation procedures, could provide insights onto the hydrodynamic characteristics of HAMCT hydrofoils. The transitional flow regime could be simulated with error percentage as low as 3.5% with the SST $k-\omega$ turbulence model. The variation of angle of attack could be simply represented by varying the velocity vector components at the boundary conditions.

Three-dimensional CFD models of HAMCT are excellent tools to study the turbine hydrodynamic characteristics. The main challenge in 3D CFD models is validation, since there are very scarce validation resources in literature. In comparison with previous works, considering the effects of 2D approximation through similarity theory and the impact of twist angle on the blade hydrodynamics, the 3D model proposed in this thesis has been successfully validated. The 3D model was used to investigate the effects of varying AoA on C_p, C_l and C_d, as well as the general flow structure, turbulence, and separation regions. The flow around the turbine was found to be asymmetric, which is consistent with previous works as well.

6.2 Conclusion of the novel swirl generator

A novel swirl generator (vane-type) is introduced in this thesis to improve the hydrodynamic characteristics of HAMCT. The concept depends on utilizing the dynamics of swirl flow to improve the lift coefficient of HAMCT blades. To investigate the effects of swirl flow on HAMCT characteristics and validate the concept, a parametric CFD study has been conducted. At first, the CFD model was validated for swirl flow predictions by comparing the CFD results to the exact solution of the swirl flow radial profile of tangential velocity component. Then, the effects of swirl flow, as represented by boundary condition S_n, on the coefficients of lift and drag were investigated. For all values of S_n and AoA, swirl flow improved C_l. However, the penalty of using swirl flow on the C_d was found high at $0.1 \leq S_n < 0.3$, and $8° < AoA \leq 16$. Therefore, VSG was found to improve the hydrodynamic characteristics of HAMCT for only specific values of S_n, and AoA.

6.3 Recommendation and future work

This thesis proposed a novel swirl-generator concept for improving the hydrodynamic characteristics of HAMCT. The future research should focus on the following aspects of the proposed concept:

1- Exploring other hydrofoils with the proposed concept.
2- Investigate different ranges of Reynolds number that represent different marine current profiles.
3- Investigate the turbulence characteristics with higher fidelity turbulence models (such as large eddy simulation).

Explore the effects of swirl flow on the hydrodynamic performance (energy conversion efficiency).

References

1. Fraenkel, P.L., *Tidal current energy technologies.* Ibis, 2006. 148: p. 145-151.
2. Harrison, R., E. Hau, and H. Snel, *Large wind turbines: design and economics.* 2000.
3. Nachtane, M., et al., *A review on the technologies, design considerations and numerical models of tidal current turbines.* Renewable Energy, 2020.
4. Zhou, Z., et al., *Developments in large marine current turbine technologies–A review.* Renewable and Sustainable Energy Reviews, 2017. 71: p. 852-858.
5. Sleiti, A.K., *Tidal power technology review with potential applications in Gulf Stream.* Renewable and Sustainable Energy Reviews, 2017. 69: p. 435-441.
6. O Rourke, F., F. Boyle, and A. Reynolds, *Tidal energy update 2009.* Applied Energy, 2010. 87(2): p. 398-409.
7. Bryden, I.G. and S.J. Couch, *ME1—marine energy extraction: tidal resource analysis.* Renewable Energy, 2006. 31(2): p. 133-139.
8. Fraenkel, P. *Practical tidal turbine design considerations: a review of technical alternatives and key design decisions leading to the development of the SeaGen 1.2 MW tidal turbine.* in *Ocean Power Fluid Machinery Seminar*. 2010.
9. Encarnacion, J.I., C. Johnstone, and S. Ordonez-Sanchez, *Design of a horizontal axis tidal turbine for less energetic current velocity profiles.* Journal of Marine Science and Engineering, 2019. 7(7): p. 197.
10. Soukissian, T.H., et al., *Marine renewable energy in the Mediterranean Sea: status and perspectives.* Energies, 2017. 10(10): p. 1512.
11. Aliyu, A.K., B. Modu, and C.W. Tan, *A review of renewable energy development in Africa: A focus in South Africa, Egypt and Nigeria.* Renewable and Sustainable Energy Reviews, 2018. 81: p. 2502-2518.
12. Soukissian, T., et al., *Diagnostic study of the Mediterranean marine energy resources potential*, in *PELAGOS*. 2017, Promoting innovative nEtworks and cLusters for mArine renewable energy synerGies in mediterranean cOasts and iSland.
13. Benjamin, J., et al., *Late Quaternary sea-level changes and early human societies in the central and eastern Mediterranean Basin: An interdisciplinary review.* Quaternary International, 2017. 449: p. 29-57.

14. Aghahosseini, A., D. Bogdanov, and C. Breyer. *The MENA super grid towards 100% renewable energy power supply by 2030*. in *Proceedings of the 11th International Energy Conference, Tehran, Iran*. 2016.
15. Bahgat, G., *Egypt's Energy Outlook: Opportunities and Challenges.* Mediterranean Quarterly, 2013. 24(1): p. 12-37.
16. Nash, S. and A. Phoenix, *A review of the current understanding of the hydro-environmental impacts of energy removal by tidal turbines.* Renewable and Sustainable Energy Reviews, 2017. 80: p. 648-662.
17. Lo Brutto, O.A., et al., *Tidal farm analysis using an analytical model for the flow velocity prediction in the wake of a tidal turbine with small diameter to depth ratio.* Renewable Energy, 2016. 99: p. 347-359.
18. Luo, X.-q., G.-j. Zhu, and J.-j. Feng, *Multi-point design optimization of hydrofoil for marine current turbine.* Journal of Hydrodynamics, Ser. B, 2014. 26(5): p. 807-817.
19. Kundu, P., *Hydrodynamic performance improvement on small horizontal axis current turbine blade using different tube slots configurations.* Applied Ocean Research, 2019. 91: p. 101873.
20. Dajani, S., et al., *Numerical Study for a Marine Current Turbine Blade Performance under Varying Angle of Attack.* Energy Procedia, 2017. 119: p. 898-909.
21. Bahaj, A.S., *Generating electrical power from ocean resources*, in *Comprehensive Renewable Energy*. 2012. p. 1-6.
22. Benbouzid, M.E.H., H. Titah-Benbouzid, and Z. Zhou, *Ocean Energy Technologies*, in *Encyclopedia of Sustainable Technologies*. 2017. p. 73-85.
23. Macenri, J., T. Thiringer, and M. Reed. *Power quality and flicker performance of the tidal energy converter, SeaGen*. in *44th International Conference on Large High Voltage Electric Systems 2012*. 2012.
24. Rourke, F.O., F. Boyle, and A. Reynolds, *Marine current energy devices: Current status and possible future applications in Ireland.* Renewable and Sustainable Energy Reviews, 2010. 14(3): p. 1026-1036.

25. O'Rourke, F., F. Boyle, and A. Reynolds, *Tidal current energy resource assessment in Ireland: Current status and future update.* Renewable and sustainable energy reviews, 2010. 14(9): p. 3206-3212.
26. Bahaj, A.S. and L.E. Myers, *Fundamentals applicable to the utilisation of marine current turbines for energy production.* Renewable Energy, 2003. 28(14): p. 2205-2211.
27. Harrison, M.E., et al., *Comparison between CFD simulations and experiments for predicting the far wake of horizontal axis tidal turbines.* IET Renewable Power Generation, 2010. 4(6): p. 613.
28. Marnet, O., *Behaviour and Rationality in Corporate Governance*. 2008: Routledge.
29. Khan, M.J., et al., *Hydrokinetic energy conversion systems and assessment of horizontal and vertical axis turbines for river and tidal applications: A technology status review.* Applied Energy, 2009. 86(10): p. 1823-1835.
30. Faudot, C. and O.G. Dahlhaug, *Prediction of Wave Loads on Tidal Turbine Blades.* Energy Procedia, 2012. 20: p. 116-133.
31. Liu, P. and B. Veitch, *Design and optimization for strength and integrity of tidal turbine rotor blades.* Energy, 2012. 46(1): p. 393-404.
32. Nicholls-Lee, R.F., S.R. Turnock, and S.W. Boyd, *Tidal Turbine Blade Selection for Optimal Performance in an Array*, in *Volume 5: Ocean Space Utilization; Ocean Renewable Energy*. 2011, ASMEDC.
33. Douglas, C.A., G.P. Harrison, and J.P. Chick, *Life cycle assessment of the Seagen marine current turbine.* Proceedings of the Institution of Mechanical Engineers Part M: Journal of Engineering for the Maritime Environment, 2008. 222(1): p. 1-12.
34. Bahaj, A. and L. Myers, *Analytical estimates of the energy yield potential from the Alderney Race (Channel Islands) using marine current energy converters.* Renewable energy, 2004. 29(12): p. 1931-1945.
35. Polagye, B., et al., *Environmental effects of tidal energy development.* 2011.
36. Marten, S. and P. Hall. *Marine tidal energy: A case study in legislative challenges and environmental impacts*. in *2014 IEEE Conference on Technologies for Sustainability (SusTech)*. 2014. IEEE.

37. Cada, G., *Report to Congress on the Potential Environmental Effects of Marine and Hydrokinetic Energy Technologies*. 2009, Office of Scientific and Technical Information (OSTI).
38. Davies, P., *Turning the Tide: Tidal Power in the UK*, in *The Severn Barrage and renewable energy in the estuary*. 2008, Thomas Telford Publishing.
39. Switzer, T. and D. Meggitt. *Review of literature and studies on electro magnetic fields (EMF) generated by undersea power cables and associated influence on marine organisms*. in *OCEANS 2010 MTS/IEEE SEATTLE*. 2010. IEEE.
40. Byrne, C.B.B., et al., *An investigation into the possible effects of cavitation on a horizontal axis tidal turbine.* 2011.
41. Westwood, A., *Ocean power: Wave and tidal energy review*. Refocus, 2004. 5(5): p. 50-55.
42. Carlson, T.J., et al., *Assessment of Strike of Adult Killer Whales by an OpenHydro Tidal Turbine Blade*. 2012, Office of Scientific and Technical Information (OSTI).
43. Keenan, G., et al., *SeaGen environmental monitoring programme final report.* Royal Haskoning: Edinburgh, UK, January, 2011.
44. Frid, C., et al., *The environmental interactions of tidal and wave energy generation devices.* Environmental Impact Assessment Review, 2012. 32(1): p. 133-139.
45. Seo, J., et al., *Review of tidal characteristics of Uldolmok Strait and optimal design of blade shape for horizontal axis tidal current turbines.* Renewable and Sustainable Energy Reviews, 2019. 113: p. 109273.
46. Vyshnavi, P., et al., *Tidal Current Energy for Indian Coastal Lines – A State Art of Review*. Journal of Physics: Conference Series, 2020. 1716: p. 012008.
47. Rosli, R. and E. Dimla. *A review of tidal current energy resource assessment: Current status and trend*. in *2018 5th International Conference on Renewable Energy: Generation and Applications (ICREGA)*. 2018.
48. Goldenfeld, N. and H.-Y. Shih, *Turbulence as a problem in non-equilibrium statistical mechanics.* Journal of Statistical Physics, 2017. 167(3-4): p. 575-594.
49. Chantry, M., L.S. Tuckerman, and D. Barkley, *Universal continuous transition to turbulence in a planar shear flow.* Journal of Fluid Mechanics, 2017. 824.

50. Ng, K.W., W.H. Lam, and K.C. Ng, *2002-2012: 10 years of research progress in horizontal-axis marine current turbines.* Energies, 2013. 6(3): p. 1497-1526.
51. Ingram, G., *Wind turbine blade analysis using the blade element momentum method. version 1.1.* Durham University, Durham, 2011.
52. Hughes, T.J., *The finite element method: linear static and dynamic finite element analysis*. 2012: Courier Corporation.
53. Anderson, J.D. and J. Wendt, *Computational fluid dynamics*. Vol. 206. 1995: Springer.
54. Youngren, H. and M. Drela, *Viscous/inviscid method for preliminary design of transonic cascades*, in *27th Joint Propulsion Conference*. 1991, American Institute of Aeronautics and Astronautics.
55. Molland, A.F., et al., *Measurements and predictions of forces, pressures and cavitation on 2-D sections suitable for marine current turbines.* Proceedings of the Institution of Mechanical Engineers, Part M: Journal of Engineering for the Maritime Environment, 2004. 218(2): p. 127-138.
56. Wang, D., M. Atlar, and R. Sampson, *An experimental investigation on cavitation, noise, and slipstream characteristics of ocean stream turbines.* Proceedings of the Institution of Mechanical Engineers, Part A: Journal of Power and Energy, 2007. 221(2): p. 219-231.
57. Goude, A. and O. Ågren, *Numerical Simulation of a Farm of Vertical Axis Marine Current Turbines*, in *29th International Conference on Ocean, Offshore and Arctic Engineering: Volume 3*. 2010, ASME.
58. Kevadiya, M. and H.A. Vaidya, *2D analysis of NACA 4412 airfoil.* International Journal of Innovative Research in Science, Engineering and Technology, 2013. 2(5).
59. Wang, S., et al., *Lattice Boltzmann Simulation of Hydro-Turbine Blade Hydrofoil in the Exploitation of Tidal Current Energy*, in *29th International Conference on Ocean, Offshore and Arctic Engineering: Volume 3*. 2010, ASME.
60. Shiu, H., et al. *A design of a hydrofoil family for current-driven marine-hydrokinetic turbines*. in *2012 20th International Conference on Nuclear Engineering and the ASME 2012 Power Conference*. 2012. American Society of Mechanical Engineers Digital Collection.

61. Nedyalkov, I. and M. Wosnik, *Performance of Bi-Directional Blades for Tidal Current Turbines*, in *Volume 1C, Symposia: Fundamental Issues and Perspectives in Fluid Mechanics; Industrial and Environmental Applications of Fluid Mechanics; Issues and Perspectives in Automotive Flows; Gas-Solid Flows: Dedicated to the Memory of Professor Clayton T. Crowe; Numerical Methods for Multiphase Flow; Transport Phenomena in Energy Conversion From Clean and Sustainable Resources; Transport Phenomena in Materials Processing and Manufacturing Processes*. 2014, American Society of Mechanical Engineers.
62. Karthikeyan, T., et al. *Design and analysis of a marine current turbine*. 2017. American Society of Mechanical Engineers.
63. Song, F., Y. Ni, and Z. Tan, *Optimization design, modeling and dynamic analysis for composite wind turbine blade.* Procedia Engineering, 2011. 16: p. 369-375.
64. Lawson, M.J., Y. Li, and D.C. Sale, *Development and Verification of a Computational Fluid Dynamics Model of a Horizontal-Axis Tidal Current Turbine*, in *Volume 5: Ocean Space Utilization; Ocean Renewable Energy*. 2011, ASMEDC.
65. Chen, L. and W.-H. Lam, *Slipstream between marine current turbine and seabed.* Energy, 2014. 68: p. 801-810.
66. de Jesus Henriques, T.A., et al., *The influence of blade pitch angle on the performance of a model horizontal axis tidal stream turbine operating under wave–current interaction.* Energy, 2016. 102: p. 166-175.
67. Otto, W., D. Rijpkema, and G. Vaz, *Viscous-Flow Calculations on an Axial Marine Current Turbine*, in *Volume 7: Ocean Space Utilization; Ocean Renewable Energy*. 2012, American Society of Mechanical Engineers.
68. Ikoma, T., et al., *Improvement of Torque Performance of a Vertical Axis Type Marine Turbine for a Water Current Generation System*, in *29th International Conference on Ocean, Offshore and Arctic Engineering: Volume 3*. 2010, ASME.
69. Li, L., Y. Chen, and Z. Wang, *Numerical Calculations of Bidirectional Characteristics on Tidal Current Runner*, in *Volume 6B: Energy*. 2013, American Society of Mechanical Engineers.

70. Goude, A., E. Lalander, and M. Leijon. *Influence of a varying vertical velocity profile on turbine efficiency for a vertical axis marine current turbine*. in *ASME 2009 28th International Conference on Ocean, Offshore and Arctic Engineering*. 2009. American Society of Mechanical Engineers Digital Collection.
71. Lloyd, G. and A. Espanoles, *Best practice guidelines for marine applications of computational fluid dynamics.* WS Atkins Consultants and Members of the NSC, MARNET-CFD Thernatic Network: London, UK, 2002: p. 84.
72. Chen, H., V. Patel, and S. Ju, *Solutions of Reynolds-averaged Navier-Stokes equations for three-dimensional incompressible flows.* Journal of Computational Physics, 1990. 88(2): p. 305-336.
73. Harrison, M.E., et al., *Comparison between CFD simulations and experiments for predicting the far wake of horizontal axis tidal turbines.* IET Renewable Power Generation, 2010. 4(6): p. 613-627.
74. Lain, S., et al. *Simulation of vertical axis water turbines*. 2012.
75. Laín, S., et al., *Design optimization of a vertical axis water turbine with cfd*, in *Advanced Structured Materials*. 2013, Springer Verlag. p. 113-139.
76. Liu, C. and C. Hu. *Numerical prediction of the hydrodynamic performance of a horizontal tidal turbines*. 2015. American Society of Mechanical Engineers (ASME).
77. Marsh, P., et al., *The influence of turbulence model and two and three-dimensional domain selection on the simulated performance characteristics of vertical axis tidal turbines.* Renewable Energy, 2017. 105: p. 106-116.
78. Leroux, T., N. Osbourne, and D. Groulx, *Numerical study into horizontal tidal turbine wake velocity deficit: Quasi-steady state and transient approaches.* Ocean Engineering, 2019. 181: p. 240-251.
79. Chen, B., et al., *Numerical investigation of vertical-axis tidal turbines with sinusoidal pitching blades.* Ocean Engineering, 2018. 155: p. 75-87.
80. ed-Dîn Fertahi, S., et al., *CFD performance enhancement of a low cut-in speed current Vertical Tidal Turbine through the nested hybridization of Savonius and Darrieus.* Energy Conversion and Management, 2018. 169: p. 266-278.

81. Wang, Y., et al., *Effect of blade vortex interaction on performance of Darrieus-type cross flow marine current turbine.* Renewable Energy, 2016. 86: p. 316-323.
82. Chen, H. and D. Zhou. *Hydrodynamic numerical simulation of diffuser for horizontal axis marine current turbine based on CFD*. 2014. Institute of Physics Publishing.
83. Tian, L., et al., *Effects of turbulence modelling in AD/RANS simulations of single wind & tidal turbine wakes and double wake interactions.* Energy, 2020. 208.
84. Goundar, J.N. and M.R. Ahmed, *Design of a horizontal axis tidal current turbine.* Applied Energy, 2013. 111: p. 161-174.
85. Goundar, J.N. and M.R. Ahmed, *Marine current energy resource assessment and design of a marine current turbine for Fiji.* Renewable Energy, 2014. 65: p. 14-22.
86. Ram, K.R., et al. *Optimization of hydrofoils for horizontal axis marine current turbines using genetic algorithm*. 2013. American Society of Mechanical Engineers (ASME).
87. Goundar, J.N., M.R. Ahmed, and Y.H. Lee, *Numerical and experimental studies on hydrofoils for marine current turbines.* Renewable Energy, 2012. 42: p. 173-179.
88. Asseff, N.S. and H. Mahfuz, *Design and finite element analysis of an ocean current turbine blade*. 2009: IEEE.
89. Manwell, J.F., J.G. McGowan, and A.L. Rogers, *Wind Energy Explained*. 2009, John Wiley & Sons, Ltd.
90. Kroo, I., *Applied Aerodynamics: A Digital Textbook. Desktop Aeronautics.* Inc., Stanford, CA, 2007. 94309.
91. Hansen, M.O., *Aerodynamics of wind turbines*. 2015: Routledge.
92. Cencel, Y. and J. Cimbala, *Fluid mechanics–fundamentals and applications.* 2006.
93. Patel, K.S., et al., *CFD Analysis of an Aerofoil.* International Journal of Engineering Research, 2014. 3(3): p. 154-158.
94. Jain, P., *Wind energy engineering*. 2011: New York: McGraw-Hill.
95. Ray, B., R. Bhaskaran, and L.R. Collins, *Introduction to CFD Basics.* Cornell Online Course, 2012.
96. Fluent, A., *18.0 ANSYS Fluent theory guide 18.0.* Ansys Inc, 2017.
97. Morris, C., *Influence of solidity on the performance, swirl characteristics, wake recovery and blade deflection of a horizontal axis tidal turbine*. 2014, Cardiff University.

98. Karthik, T. and F. Durst, *Turbulence models and their applications.* 10th Indo German Winter Academy, 2011: p. 1-52.
99. McKittrick, L.R., et al., *Analysis of a composite blade design for the AOC 15/50 wind turbine using a finite element model.* SAND2001-1441. Sandia National Laboratories Contractor Report, 2001.
100. Srivastava, S. and C. Aditya, *Analysis of NACA 2412 Airfoil for UAV Based on High-Lift Devices.* International Journal of Engineering Applied Sciences and Technology, 2016. 1(6): p. 13-16.
101. Roy, C., *Strategies for Driving Mesh Adaptation in CFD (Invited)*, in *47th AIAA Aerospace Sciences Meeting including The New Horizons Forum and Aerospace Exposition*. 2009, American Institute of Aeronautics and Astronautics.
102. Fluent, A., *14.0 ANSYS Fluent UDF Manual.* ANSYS, Inc. Canonsburg, PA, USA, 2013.
103. Norton, E. and D. Quarton, *Recommendations for design of offshore wind tubines (RECOFF).* D3 Deliverable-Collated Sensitivity Studies, Document, 2003(2762).
104. Gracey, W., *Measurement of static pressure on aircraft.* 1957.
105. Weltner, K. and M. Ingelman-Sundberg, *Misinterpretations of bernoulli's law.* Department of Physics, University Frankfurt, 2011.
106. Do Val, C., J. Silva, and S. Oliveira Jr, *Deep Water Cooled ORC for Offshore Floating Oil Platform Applications.* International Journal of Thermodynamics, 2016. 20(4): p. 229-237.
107. Goundar, J.N., M.R. Ahmed, and Y.-H. Lee, *Numerical and experimental studies on hydrofoils for marine current turbines.* Renewable Energy, 2012. 42: p. 173-179.
108. Anderson, J.D., *Fundamentals of Aerodynamics*. 2011: McGraw-Hill.
109. Wagner, R., et al., *Accounting for the speed shear in wind turbine power performance measurement.* Wind Energy, 2011. 14(8): p. 993-1004.
110. Incropera, F.P., et al., *Fundamentals of heat and mass transfer*. 2007: Wiley.
111. Bernardini, C., et al., *Turbine blade boundary layer separation suppression via synthetic jet: An experimental and numerical study.* Journal of Thermal Science, 2012. 21(5): p. 404-412.

112. Goundar, J.N., *Tidal Current Assessment and Design of a Horizontal Axis Tidal Current Turbine for Fiji*, in *School of Engineering and Physics*. 2012, The University of the South Pacific: Suva, Fiji Islands.
113. Roy, C. *Strategies for driving mesh adaptation in CFD*. in *47th AIAA aerospace sciences meeting including the new horizons forum and aerospace exposition*. 2009.
114. Goundar, J.N., D. Prasad, and M.R. Ahmed. *Design and performance testing of a ducted savonius turbine for marine current energy extraction*. 2013. American Society of Mechanical Engineers (ASME).
115. Guo, Q., L. Zhou, and Z. Wang, *Comparison of BEM-CFD and full rotor geometry simulations for the performance and flow field of a marine current turbine.* Renewable Energy, 2015. 75: p. 640-648.
116. Colonius, T., et al. *Closed-loop control of leading-edge and tip vortices for small UAV*. in *Conference on Active Flow Control, DFG, Berlin*. 2006.
117. Langtry, R., J. Gola, and F. Menter, *Predicting 2D Airfoil and 3D Wind Turbine Rotor Performance using a Transition Model for General CFD Codes*, in *44th AIAA Aerospace Sciences Meeting and Exhibit*.
118. Sayers, A. and A.C. Bsc, *Performance characteristics of a horizontal axis model wind turbine.* Proceedings of the Institution of Mechanical Engineers, 1981. 195(1): p. 223-229.
119. Coton, F.N., R.A.M. Galbraith, and D. Jiang, *The Influence of Detailed Blade Design on the Aerodynamic Performance of Straight-Bladed Vertical Axis Wind Turbines.* Proceedings of the Institution of Mechanical Engineers, Part A: Journal of Power and Energy, 1996. 210(1): p. 65-74.
120. Betz, A., *Introduction to the theory of flow machines*. 2014: Elsevier.
121. Panigrahi, D.C. and D.P. Mishra, *CFD Simulations for the Selection of an Appropriate Blade Profile for Improving Energy Efficiency in Axial Flow Mine Ventilation Fans.* Journal of Sustainable Mining, 2014. 13(1): p. 15-21.
122. Lucca-Negro, O. and T. O'doherty, *Vortex breakdown: a review.* Progress in energy and combustion science, 2001. 27(4): p. 431-481.
123. Gupta, A., *Lilley. DG, and Syred. N.. Swirl Flows*. 1984, ABACUS press.

124. Massey, B. and J. Ward-Smith, *Mechanics of fluids 8th ed*. 2005, Taylor & Francis e-Library.
125. Lucca-Negro, O., *Modelling of swirling flow instabilities*. 1999, University of Wales. Cardiff.
126. Lewellen, W., *A study of fluid dynamics of gaseous nuclear rockets Quarterly progress report, period ending Jun. 30, 1968.* 1968.
127. Lewellen, W., *A study of fluid dynamics of gaseous nuclear rockets Quarterly progress report, 1 Jul.-30 Sep. 1968.* 1968.
128. Sozou, C. and J. Swithenbank, *Adiabatic transverse waves in a rotating fluid.* Journal of Fluid Mechanics, 1969. 38(4): p. 657-671.
129. Morris, C.E., et al., *Evaluation of the swirl characteristics of a tidal stream turbine wake.* International Journal of Marine Energy, 2016. 14: p. 198-214.
130. Sloan, D.G., P.J. Smith, and L.D. Smoot, *Modeling of swirl in turbulent flow systems.* Progress in Energy and Combustion Science, 1986. 12(3): p. 163-250.
131. Lilley, D.G., *Prediction of Inert Turbulent Swirl Flows.* AIAA Journal, 1973. 11(7): p. 955-960.
132. Eldrainy, Y.A., et al., *Large eddy simulation and preliminary modeling of the flow downstream a variable geometry swirler for gas turbine combustors.* International Communications in Heat and Mass Transfer, 2011. 38(8): p. 1104-1109.
133. Saqr, K.M. and M.A. Wahid, *Effects of swirl intensity on heat transfer and entropy generation in turbulent decaying swirl flow.* Applied thermal engineering, 2014. 70(1): p. 486-493.
134. El Drainy, Y.A., et al., *CFD analysis of incompressible turbulent swirling flow through Zanker plate.* Engineering Applications of Computational Fluid Mechanics, 2009. 3(4): p. 562-572.
135. Saqr, K.M. and M.A. Wahid, *Numerical simulation of entropy generation in hydrogen enriched swirl stabilized combustion.* CFD Letters, 2013. 5(1-2): p. 1-5.
136. Saqr, K.M., et al., *CFD modelling of entropy generation in turbulent pipe flow: Effects of temperature difference and swirl intensity.* Applied Thermal Engineering, 2016. 100: p. 999-1006.

137. Luquet, R., et al., *Design and model testing of an optimized ducted marine current turbine.* International Journal of Marine Energy, 2013. 2: p. 61-80.

138. Lee, S.H., et al., *A numerical study for the optimal arrangement of ocean current turbine generators in the ocean current power parks.* Current Applied Physics, 2010. 10(2): p. S137-S141.

Appendix

Annex 1

Research works using Numerical Analysis

Research Author	Model	Simulation	Point of Study	Results
Goude, A. and O. Ågren	NACA 0021 3 blades 2-D study	Vortex Method	Turbine Mutual Interactions	The two-turbine system had highest coefficient per turbine than single turbine
Morris, C.E	Wortmann FX 63-137 3 Blades 2-D study	ANSYS	Evaluation of swirl characteristics	It has been shown that close to the turbine, at x/D = 0.1, Swirl number varies with tip speed ratio with a similar trend to the turbines torque coefficient, peaking at the same tip speed ratio.
Kevadiya, M. and H.A. Vaidya	NACA 4412 2-D Study Re=100000	ANSYS	2-D Analysis of NACA 4412 Air foil	The coefficient of Lift/Drag ratio increases with increase in angle of attack up to 8°. After 8°, Lift/Drag ratio decreases with increase in angle of attack.
Wang, S., et al	NACA 0012, NACA 63-215, NACA 2412, NACA 4411 and NACA 4424 1 Bladed 2-D Study	CFL3D	Lattice Boltzmann Simulation of Hydro-Turbine Blade Hydrofoil	The flow around the hydrofoil is greatly related to the angle of attack, that is, there is no vortex when the angle of attack is small and as the angle of attack increases, vortex is gradually produced on the wing back .
Lawson, M.J., Y. Li, and D.C. Sale	S814 air foil 3-Bladed 3-D Study	ANSYS FLUENT	Methodology for predicting the lift and drag coefficients, bending moments and center of pressure in the turbine rotor.	Velocity along the direction of the y-axis decreases considerably as the flow approaches the turbine rotor.
Chen, L. and W.-H. Lam	NACA 63418 3-Bladed 3-D Study	Open FOAM	Investigating the slipstream between the seabed and the	The axial component of velocity is the dominating velocity of flow below marine current turbine.

Research Author	Model	Simulation	Point of Study	Results
			marine current turbine	
de Jesus Henriques, T.A., et al	NACA 4441 near the hub to NACA 4416 at the tip 3-Bladed 3-D Study	STAR-CCM+ ANSYS CFX	Design, analysis and predict hydrokinetic performance of HAMCT with and without extreme gravity waves	By increasing the installation depth of HAMCT from the free surface, shaft loads, and power coefficient of the turbine experience oscillate respectively.
Goundar, J.N., M.R. Ahmed, and Y.-H. Lee	Hydrofoil HFSX modified from S1210 Re=2100000	Not Stated	Design of a high performance and cavitation free hydrofoil HF-SX	Cavitation is a major problem for HAMCT rotors; therefore, it is appropriate to use lower TSR, while maximizing the number of blades to have higher hydrodynamic performance, increasing the camber and thickness of hydrofoils reduces the suction peak and also improves the performance.
Otto, W., D. Rijpkema, and G. Vaz	NACA 63-8xx 3-Bladed 3-D Study Re=140000	ReFRESCO	viscous-flow calculations on an axial marine current turbine	The flow-field analysis reveals significant viscous effects. Large separation zones at the suction side of the blade are seen in the model scale results.
Baltazar, J., J. Machado, and J.A.C. Falca	Linear interpolation from the NACA 63-812, 63815, 63-818, 63-821 and 63-824 2-Bladed Re=10000000	MARETEC/IST	hydrodynamic design and analysis of horizontal axis marine-current turbines	All cases show a consistent decrease in the mean axial force and power coefficients with increasing set angle
Ikoma, T., et al	NACA 63-018. 3-Bladed 3-D Study	FLOW-3D	Improvement of torque performance of a vertical axis MCT	Regarding the cyclic pitching of turbine blades, results suggest that significant increase in average turbine torque is possible

Research Author	Model	Simulation	Point of Study	Results
Lawson, M.J., Y. Li, and D.C. Sale	NACA 63(1)424 1-Bladed 3-D Study	Harp Opt	Development and verification of a computational fluid dynamics model of a horizontal-axis MCT	For the turbine, operating conditions considered in this study, the effect of the computational time step on the CFD solution was found to be minimal, and the results from steady and transient simulations were in good agreement
Shiu, H., et al	MHKF1 family of hydrofoils. 1-Bladed 2-D Study Re=1500000	OVERFLOW	Design of a hydrofoil family for MCT	Compared to NACA 44 foils of equivalent thickness, the MHKF1-180 and MHKF1-240 foils had lower (l/d) max under clean conditions. However, when soiled, the performance falloff was much less on the MHKF1 foils, resulting in significantly higher (l/d) max values than on the NACA 44 foils
Goude, A., E. Lalander, and M. Leijon	NACA0021 3-Bladed 3-D Study	Theoretical Analysis using double multiple variable stream tube model developed by "Paraschivoiu"	Influence of a varying vertical velocity profile on turbine efficiency	Three turbine cases were studied: one turbine vertically aligned, and two horizontally aligned turbines rotating with opposite direction. The results show that the difference depends both on how much the velocity varies over the velocity profile, and on the shape of the velocity profile, where a linear profile causes a lower Cp compared to a logarithmic profile
Baltazar, J. and J.A.C. Falcão de Campos	Linear Interpolation of NACA 63812, 63-815, 63-818,	Theoretical Analysis	Hydrodynamic analysis of a horizontal axis MCT with boundary element method	The effect of the helicoidally wake model parameters used in the analysis is found to have a strong influence on the performance curves

Research Author	Model	Simulation	Point of Study	Results
	63821, and 63824. 3-Bladed 2-D Study			
Asseff, N.S. and H. Mahfuz	NACA44xx 1-Bladed 3-D Study	ANSYS	Design and finite element analysis of MCT	It is more effective, and cheaper to increase the (t/c) to make a blade stiffer and stronger, rather than increasing the skin thickness. It has also been proven that thicker profiles can still result in efficient power production
Nedyalkov, I. and M. Wosnik	B3-351045 2-D Study 1-Bladed	OpenFOAM	Performance of bi-directional blades for MCT	Bidirectional foils may provide a more cost-efficient way to account for the bi-directionality of the tidal currents, as no yaw or pitch control is required for horizontal-axis turbines utilizing blades with such shapes
Li, L., Y. Chen, and Z. Wang	S-shaped curvature hydrofoil. 2-Bladed 3-D Study	SIMPLEC algorithm	Numerical calculations of bidirectional characteristics on tidal current runner	The research results show that the efficiency of the reversible turbine is lower than that of the turbine with standard hydrofoil, but its dynamic performance is completely identical between positive condition and reverse condition. And it can be used for generation during the tide rises or ebbs
Xu, W. and S.A. Kinnas	NACA 63-8xx 3 Bladed	Fluent	Performance prediction and design of marine current turbines in the presence of cavitation	The Cavitation phenomena is lower at the top location of the blade. The blade geometry with variables x1=0.8 and x2=1.445, minimizes the turbine cavitation and produced thrust and power

Research Author	Model	Simulation	Point of Study	Results
				coefficients of 0.697 and 0.342 respectively
Jo, C.-h., et al	Thick foil of S814. 3-Bladed 3-D Study	ANSYS CFX	Numerical analysis of offshore pile structure for MCT	TCP turbine was designed using blade element momentum theory and FSI analyses were performed using ANSYS WORKBENCH Multifold. The FSI analysis procedure was established; however, two-way FSI was only a partial success. In the future, the results of the one-way FSI analysis need to be compared to the two-way FSI analysis closely
Bai, L., R.R. Spence, and G. Dudziak	NACA hydrofoils (4415) Re=100000	BEM	Analysis of a small array of 45:1 scale horizontal axis hydrokinetic turbines based on the doe reference model 1	Numerical simulations predict the theoretical drop in performance as the TSR moves away from the optimum and the angle of attack along the span increases above the value of maximum lift and into stall
	NACA 63-215 NACA 63-815	BEM	To study the hydrodynamic design parameters	The power coefficient for both series of sections for pitch angles of 0 and 88. Both section shapes have similar performance although the NACA 63-8xx series show delayed stall at low tip speed ratio (TSR). Cavitation can be avoided or minimized by suitable pitching of the blades or using a section with higher camber
Baltazar, J., J. Machado, and J.A.C	NACA 63-815 and NACA 63-824 Re=580000		The effect of platform motions on turbine performance	The effect of platform motions on axial loading of the turbine is analyzed by comparing differences that occur between a captive and moored platform for different environmental

Research Author	Model	Simulation	Point of Study	Results
				conditions. It was shown that for the current only condition, which is more or less a constant velocity on the turbine, does not show big differences between the moored and captive platform

Annex 2

Research Works using Experimental Analysis

Research No	Model Test rig	Experiment	Point of Study	Results
Bahaj, A., et al	NACA 63-812, 63-815, 63-818, 63-821 and 638242.	Cavitation Tunnel and Test Tank	Power and thrust measurement	The results show an increase in Cp and Ct as hub pitch angle is reduced, with maximum CP=0.46 occurring for the design 20 pitch angle
Yang, B. and X. Shu	NACA0012 Gottingen 623 2-Bladed Re=1500000	Flow visualization by PIV using helical vertical axis turbine	Hydrofoil optimization	It is observed that (CL/CD) total of the optimized has been greatly increased in comparison with another two competitive hydrofoils, NACA 0012 and Gottingen 623
de Jesus Henriques, T.A	Wortmann FX 63-137 3-Bladed 3-D Re=230000	Recirculating water channel	The influence of blade pitch angle on the performance of HATT	As the blade pitch angle was increased from optimum, both the mean power and thrust on the turbine decreased and the reductions in thrust were always greater than in power
Yang, B. and X.W. Shu	NACA 63-8xx 3-Bladed 3-D	800mm diameter turbine in a cavitation tunnel and a towing tank	Experimental verifications of numerical predictions for the hydrodynamic performance of HAMCT	Numerical analysis demonstrates similar trends in the results and provides a satisfactory representation of the experimental turbine performance
Goundar, J.N., M.R. Ahmed, and Y.-H. Lee	Hydrofoil HF-Sx modified from S1210 Re=2100000	The experiments were performed in an Engineering Laboratory Design (ELD)	Design of a high performance and cavitation free hydrofoil HF-SX	Cavitation is a major problem for HAMCT rotors; therefore, it is appropriate to use lower TSR, while maximizing the number of blades to

Research No	Model Test rig	Experiment	Point of Study	Results
		Inc., low speed open circuit wind tunnel		have higher hydrodynamic performance, increasing the camber and thickness of hydrofoils reduces the suction peak and also improves the performance
Ikoma, T., et al	NACA 63-018. 3-Bladed 3-D Study	single-return water current and water wave channel, at the Institute of Industrial Sc, University of Tokyo	Improvement of torque performance of a vertical axis MCT	Regarding the cyclic pitching of turbine blades, results suggest that significant increase in average turbine torque is possible
Bahaj, A., W. Batten, and G. McCann	S814 3-Bladed 3-D Study Re=1500000	Full scale rotor blade MCT	Simulation and prediction of loads in MCT	both thrust and torque increase as the current speed increases, and in longer waves the torque is relatively sensitive to the variation of wave height
Senat, J. and M. Arockiasamy	NACA 63-8xx	Towing tank, at Southampton Solent University	Comparing energy yields from fixed and yawing horizontal axis MCT	The extra energy yield from the yawing turbine is insignificant and the location is therefore suitable for a bidirectional turbine
Blunden, L.S. and W.M. Batten	Rotor Disk Model. 3-D Study Re=100000	21m tilting flume, at the Chilworth Research Laboratory, University of Southampton	The Effect of boundary proximity upon the wake structure of horizontal axis MCT	When in close proximity with the seabed a discontinuity in mass flow rate above and below the rotor disk causes the wake to be deflected downwards. The lower rate of flow beneath the disk reduces the energization along the underside of the wake that is usually

Research No	Model Test rig	Experiment	Point of Study	Results
				caused by turbulent mixing of the free stream and wake fluid. Similarly, velocity between the wake and ambient flow reduces the shear stresses that serve to dissipate the wake and therefore, it persists further downstream which has a direct effect upon the downstream spacing of devices within multi-row arrays
Nedyalkov, I. and M. Wosnik	B3-351045 2-D Study 1-Bladed	University of New Hampshire, High-Speed Cavitation Tunnel - HICAT	Performance of bidirectional blades for MCT	Bidirectional foils may provide a more cost-efficient way to account for the bi directionality of the tidal currents, as no yaw or pitch control is required for horizontal-axis turbines utilizing blades with such shapes
Bahaj, A.S., et al	NACA hydrofoils (4415) Re=100000	Proceedings of the 3rd Marine Energy Technology Symposium	Analysis of a small array of 45:1 scale horizontal axis hydrokinetic turbines based on the doe reference model 1	The net result is a higher kinetic energy flux, obtained by integrating the cube of the flow velocity along the cross section of the rotor disk, in the downstream-most turbine (0.437 V 3 ∞) compared to the middle turbine (0.387 V 3 ∞). The most remarkable observation from the efficiency results, in a three turbine coaxial array, is that the downstream-most turbine produces more power and a higher efficiency than the middle turbine

Research No	Model Test rig	Experiment	Point of Study	Results
Seo, J., et al	NACA 63-215 NACA 63-815.	Research Institute of Marine Systems Engineering, Seoul National University, Seoul, Korea	Experimental study on wake fields of a horizontal axis tidal stream turbine model in various loading conditions	As TSR decreased, the angle of attack increased. Stall might occur at the lowest TSR. The angle of attack onto the turbine blade section near the turbine axis was large, resulting in strong lift force on the blade section. Strong lift accompanied downwash flow developed into the circumferential flow in the 3D turbine wake. Radial flow was observed out of the wake stream, implying expansion of the wake region
Van der Plas, P.	NACA 63-815 and NACA 63-824	Blue TEC platform in the circulation tank of IFREMER in Boulogne-Sur-Mer (France)	The effect of platform motions on turbine performance	Unsteady flow field causes fluctuating loads on the rotor and results in varying power outputs. To correctly analyze turbine performance, the fluctuating inflow velocity cannot be neglected in the analysis of turbine performance
Barltrop, N., et al.	S814	Universities of Glasgow and Strathclyde	Investigation into wave–current interactions in marine current turbines	The presence of waves will increase the torque on the rotor at lower range of current speed whereas mean axial thrust is almost unchanged
Myers, L. and A. Bahaj	NACA 44XX Aerofoil sections	University of Southampton, Southampton	Power output performance characteristics of a horizontal axis marine current turbine	Full-scale MCTs operating at yaw coupled with the relatively low blade speed will cause a slower change in blade AoA with blade azimuth position hence the hydrodynamic

Research No	Model Test rig	Experiment	Point of Study	Results
				characteristics will vary over time. This introduces an interesting aspect into MCT operation as the power output will vary with each rotation and cause an effect known as flicker
Maganga, F.	tri-bladed horizontal axis turbine	Le Havre University and IFREMER (French Research Institute for Exploitation of the Sea)	Experimental characterization of flow effects on marine current turbine behavior and on its wake properties	It was observed (as expected) that the water velocity recovery is faster in area of greater ambient turbulence intensity. Increased ambient turbulence intensity leads to the formation of a narrower wake (stream wise direction). Rapid changes in turbulent kinetic energy production
Esfahani, J.A. and H.R. Karbasian	NACA 63-215 hydrofoil	Ferdowsi University of Mashhad	Optimizing the shape of rotor blades for maximum power extraction in marine current turbines	The lift to drag ratio is at its maximum value, the effect of TSR on the shape of the blade is insignificant. Thus, the chord profile extruded throughout the span of the blades must be designed with a maximum lift to drag ratio at each section of the blades